POLITECNICO
MILANO 1863

SCUOLA DI INGEGNERIA INDUSTRIALE
E DELL'INFORMAZIONE

Preliminary design of a fixed-wing VTOL UAV for Martian flight

Tesi di Laurea Magistrale in
Aeronautical Engineering - Ingegneria Aeronautica

Author: **Marco Bertani**

Student ID: 989627
Advisor: Prof. Alberto Guardone
Academic Year: 2022-23

Abstract

NASA Mission to Mars 2020 marked a historic achievement for space exploration. For the first time, remotely controlled flight on an extraterrestrial atmosphere was accomplished by Ingenuity, the Mars Helicopter.

This important result fostered interest towards large-scale exploration of Mars. In the future, long-range missions could be performed in Martian environment by fixed-wing UAVs, which would allow for larger payloads and greater range.

However, the rarefied atmospheric conditions on Mars produce several changes on the design of a fixed-wing UAV compared to those for terrestrial applications. The thin Martian atmosphere is characterised by very low density and glacial temperature, affecting significantly the aerodynamics of the UAV and, therefore, its overall performance.

This thesis presents the conceptual and preliminary design of a vertical take-off and landing fixed-wing UAV for the Martian environment, in the framework of a scientific mission for the large-scale aerial exploration of the Red Planet.

In addition, a comparative study is carried out between the Martian drone design and that of a UAV designed to carry out a similar mission on Earth, to highlight design similitudes and differences, and their dependence on the planet characteristics. An outlook towards similar design for UAV operating in the Venus and Titan atmosphere concludes the thesis.

Keywords: Mars UAV, Mars aerodynamics, Aircraft design, eVTOL

Abstract in lingua italiana

La missione NASA Mission to Mars 2020 segnò un traguardo storico nella saga dell'esplorazione spaziale. Infatti, per la prima volta nella storia venne effettuato un volo a controllo remoto in un'atmosfera extraterrestre, grazie ad Ingenuity, l'elicottero marziano.

Questo risultato straordinario favorì la crescita di un grande interesse verso l'esplorazione di Marte su larga scala. In futuro, potranno essere effettuate alcune missioni ad elevata autonomia nell'ambiente marziano grazie all'utilizzo di droni ad ala fissa, i quali consentiranno di trasportare carichi paganti più elevati e per distanze maggiori.

Tuttavia, le condizioni atmosferiche che si trovano su Marte provocano diversi effetti nella progettazione di velivoli ad ala fissa ed a pilotaggio remoto, rispetto a quanto di consueto per le applicazioni terrestri. L'atmosfera marziana è caratterizzata da una densità molto bassa e da temperature glaciali, influenzando notevolmente le caratteristiche aerodinamiche del drone e, di conseguenza, le sue prestazioni complessive.

Questa tesi presenta la progettazione concettuale e preliminare di un drone a decollo ed atterraggio verticale pensato per l'ambiente marziano, nel contesto di una missione scientifica per l'esplorazione su larga scala del Pianeta Rosso.

Inoltre, presenta uno studio comparativo tra la progettazione del drone marziano e quello di un UAV progettato per compiere una missione analoga sulla Terra, con lo scopo di evidenziarne similarità e differenze, e la loro dipendenza dalle diverse caratteristiche planetarie. Uno sguardo verso la progettazione di droni ad ala fissa per missioni su Venere e Titano conclude il lavoro di questa tesi.

Parole chiave: Drone marziano, aerodinamica su Marte, progettazione di velivoli, eVTOL

Contents

1 | Introduction

Mission Mars 2020 by NASA marked the success of the first powered flight on an extra-terrestrial atmosphere, thanks to Ingenuity, the Mars Helicopter. Ingenuity is a small UAV capable to fly in the thin Martian atmosphere, at few meters height over Crater Jezero, the landing site of Perseverance rover, with a range of few hundreds of metres and an endurance of a couple of minutes. Up to November 2023, Ingenuity performed 66 flights for a total of 118.8 flying minutes, covering 14.9 km and reaching altitudes as high as 24.0 m [48].

Even if the Mars Helicopter is just a technological demonstrator, its success have raised great interest towards powered flight in the Martian atmosphere. In the future, one of the objectives will be the increase in the mission range in order to perform scientific experiments at a large scale. To this aim, fixed-wing UAVs might represent a suitable choice, bringing several advantages with respect to rotary-wing drones (as the Mars Helicopter), in particular for what concerns the mission range and endurance.

Mars represents an extreme environment, in many respects. The impervious terrain characteristics of the Martian surface require that the drone disposes of VTOL capabilities. Another important theme is that of the energy supply on Mars, where the most abundant and economic energy source is represented by solar energy. Therefore, the most natural choice for that environment might be the use of electric VTOL UAVs equipped with wing-mounted solar panels.

The very low density and glacial temperature of the Martian surface affect significantly the aerodynamics of the UAV and its capability to generate lift. The most similar conditions on Earth to those of Mars are the ones faced by High-Altitude Long-Endurance (HALE) UAVs.

Another important topic is the cost per kg to build and to get to Mars. To build and launch the Mars 2020 Perseverance mission cost $ 2.4 billion, according to NASA. Perseverance Rover a total mass equal to 1025 kg, it corresponds to roughly $ 2.34 million per kg. Ingenuity cost $ 81 million, it has a maximum take-off mass of 1.8 kg, leading to a cost of $ 45 million per kg. This implicates that it is very important to keep the maximum

take-off mass of the UAV as low as possible.

State-of-the-art and innovative technologies are required in order to make the flight on Mars possible, and realise in the future scientific missions at a large scale, making use of fixed-wing UAVs.

This thesis investigates the future applicability of fixed-wing UAVs in the Martian environment, proposing the preliminary design of an electric VTOL UAV equipped with wing mounted solar panels, in the framework of a scientific mission for the large scale aerial exploration of the Red Planet. The mission consists in the use of miniaturized gas-chromatography coupled with a mass spectrometer for the collection and analysis of soil samples, along with the characterisation of the Mars atmosphere, also in unexplored regions, exploiting the long range capabilities of the UAV.

Afterwards, this thesis proposes the preliminary design of a second drone conceived to replicate a similar mission of those of the martian UAV, but at terrestrial conditions. A comparative study is carried out to highlight design similarities and differences, analysing their dependence on the planet characteristics, especially the atmospheric density and planetary gravitational acceleration.

In this chapter a general overview of the Red Planet is presented, the main characteristics are investigated, such as the mean distance from the Sun, the planetary mass and density, gravitational acceleration and daily duration. Later, a more in-depth analysis of the topography and soil composition of the Red Planet is carried out, to retrieve relevant locations for the definition of future scientific missions in that environment. Later, the topic of the energy supply on Mars is discussed, by defining the solar irradiance and how it is affected by the astronomical features of the Red Planet, in order to retrieve a simple model to be used for the sizing of the recharging system of the Mars UAV.

Afterwards, the Martian atmosphere is described, and an engineering atmospheric model is presented. It will be used for the design of the Martian UAV. A concise presentation of the timeline of Mars exploration, and an introduction to Ingenuity, the Mars Helicopter is later presented, along with a critical analysis of the possible benefits brought by the use of fixed-wing UAVs for the exploration of Mars.

In addition, similarly for what presented for the Martian case, the main features of the terrestrial environment are described, in particular the atmospheric model and the solar irradiance characteristics. The chapter is concluded with the presentation of some categories of air vehicles of common use for terrestrial applications, that present some common feature with the basic requirements for the Martian flight. Those are electric

vertical take-off and landing vehicles (eVTOLs), High Altitude Long Endurance aircraft (HALE), and small Unmanned Aerial Systems (UAS).

1.1. Martian environment

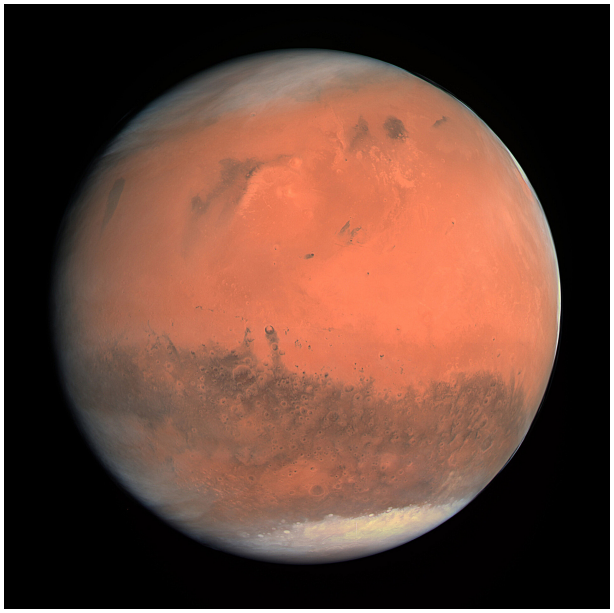

Figure 1.1: Mars

1.1.1. General Overview

Mars is the fourth planet from the Sun and the second smallest planet in the Solar System. The Red Planet is the most similar to Earth in terms of size and composition. Mars may have had a dense atmosphere and liquid water on the surface in a distant past. However, today the atmosphere of Mars is very thin and liquid water exists only in the form of ice. The Red Planet has a very different surface with respect to Earth. Mars is covered by impact craters, mountains, valleys, and sand dunes. The surface of Mars is also much older than that of Earth.

The Red Planet is located on average at 228 million kilometers from the Sun, which in terms of astronomical units corresponds to 1.524 AU, and 150 million kilometers from Earth. The mean radius of Mars is about 3390 km, hence the Red Planet is roughly half the size of the Earth [45]. One day on Mars is 24.6 hours long, one year lasts 669.6 sols, or solar days. This is the equivalent of 687 days on Earth. The rotation axis is tilted 25° with respect to the plane of its orbit around the Sun, similarly to the 23.4° tilt of the terrestrial rotation axis. This tilt conducts to the presence of seasons on Mars, similarly

to Earth. On the Red Planet seasons do not have all the same length because of the elliptical orbit of the planet around the Sun. Concerning the northern hemisphere, spring is the longest season of the year with 194 sols, autumn is the shortest with 143 sols.

The only source of power in that environment is represented by the Sun; the solar radiation decreases with the square of the heliocentric distance, therefore on Mars it is less abundant than on Earth.

The mean density of Mars is about $\rho_{\text{Mars}} = 3934 \ \frac{\text{kg}}{\text{m}^3}$, 29 % lower than the mean density of Earth, which is about $\rho_{\text{Earth}} = 5513 \ \frac{\text{kg}}{\text{m}^3}$ [49]. The total mass of the Red Planet is about $M_{\text{Mars}} = 6.42 \times 10^{23}$ kg, roughly 10.7 % of the $M_{\text{Earth}} = 5.97 \times 10^{24}$ kg of the Earth. As a result, the gravitational acceleration on Mars surface is $g_{\text{Mars}} = 3.72 \ \frac{\text{m}}{\text{s}^2}$, roughly 38 % of the terrestrial $g_{\text{Earth}} = 9.81 \ \frac{\text{m}}{\text{s}^2}$.

Mars also has two moons, the largest is Phobos, the smallest is Deimos. On average, Phobos is 9377 km distant from Mars, but is getting closer at a rate of 1.8 m over a hundred years, so in 50 million years it will either collide over the Martian surface or produce a ring around the Red Planet.

Two seasonal polar caps are present on the Red Planet. MARSIS (Mars Advanced Radar for Subsurface and Ionosphere Sounding) studied the subsurface structure of Martian polar caps. Results indicate that both northern and southern caps are up to 3.5 km thick, composed by water ice and carbon dioxide ice. The water reservoir contained in the southern polar cap is the largest on Mars. According to ESA [42], the melting of the polar ice would cover the planet with an ocean 11 metres deep.

1.1.2. Topography and soil composition

Mars is about half the size of Earth, with a mean radius of approximately 3390 kilometers. It has a dense innermost core between 1500 to 2100 kilometers in radius. It's made of iron, nickel, and sulfur. A rocky mantle surrounds the core between 1240 to 1880 kilometers deep. The outermost layer is a crust made of iron, magnesium, aluminum, calcium, and potassium. The crust is between 10 to 50 kilometers thick.

The typical red color of Mars is the result of the oxidization of iron that composes the Martian regolith. Martian regolith is mainly basaltic in composition as a consequence of past volcanism. It contains salts such as sulfates and perchlorates.

The first few in situ measurements of the soil composition of the Martian surface came with missions Viking 1, Viking 2 and, later, Pathfinder. These landers arrived in the younger regions of the Mars surface, corresponding to the lower-elevation northern plains.

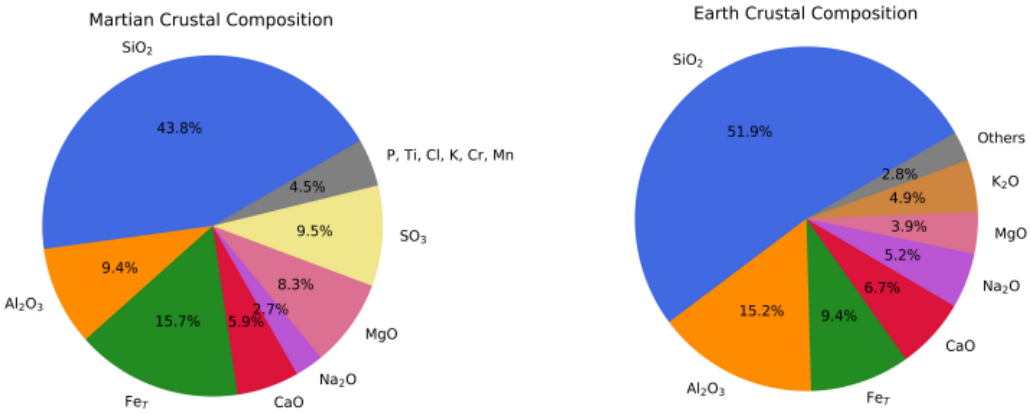

(a) Martian crustal composition (b) Terrestrial crustal composition

Figure 1.2: Martian and terrestrial crustal compositions

More recent rovers such as Spirit, Opportunity, and Curiosity landed over older regions of the planet.

First measurements by Viking lander determined that the Martian surface is, compared to the terrestrial, lower in Al compositions, higher in Fe, and with much higher concentrations of S and Cl, which suggests the formation from rocks of mafic or ultramafic type, as described by [8] and [22]. Viking landing sites were distant roughly 4500 km, but the sites' average compositions were extremely similar. This led to the conclusion that airborne dust was transported and deposited by global dust storms, which had the effect to homogenize the surface composition. This theory has been confirmed by the analyses of dust samples collected by Pathfinder, MER rovers, and Curiosity.

The compound of the Martian regolith is highly basaltic, having as main composition pyroxene, plagioclase, olivine, along with Fe and Fe-Ti oxides and some alteration minerals (such as sulfates, carbonates, and clays). The particle size of Martian regolith ranges from 1 µm to 1000 µm, with average Martian soil grain sizes being between 250 µm and 300 µm.

Figure 1.2 compares the terrestrial and Martian crustal composition. The topographic characteristics of the Red Planet have been collected by the Mars Global Surveyor spacecraft, launched in 1996. It was equipped with an altitude Mars Orbiter Laser Altimeter (MOLA).

Mars presents some interesting topographic features: Olympus Mons, with 26 975 m height is the highest peak in the Solar System; Valles Marineris is the largest canyon of

the Solar System, it extends for more than 3 000 km, it spans as much as 600 kilometers across, and delves as much as 8 kilometers deep. Hellas Planitia is a meteoritic crater in the Martian southern hemisphere, it extends over roughly 2300 km and reaches up to 7 km in depth.

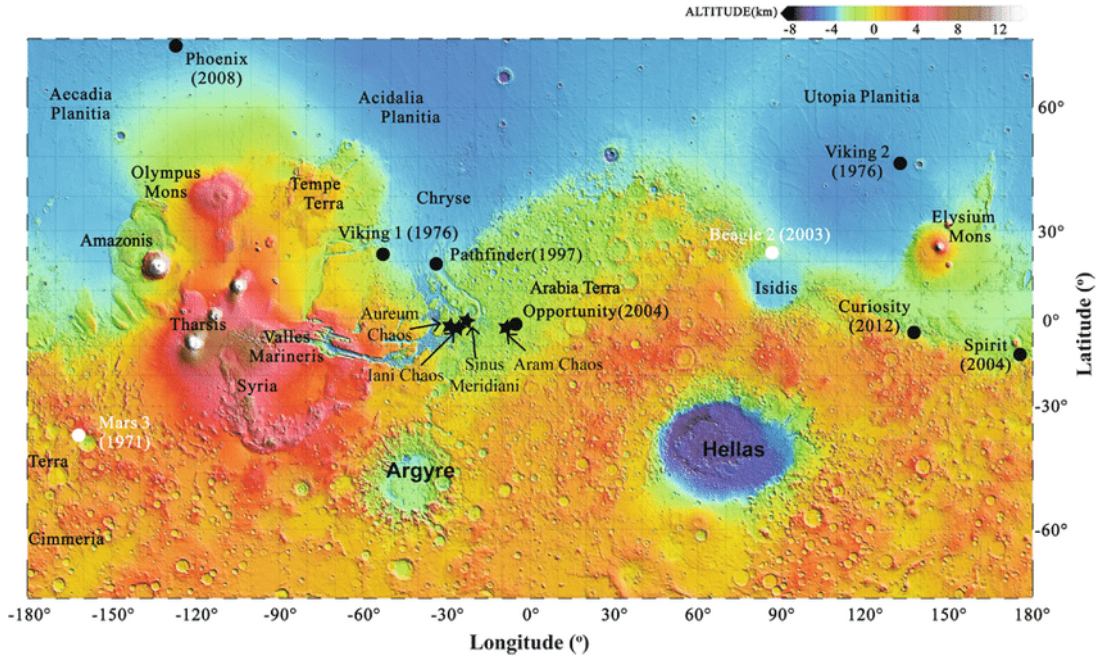

Figure 1.3: Mars topographic map

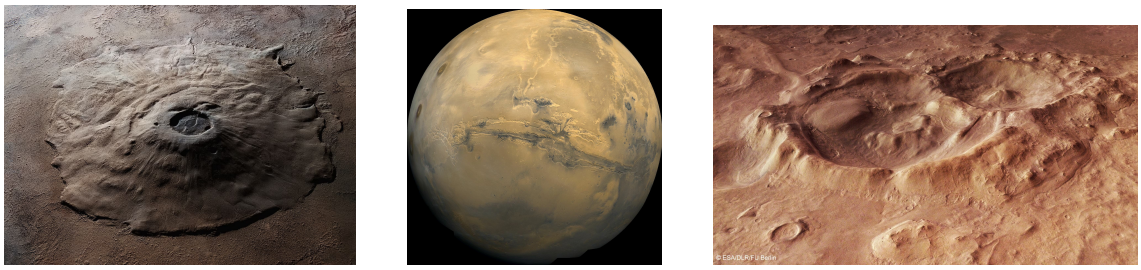

(a) Olympus Mons (b) Valles Marineris (c) Hellas Planitia

Figure 1.4: Mars topographic features

The landing site of Mission to Mars 2020 is Jezero Crater, part of Isidis Planitia. Reference coordinates of Jezero Crater are $18.38°N$, $77.58°E$.

Opportunity Rover discovered evidence that water had existed in the Meridiani Planum region. At present day, water reservoirs on Mars reside in the subsurface of the Planet. The vast majority of H_2O on Mars is in the form of ice.

1.1.3. Solar irradiance

The solar irradiance on Mars is described by reference [6], where the characterisation of the solar radiation on the Martian surface has been evaluated by the definition of a normalized net solar flux function f, dependent by the optical depth τ and the zenith angle z. The formulation involves other parameters, such as the diurnal and hourly variation of the global irradiance G, of the beam irradiance G_b, and of the diffuse irradiance G_d over a considered surface.

As well as for planet Earth, the solar radiation on the surface of Mars is formed by two components: direct beam irradiance G_b and diffuse irradiance G_d.

The direct beam is influenced by scattering and absorption along the path from the top of the Martian atmosphere to the Martian surface. Measurements of the optical depth of the Martian atmosphere τ allows an estimate of the absorption and scattering out of the beam. These estimates were derived in the past from images of the Sun and Phobos taken with a special diode by cameras on the Viking lander.

Considering the beam irradiance at the top of the Martian atmosphere, defined as G_{ob}, and measured in $\left[\frac{W}{m^2}\right]$, it can be computed as

$$G_{\text{ob}} = \frac{S}{r^2}, \tag{1.1}$$

where S is the Solar Constant $S = 1371\frac{\text{W}}{\text{m}^2}$, and r is the heliocentric distance in AU (Astronomical Unit). The Sun-Mars mean distance in astronomical units (AU) is $r_{\text{mean}} = 1.5237$. Therefore, the mean beam irradiance at the top of Mars atmosphere is equal to $G_{\text{ob,mean}} = 590\ \frac{\text{W}}{\text{m}^2}$.

The heliocentric distance r depends by the Mars semimajor axis a, measured in AU; the eccentricity e (for the Red Planet $e_{\text{Mars}} = 0.093377$); and the true anomaly θ.

The heliocentric distance, measured in astronomical units is given by

$$r = \frac{a(1-e^2)}{1 + e\ cos(\theta)}. \tag{1.2}$$

The true anomaly θ is related to the areocentric longitude L_S and the areocentric longitude of Mars perihelion, corresponding to 248°

$$\theta = L_S - 248°. \tag{1.3}$$

As a result, the beam irradiance at the top of Mars atmosphere can be expressed as

$$G_{ob} = S\left[\frac{1 + e\cos(L_S - 248°)}{a(1-e^2)}\right]^2. \tag{1.4}$$

In order to size the photovoltaic power system, it is fundamental to consider only the solar irradiance G that reaches the Martian surface, which would be significantly reduced with respect to the one at the top of the Martian atmosphere G_{ob} due to the effect of the opacity of the atmosphere. In addition, it is fundamental to consider the projection of G over an horizontal surface G_h, which is related to the cosine of the solar zenith angle z.

$$G_h = G\,cos(z) \tag{1.5}$$

The global irradiance on a horizontal surface G_h can be also expressed as:

$$G_h = G_{bh} + G_{dh}, \tag{1.6}$$

where: G_{bh} is the direct beam irradiance on a horizontal surface; G_{dh} is the diffuse irradiance on a horizontal surface

There is no specific way to directly measure the diffuse irradiance G_{dh}, but it is obtained by subtracting the beam from the global irradiance.

The direct beam irradiance, G_b, on the Martian surface normal to the solar rays is related by Beer's law (1.7)

$$G_b = G_{\mathrm{ob}}\, e^{-\tau m(z)}, \tag{1.7}$$

where τ is the optical depth of the intervening atmospheric haze and m(z) is the air mass related to the zenith angle z, that can be approximated as

$$m(z) \simeq \frac{1}{\cos(z)}. \tag{1.8}$$

The direct beam irradiance G_b can be projected on an horizontal surface in order to retrieve G_{bh}

$$G_{bh} = G_b\cos(z). \tag{1.9}$$

The cosine of the zenith angle of the incident solar radiation is expressed by

$$\cos(z) = \sin(\phi)\sin(\delta) + \cos(\phi)\cos(\delta)\cos(\omega) \tag{1.10}$$

where ϕ is the latitude; δ is the declination angle; ω is the hour angle measured from the true noon westward.

The solar declination angle δ is defined as

$$\sin(\delta) = \sin(\delta_0)\sin(L_S), \tag{1.11}$$

where δ_0 is the Mars obliquity of the rotation axis ($\delta_0 = 24.936°$).

The global irradiance G_h is computed in reference [6] by making use of a normalized flux function $f(z, \tau)$

$$G_h = G_{\text{ob}} \cos(z) \frac{f(z, \tau)}{0.9}, \tag{1.12}$$

where τ is the optical depth and it is assumed to remain constant throughout a Martian day. Opacity is minimum during the northern spring ($0° \leq L_S \leq 90°$) and summer ($90° \leq L_S \leq 180°$), and maximum during the seasons during which most local and global dust storms occur, typically southern spring ($180° \leq L_S \leq 270°$) and summer ($270° \leq L_S \leq 360°$). When dust storms are not present, the optical depth is typically about $\tau = 0.5$.

The table presented by figure 1.5 reports a set of values that are assumed by the normalized net flux function $f(z, \tau)$. Those data are related to an albedo of 0.1 but it is stated by reference [6], that it can also be used for higher albedo to a first approximation.

TABLE III. - NORMALIZED NET FLUX FUNCTION $f(z,\tau)$ AT THE MARTIAN SURFACE

Optical depth	Zenith angle Z, deg									
τ	0	10	20	30	40	50	60	70	80	85
0.1	0.885	0.883	0.882	0.880	0.876	0.870	0.857	0.830	0.755	0.635
0.2	.866	.865	.860	.858	.851	.836	.813	.758	.640	.470
0.3	.847	.846	.841	.836	.826	.806	.774	.708	.562	.412
0.4	.828	.827	.821	.815	.802	.778	.740	.667	.502	.373
0.5	.810	.810	.802	.796	.778	.752	.708	.628	.452	.342
0.6	.793	.791	.785	.775	.755	.725	.677	.593	.414	.318
0.7	.776	.773	.766	.755	.733	.700	.646	.555	.383	.298
0.8	.760	.756	.750	.736	.710	.675	.616	.520	.360	.280
0.9	.745	.740	.733	.717	.690	.650	.587	.487	.336	.264
1.0	.732	.725	.717	.700	.670	.628	.560	.455	.317	.252
1.1	.713	.709	.700	.682	.651	.604	.539	.433	.300	.239
1.2	.697	.692	.683	.662	.632	.585	.518	.413	.288	.230
1.3	.682	.677	.667	.646	.613	.567	.498	.394	.273	.220
1.4	.666	.661	.650	.629	.596	.546	.478	.379	.262	.210
1.5	.651	.646	.633	.612	.580	.530	.460	.362	.251	.202
1.6	.637	.630	.618	.597	.563	.512	.441	.348	.240	.195
1.7	.622	.615	.601	.581	.546	.494	.424	.332	.232	.188
1.8	.609	.600	.586	.568	.531	.480	.408	.318	.224	.181
1.9	.596	.587	.571	.551	.514	.464	.393	.304	.217	.176
2.0	.582	.573	.558	.537	.500	.448	.378	.293	.208	.170
2.25	.552	.542	.522	.501	.462	.410	.343	.265	.190	.156
2.50	.518	.509	.492	.469	.430	.378	.316	.242	.174	.145
2.75	.486	.478	.462	.440	.401	.353	.293	.224	.158	.136
3.00	.460	.450	.434	.414	.376	.330	.273	.206	.150	.128
3.25	.434	.424	.410	.390	.354	.308	.254	.193	.140	.120
3.50	.411	.400	.387	.367	.333	.290	.240	.180	.132	.110
4.00	.370	.360	.347	.330	.296	.258	.212	.160	.118	.100
5.00	.294	.286	.275	.258	.230	.203	.166	.130	.094	.080
6.00	.228	.223	.215	.200	.178	.153	.130	.103	.080	.068

Figure 1.5: Normalised Net Flux Function

Results indicate that the beam irradiance shows a sharp decrease with increasing of the

optical depth, and a relative moderate decrease with increasing of the zenith angle. In addition, the diffuse irradiance shows a sliding maximum with the variation of the zenith angle.

Another major concern to the assessment of performance of solar panels on Martian environment is represented by dust storms. These have been observed to occur both on local and global scales.

The intensity of Martian global and local dust storms is defined in terms of opacity and dust raised. According to Appelbaum and Flood [6]: *"Global dust storms are those which obscure planetary-scale sections of the Martian surface for many Martian days (sols), whereas local dust storms are less intense, and form and dissipate in a few days or less. From a photovoltaic system design point of view, the intensity, frequency, and duration of these storms may be viewed as partially cloudy and cloudy days for which additional energy storage in the photovoltaic system must be taken into account."*

Global dust storms typically occur once or twice a Martian year, and last from 35 to 70 sols. Those begin typically near perihelion, when solar insolation is maximum in the southern mid-latitude. During global dust storms, the opacity is greater than one. Local dust storms can occur at almost all latitudes and throughout the year. They are most frequent in the latitudes of $10° - 20°N$ and $20° - 40°S$. They typically last few days, and the opacity can be assumed to be about one.

For the sizing of the solar power system is necessary to compute the daylight time. The number of Mars daylight hours T_d, is defined as

$$T_d = \frac{2}{15} \cos^{-1}(-\tan(\phi)\tan(\delta)). \tag{1.13}$$

The number of Mars daylight hours is related to the sunset hour angle ω_{ss}, given by

$$\omega_{ss} = \cos^{-1}(-\tan(\phi)\tan(\delta)). \tag{1.14}$$

Once that the sunset hour angle ω_{ss} is known, the sunrise hour angle can be computed according to symmetry considerations.

1.1.4. Atmosphere

Mars atmosphere have been investigated by the mission of the Mars Science Laboratory (MSL) of NASA, especially through the use of the Sample Analysis at Mars (SAM) [24]. SAM addresses the chemical and isotopic composition of the atmosphere and volatiles extracted from solid samples. This module is part of Curiosity Rover, it is a 40 kg instrument formed by a quadrupole mass spectrometer, a tunable laser spectrometer, and a 6-column gas chromatograph all coupled through solid and gas processing systems to provide complementary information on the samples. The SAM suite is able to measure a set of light isotopes and to analyze volatiles directly from the atmosphere or thermally released from solid samples. The primary science goals of SAM are to find compounds, especially carbon compounds, chemical and isotopes states of lighter elements in rocks, soils and atmosphere, in order to characterize the geology and geochemistry of the landing sites, to investigate the role of water, and to measure the spectrum of surface radiation.

The objective is to provide answers to the questions concerning future potential habitability of the Red Planet and investigate how were environmental conditions on Mars in the past. The atmospheric conditions on Mars are extremely challenging for life because of the lack of abundant liquid water, glacial temperatures, and the presence of surface ultra-violet and near surface cosmic radiation. However, it was hypothesized by Acuna et al. [1], that the climate on Mars was more benign several billion years ago, when presented a thicker atmosphere protected by an early planetary magnetic field.

In depth analysis about the composition of the Martian atmosphere have been found in reference [41]. The article presents the results collected by SAM, with in-situ measurements in Gale Crater, during a period of three Martian years (MY), from MY 31 to MY 34. Results indicate that the atmosphere of Mars is composed by 95.1 % carbon dioxide, 2.59 % nitrogen, 1.94 % argon, 0.161 % oxygen and 0.058 % carbon monoxide. These are average values, that are subject to significant variations during a Martian year, and year-to-year. The main causes of this phenomenon are Mars' obliquity and large orbital eccentricity.

Carbon dioxide (CO_2) is the primary component of Mars atmosphere, its global surface density varies significantly due to the condensation (during winter) and sublimation (during spring) in the polar regions. During the first 200 sols of Curiosity's mission on the Mars surface, over Gale Crater, a stable pressure increase was recorded up to the reach of an annual maximum during fall, just after the perihelion. Afterwards, a stable decrease in pressure was measured to a local minimum around sol 470, during the formation of the north polar cup, produced by the condensation of CO_2. The pressure decreased again

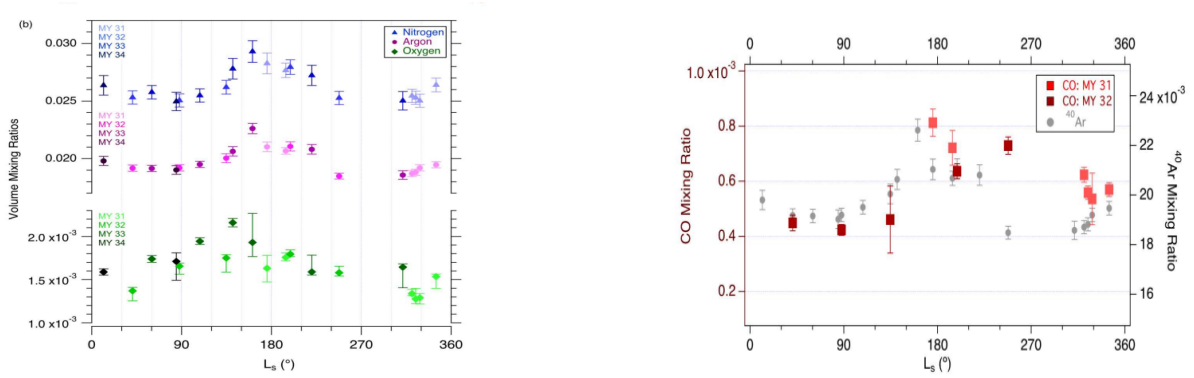

Figure 1.6: VMR seasonal trends

with the formation of the southern polar cup. Even if fluctuations in VMR (Volume Mixing Ratio) of CO_2 due to seasonal and diurnal cycles are large, carbon dioxide is so abundant that VMR only varies by 1 % around the average value of 95.1 %.

The decrease of the relative amount of CO_2 in the Mars atmosphere shows a lag with respect to the decrease of the average surface pressure, in the range of 20 - 40° of areocentric longitude (L_S) when the surface pressure approaches the annual minimum during summer. This phenomenon is explained in reference [41], by the fact that the mass is redistributed hemisphere-to-hemisphere during the sublimation or condensation of polar caps. Transport acts rapidly to maintain pressure equilibrium, but the Volume Mixing Ratio varies afterwards because the process of mixing acts slower.

Argon (^{40}Ar), nitrogen (N_2), oxygen (O_2) and carbon monoxide (CO) are the four most abundant non-condensable gases at Mars surface atmospheric conditions. For this reason, they are not expected to deposit or sublimate from the solar caps. However, these molecules present seasonal trends in VMR as a response to the mixing of air masses during the seasonal CO_2 cycle. Moreover, unexplained effects involve O_2 and CO.

Surface pressure maxima happen about $L_s = 60°$ and $L_s = 250°$, after the sublimation of northern and southern caps. VMR minima of inert gases ^{40}Ar and N_2 present a lag with respect to surface pressure maxima, of about $L_s = 30°$, suggesting a lower mixing timescale. According to SAM measurements presented by [41], Argon and nitrogen seasonal variations of VMR are about 10 %. Oxygen VMR does not seem to follow the same seasonal pattern presented by nitrogen and argon, especially at the beginning of the Martian year. In addition, significant interannual variability is present.

Prior to investigating the problem of the design of a fixed-wing UAV for Martian flight, the draft of a simple analytical model of the Mars atmosphere is required. To this aim, a simple Martian atmospheric model can be found in reference [16], developed by NASA.

This model has been implemented in MATLAB.

Before the draft of the simplified model, it is necessary to understand whether the continuum assumption can be used or it is violated at the Martian atmospheric conditions. The Knudsen number, defined as the ratio between the mean molecular free path λ and the characteristic length scale L of the considered problem, must be small ($Kn = \frac{\lambda}{L} << 1$). If this relation is satisfied, the continuum model holds.

The typical values of the mean molecular free path at Mars surface atmospheric condition are about $\lambda \simeq 10\ \mu m$, according to Bardera, Sor, and García-Magariño [7]. The characteristic length scale L is the mean aerodynamic chord of the UAV, it can be assumed between $0.5 \leq L \leq 1\ m$. Hence, the Knudsen number assumes values close to $Kn = 2 \times 10^{-5} << 1$. This implicates that the continuum model holds.

NASA simplified model for Mars atmosphere is reported by the following equations (1.15), (1.16) and (1.17)

$$\text{for h} < 7000 \text{ m} : \begin{cases} T = -31 - 0.000998h \\ P = 0.699 \cdot exp(-0.00009h) \end{cases} \tag{1.15}$$

$$\text{for h} \geq 7000 \text{ m} : \begin{cases} T = -23.4 - 0.00222h \\ P = 0.699 \cdot exp(-0.00009h) \end{cases} \tag{1.16}$$

$$\rho = \frac{P}{0.1921(T + 273.15)}, \tag{1.17}$$

with altitude h in [m], atmospheric density ρ in $[\frac{\text{kg}}{\text{m}^3}]$, pressure P in [kPa] and temperature T in [°C] .

Trends of density, temperature and pressure with altitude are shown by figure 1.7.

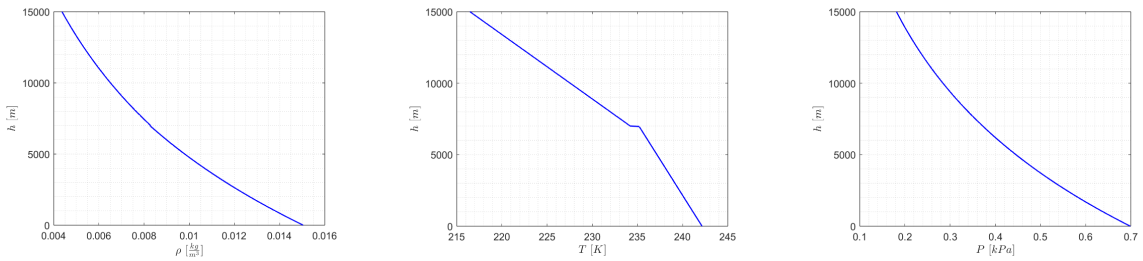

(a) Density (b) Temperature (c) Pressure

Figure 1.7: Mars Atmospheric Model

The atmospheric model assumes the following values of temperature, pressure and density, at 0 m altitude: $T_{\mathrm{h}=0\,\mathrm{m}} = 242.15$ K; $P_{\mathrm{h}=0\,\mathrm{m}} = 699$ Pa; $\rho_{\mathrm{h}=0\,\mathrm{m}} = 0.0150 \quad \frac{\mathrm{kg}}{\mathrm{m}^3}$;

For the assessment of the aerodynamic performance of the UAV, the Reynolds and Mach numbers must be computed for each flight condition, therefore, the computation of the dynamic viscosity and the speed of sound are discussed hereafter.

Regarding the speed of sound, the specific heat ratio γ on Earth is constant up to a few MHz at ambient pressure, as shown by reference [9]. Hence, the speed of sound does not vary with frequency near the surface. However, at the low atmospheric pressure of Mars surface, which is in the order of 600 Pa, the continuum theory holds, but energy exchanges at molecular scales act differently. Part of the energy associated with the translational motions of molecules is spent on the excitation of inner degrees of freedom (vibrational and rotational modes).

The relaxation of the rotational motion happens instantaneously, instead the relaxation of the vibrational modes occurs over a longer timescale. This phenomenon is governed by the relaxation frequency $f_R = \frac{1}{\tau_R}$, with τ_R the relaxation time. At 600 Pa, on Mars, the relaxation frequency is about $f_R = 240\ Hz$.

Two different speeds of sound appear, depending on whether the vibrational mode is activated or not. In fact, at frequencies f $< f_R$, all modes are equally excited. This implicates that there are seven degrees of freedom, given by: three translational modes; two rotational modes; and one doubly-degenerate vibrational mode. As a result, the specific heat ratio is equal to $\gamma = \frac{9}{7} = 1.2857$. Instead, at frequencies f $> f_R$ there is no sufficient time to relax the vibrational mode, this implicates that there are only five active degrees of freedom and $\gamma = \frac{7}{5} = 1.4$.

Preseverance rover of Mission to Mars 2020 is equipped with SuperCam, a laser-induced breakdown spectroscopy (LIBS) that analyses the chemistry of Mars at distances from 1.5 to 7 m and permits to detect acoustic signals. Preseverance is also equipped with a special microphone, called EDLCAM. Speed of sound measurement were conduct by NASA making use of LIBS and EDLCAM. Experiments were carried out considering that Igenuity's blade behaved like an harmonic source centred around 84 Hz, therefore at a frequency minor than the relaxation frequency $f < f_R$. SuperCam recorded a speed of sound close to $c = 237.7 \pm 3\frac{\mathrm{m}}{\mathrm{s}}$, as presented by Maurice, Chide et al. [27]. An estimated wind speed of about $v_{\mathrm{wind}} = 2.5\frac{\mathrm{m}}{\mathrm{s}}$ was present during the experiment, therefore the true measured speed of sound was close to $c = 240\frac{\mathrm{m}}{\mathrm{s}}$.

As mentioned before in this section, the atmosphere of Mars is composed on average

by 95.1 % carbon dioxide, 2.59 % nitrogen, 1.94 % argon, 0.161 % oxygen and 0.058 % carbon monoxide. The molecular weight $\mathcal{M}$ can be retrieved by means of a weighted average between the molecular weights of all constituents

$$\mathcal{M} = \sum_{i=1}^{N} w_i \mathcal{M}_i = w_{CO_2}\mathcal{M}_{CO_2} + w_{N_2}\mathcal{M}_{N_2} + w_{Ar}\mathcal{M}_{Ar} + w_{O_2}\mathcal{M}_{O_2} + w_{CO}\mathcal{M}_{CO} \approx 43.34 \frac{\text{g}}{\text{mol}} \tag{1.18}$$

The universal gas constant is $R = 8314.463 \frac{\text{J}}{\text{molK}}$. The gas constant $R_{\text{gas}} = \frac{R}{\mathcal{M}}$ is equal to $R_{\text{gas}} = 191.84 \ \frac{\text{J}}{\text{kgK}}$. As a result, the speed of sound (under the assumption of polytropic ideal gas) can be computed as $c = \sqrt{\gamma R_{\text{gas}} T}$. At 0 m altitude the speed of sound assumes the value of $c = 244.39 \frac{m}{s}$, which is roughly 28 % lower than the speed of sound of air at sea level $c = 340.29 \frac{m}{s}$.

Mars acoustics provides few other peculiarities, it is interesting to consider the acoustic impedance at Mars atmospheric conditions, $Z = \rho c$, as presented by table 1.1.

Gas	T [°C]	P [Pa]	ρ $\left[\frac{\text{kg}}{\text{m}^3}\right]$	c $\left[\frac{\text{m}}{\text{s}}\right]$	Z $\left[\frac{\text{Pas}}{\text{m}}\right]$
CO_2	20	101 325	1.839	266.2	489.6
CO_2	- 31	699	0.015	244.4	3.666
Air	20	101 325	1.205	340	413.7

Table 1.1: Acoustic impedance on Mars and Earth

The acoustic impedance of the Martian atmosphere, approximated with Z_{CO2} is two order of magnitude lower than Z_{air} on Earth. This means that signals on Mars are roughly 20 dB weaker than the sound produced by the same source on Earth.

The dynamic viscosity μ as function of temperature, and therefore of altitude, is required for the assessment of the Reynolds number at all flight conditions. The characterisation of the dynamic viscosity as function of the temperature is represented by Sutherland's Law:

$$\begin{cases} \mu = \mu_0 \left(\frac{T}{T_0}\right)^{\frac{3}{2}} \frac{(T_0+S)}{(T+S)} \quad \text{Pas} \\ T_0 = 293.15 \text{ K} \\ \mu_0 = 1.48 \cdot 10^{-5} \text{ Pas} \\ S = 240 \text{ K} \end{cases} \tag{1.19}$$

The dynamic viscosity of Mars atmosphere at 0 metres altitude assumes the value of $\mu = 1.2286 \times 10^{-5}$ Pas.

1.1.5. Timeline of Mars exploration and state-of-the art of Martian flight

The exploration of Mars has a long history, with more than 45 missions from 1960 to present day [46] [26].

The first successful mission to Mars was NASA's Mariner 4, launched on 28th November 1964. Mariner 4 performed a flyby on the 15th of July 1965, flying as close as 9844 kilometers to the surface of Mars. It took 21 images of the Red Planet. It was followed by missions Mariner 6 and Mariner 7 (1969) that collected respectively 75 and 126 images of the Red Planet.

Mariner 9 Orbiter (1971) was the first spacecraft to map the entire planet, it discovered tectonic structures, giant volcanoes and valleys. It collected 7329 images. Viking 1 Orbiter (1975) returned over 36,000 images and Viking 1 Lander returned the first image from the surface of Mars and conducted soil experiments.

Mars Global Surveyor (1996) mapped Mars and its topography, studied indications of Mars' wetter past. Mars Pathfinder (1996) brought a new approach to low-cost exploration of Mars, the first to successfully transport a rover, called Sojourner. Mars Express/Beagle 2 Lander (2003), was the first ESA mission on Mars.

In the last two decades, other countries contributed to the exploration of the Red Planet, such as China, India and the United Arab Emirates (UAE).

Recent space missions to Mars include Tianwen-1 Orbiter and Zhurong Rover by China (2020) and NASA Mission to Mars 2020, with the objectives to search for signs of ancient life and the collection of samples for future return to Earth.

The near future will see the launch of several missions to Mars: India's Mars Orbiter Mission 2 (MOM-2), planned to launch in 2024; Escape and Plasma Acceleration and Dynamics Explorers (EscaPADE) by the US, expected to launch in August 2024; Exomars (ESA and Roscosmos) to search for evidence of past or present microscopic life on Mars, planned for 2024 but delayed indefinitely due to Russian invasion of Ukraine in 2022.

Mars Helicopter - Ingenuity

The state-of-the art considering UAVs for Martian atmospheric flight is represented by Ingenuity. The Mars Helicopter, is a small, autonomous rotorcraft developed by NASA for the Mission to Mars 2020. It has been transported to the surface of the Red Planet attached to the belly of Perseverance, an autonomous rover designed to collect samples of rocks and sediment for potential return to Earth by later missions.

Figure 1.8: Ingenuity

Ingenuity is a technological demonstrator, having no specific role to support the Mars 2020 mission but sets few key objectives, that according to NASA are:

1. Prove powered flight in the thin atmosphere of Mars, where it is much harder to generate lift.
2. Demonstrate miniaturized flight technology by reducing the size of the onboard computers and electronics, in order to limit the MTOM of the helicopter.
3. Operate autonomously and make use of solar power to recharge batteries. Rely on internal heaters to maintain operational temperatures during the cold Martian nights. Moreover, after receiving commands from Earth relayed through the rover, each test flight can be performed without real-time input from Mars Helicopter mission controllers.
4. Preview areas that could be of possible interest for the exploration by Perseverance rover.
5. Paving the way for future aerial explorations on Mars and, potentially, other space destinations.

Ingenuity has a maximum take-off mass of 1.8 kilograms, its height is about 49 centimetres. The rotor system is formed by two rotors, with counter-rotating blades of 1.2 metres

of diameter, and a maximum rotational speed of 2400 RPM. On the top of the Mars Helicopter, there is a small solar panel for the recharge of the battery system.

On 19th April 2021, for the first time in history, Ingenuity performed a remote controlled flight in an extra-terrestrial atmosphere. Up to November 2023, Ingenuity completed 66 flights for a total of 118.8 flying minutes, covering 14.9 km, and reaching altitudes as high as 24.0 m. Figure 1.9 shows the distance covered by Ingenuity on each mission (data from [48]):

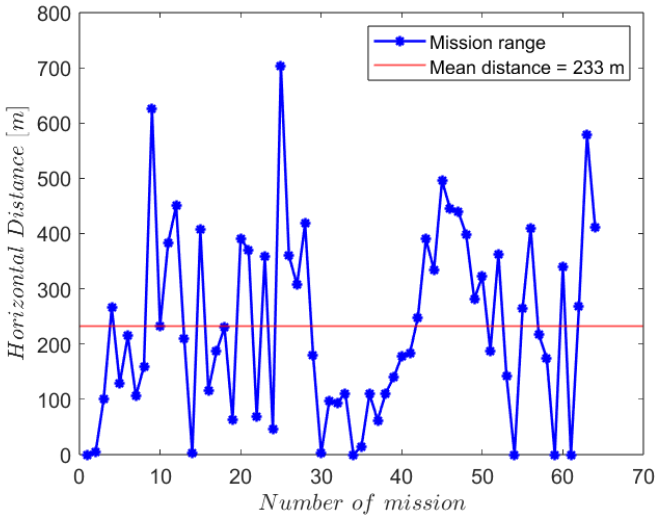

Figure 1.9: Distance flown by Ingenuity on each mission

Fixed-wing UAVs for Mars exploration

Fixed-wing UAVs may play a significant role in future Mars exploration, for several reasons. First, fixed-wing UAVs are more energy-efficient when compared to rotorcrafts. In fact, considering a steady-level flight condition, the main rotor of rotorcraft UAVs, tilting forward, must balance both the drag force and the weight, resulting in high shaft power demand. However, the propulsive system of a fixed-wing UAV must produce sufficient thrust to compensate for the drag force only, as the weight is all equilibrated by the lift force generated by the wing. In addition, it is typically possible to reach higher velocity.

Fixed-wing UAVs might be designed for efficient cruising. In case of propeller driven fixed-wing UAVs, by operating at the condition of maximum lift-to-drag ratio it is possible to maximize the mission range of the UAV. As a result, fixed-wing UAVs are able to cover larger distances in a faster, and more energy-efficient way, when compared to rotorcraft UAVs.

Fixed-wing UAVs might also offer support to rovers, by inspecting areas that may be of

scientific interest for the rover operations. In fact, operating at the condition of maximum endurance, fixed-wing UAVs can provide a real-time mapping of the areas in proximity to the rover, with low power demand.

Fixed-wing UAVs are also more indicate to carry larger payloads, when compared to rotorcraft UAVs.

The Mars planetary conditions present some challenges. The low atmospheric density at Martian conditions affect significantly the capability of fixed-wing UAVs to generate lift. In order to operate at Mars atmospheric conditions, aerodynamic surfaces must be larger, when compared to those for terrestrial applications. Moreover, the Martian glacial temperatures (-100 Celsius degrees) during the winter pose challenges for the operation of electronic components and batteries. The distance between Earth and Mars produces communication delays. The UAV must be equipped with a sophisticated system to operate completely autonomously and safely.

1.2. Terrestrial environment

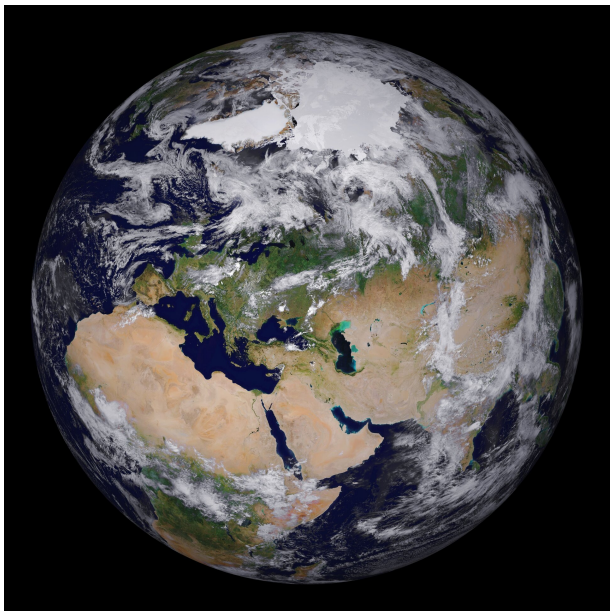

Figure 1.10: Earth

1.2.1. Atmosphere and solar irradiance

The principal constituents of the terrestrial atmosphere are reported by table 1.2, the reported data are from NOAA [47].

Gas	Symbol	Content
Nitrogen	N_2	78.084 %
Oxygen	O_2	20.947 %
Argon	Ar	0.934 %
Carbon dioxide	CO_2	0.035 %
Neon	Ne	18.18 ppm
Helium	He	5.24 ppm
Methane	CH_4	1.70 ppm
Krypton	Kr	1.14 ppm
Hydrogen	H_2	0.53 ppm
Nitrous oxide	N_2O	0.31 ppm
Carbon monoxide	CO	0.10 ppm
Xenon	Xe	0.09 ppm
Ozone	O_3	0.07 ppm
Nitrogen dioxide	NO_2	0.02 ppm
Iodine	I_2	0.01 ppm

Table 1.2: Composition of terrestrial atmosphere

The most abundant components are Nitrogen (78.084%), Oxygen (20.947%) and Argon (0.934%). A significant contribution is given by carbon dioxide (0.035%), risen significantly during the last decades due to climate change.

The molar mass of air ($\mathcal{M}_{air}$) can be computed as the sum of all the contributions given by its constituents, as reported by equation 1.20

$$\mathcal{M}_{\text{air}} = \sum_{i=1}^{N} w_i \mathcal{M}_i = w_{N_2}\mathcal{M}_{N_2} + w_{O_2}\mathcal{M}_{O_2} + w_{Ar}\mathcal{M}_{Ar} + w_{CO_2}\mathcal{M}_{CO_2} \approx 28.97 \frac{\text{g}}{\text{mol}}, \quad (1.20)$$

the gas constant of air assumes the value of $R_{\text{air}} = \frac{R}{\mathcal{M}_{\text{air}}} = 287\ \frac{\text{J}}{\text{kgK}}$.

Air is a mixture mainly composed by N_2 and O_2, both are linear polyatomic (diatomic) molecules. The activation temperature of the vibrational mode for nitrogen and oxygen are, respectively, $T_{\text{vib},\,N_2} = 3393\text{K}$ and $T_{\text{vib},\,O_2} = 2273\text{K}$, from reference [17].

Therefore, at terrestrial atmospheric conditions, the vibrational mode for N_2 and O_2 are never excited. As a consequence, air has 5 degrees of freedom (3 translational and 2 rotational). The isochoric specific heat assumes the value of $C_v = \frac{5}{2}R$, and the specific heat ratio is equal to $\gamma = \frac{7}{5} = 1.4$.

As an atmospheric model for the design of the terrestrial UAV, the International Standard Atmosphere has been used. The International Standard Atmosphere model is based on the following assumptions:

1. Air is considered as a polytropic ideal gas,
2. The static equilibrium holds,
3. The temperature profile is known.

Reference values for atmospheric pressure P, temperature T and density ρ are:

$$P_0 = 101325 \text{ Pa}; \quad T_0 = 288.15 \text{ K}; \quad \rho_0 = 1.225 \ \frac{\text{kg}}{\text{m}^3}; \tag{1.21}$$

International Standard Atmosphere model is reported by the following equations (1.22), (1.23):

$$\text{for h} < h_s = 11000 \text{ m } (Troposphere): \quad \begin{cases} T = T_0 + \lambda h \\ P = P_0 \cdot \left(\frac{T(h)}{T_0}\right)^{\frac{-g}{R\lambda}} \\ \rho = \rho_0 \cdot \left(\frac{T(h)}{T_0}\right)^{-\left(1+\frac{g}{R\lambda}\right)} \end{cases} \tag{1.22}$$

$$\text{for } 11000 \text{ m} \leq \text{h} \leq 20000 \text{ m } (Stratosphere): \quad \begin{cases} T = T_s \\ P = P_s \cdot exp\left(\frac{-g}{RT_s}(h - h_s)\right) \\ \rho = \frac{P}{RT} \end{cases} \tag{1.23}$$

with temperature gradient $\lambda = -6.5\frac{K}{km}$, gravitational acceleration $g = 9.81\frac{m}{s^2}$, gas constant $R = 287.05\frac{J}{kgK}$ and with altitude h in [m], atmospheric density ρ in $\left[\frac{\text{kg}}{\text{m}^3}\right]$, atmospheric pressure P in $[Pa]$, temperature T in [K] .

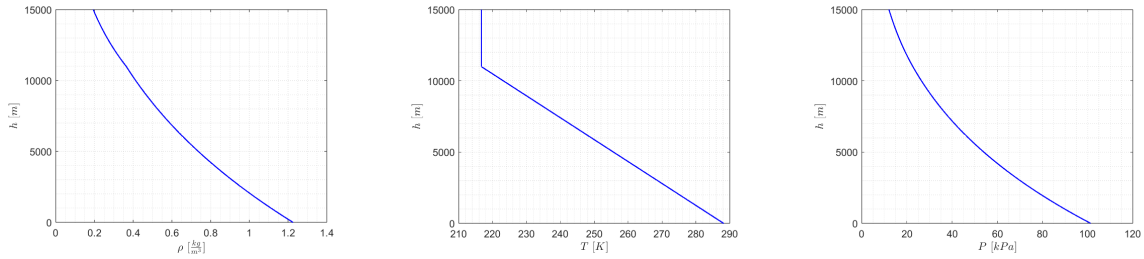

(a) Density (b) Temperature (c) Pressure

Figure 1.11: International Standard Atmosphere (ISA) model

For the modelling of the dynamic viscosity with temperature, therefore altitude, the Sutherland's Law for air has been used (1.24)

$$\begin{cases} \mu = \mu_0 \left(\frac{T}{T_0}\right)^{\frac{3}{2}} \frac{(T_0+S)}{(T+S)} \ \ Pa \cdot s \\ T_0 = 273.15 \ K \\ \mu_0 = 1.71 \cdot 10^{-5} \ Pa \cdot s \\ S = 211 \ K \end{cases} \tag{1.24}$$

In order to size the solar panels of the terrestrial UAV, it is necessary to characterise the solar irradiance on Earth. Similarly for the Mars case, full theoretical explanation is presented by reference [51].

The average distance Sun-Earth between perihelion and aphelion is equal to $r = 1$ AU.

The beam irradiance at the top of the atmosphere is presented by equation 1.1, hence $G_{\text{ob}} = 1371 \frac{\text{W}}{\text{m}^2}$. The beam irradiance at the top of the terrestrial atmosphere is more than double of the corresponding Martian case $G_{\text{ob,mean Mars}} = 590 \ \frac{\text{W}}{\text{m}^2}$.

In order to simplify the sizing of the solar power system of the UAV, the open-source software ModelE AR5 Simulations has been used [37]. The software requires in input the coordinates of the location where it is required to compute the daily insolation, along with the month of the year.

1.2.2. Connections between Martian and terrestrial flight

The design of a fixed-wing UAV for atmospheric Martian flight unites different challenges that are of great actuality for applications on Earth. Firstly, the solar energy is the only relatively abundant source of energy on Mars. Therefore, the UAV is required to

have self-charging capability, making use of solar panels, along with electric propulsion. In addition, due to the impervious terrain characteristics and the fact there are not prepared surfaces to permit take-off and landing, vertical take-off and landing solutions must be exploited. eVTOLs are of great actuality, especially referring to Urban Air Mobility (UAM). Moreover, the atmospheric conditions of Mars' surface are characterised by an extremely low density. Similar conditions on Earth are faced by High-altitude, long endurance UAVs (HALE). These aerial vehicles are commonly equipped with solar power systems to significantly extend the duration of their missions, that in some cases it is in the order of weeks.

eVTOLs

eVTOLs are of great actuality, as this innovative concept of electric aircrafts aims to solve the problems related to Urban Air Mobility (UAM) and Regional Air Mobility (RAM). Urban Air Mobility (UAM) is a new form of air transportation for passengers and goods across bustling cities in a safe, fast, flexible and sustainable way. UAM is fostered by the remarkable improvements achieved in the last few years in the fields of battery technology and electric propulsion. There is no clear definition of the typical mission range for UAM, however it can be assumed from 20 to 50 kilometres.

Vertical take-off and landing aerial vehicles are one of the most promising solutions also to the theme of Regional Air Mobility. RAM aims to provide a valid alternative to road transportation for regional trips. According to NASA [2], only 1.6 % of all trips in the range of 50 to 500 miles are taken by air, and 0.6 % of U.S. airports support 70 % of domestic air travel. eVTOLs might become in the next few years a valid alternative to road transportation for regional trips.

Several eVTOLs projects are undergoing worldwide, especially in Europe and in the United States. Some examples are given by: Lilium, Archer Aviation, Volocopter, Joby Aviation, Vertical Aerospace and many other companies. eVTOLs often adopt the use of distributed electric propulsion (DEP), by installing a set of propellers distributed all over the wingspan in order to enhance the dynamic pressure perceived by the wing with the scope to increment the lift.

(a) Lilium Jet (b) Archer Midnight

Figure 1.12: Lilium Jet and Archer Midnight eVTOLs

A considerable fraction of the undergoing projects adopt a tilt-rotor configuration, apart from Lilium Jet which makes use of orientable ducted fans. Both solutions are aimed to produce thrust by means of a Thrust Vectoring Systems. During vertical take-off and landing, the vertical thrust must produce a sufficient vertical force in order to lift the eVTOL, during transition to forward flight, the Thrust Vectoring Systems will progressively rotate up to reaching a condition that allows forward flight.

Tilt-rotors are more efficient than lift fans. As reported by Lilium [44], ducted fans incur in a 50% penalty in power consumption at hover, for the same weight. This affects only the hovering phase, that typically has a modest duration, considering the entire flight profile.

Figure 1.13: Lilium ducted fans

Ducted fans present the great advantage to significantly reduce the emitted noise, when compared to tilt-rotor architectures. Lilium affirms a 60 dB noise emission [31], measured at 100 m distance, during take-off and landing hover, which are the most critical phases in terms of noise emission. This architecture makes use of 36 ducted fans embedded over the trailing edge of the wing, exploiting the advantages of DEP and helping the flow over the suction side of the wing to stay attached over all the flight envelope. Fans are also

used for directional control and avoid the use of the rudder, which is not present in their aircraft. The absence of the rudder reduces weight and drag.

HALE aircrafts

High-altitude, long endurance aircrafts are a particular category of aerial vehicles designed to perform missions at high altitude (greater than 15000 metres) for a long period of time (in the order of weeks or months), and typically at low speeds. The uses are both civil and military. Most common civil missions are: weather monitoring, ocean and terrain imaging, border security. Two examples are given by manned platforms Solar Impulse 2 and unmanned Airbus Zephyr.

In order to fly for a so long period of time, HALE are usually solar-electric, therefore, the solar propulsive system is sized in a way that during the day it produces the power required by the aircraft during the cruising phase, or other phases in accordance with the flight profile, but also to recharge completely the batteries. Those, are then discharged during night. Exploiting this mechanism of recharge during the day and discharge during the night, theoretically, a sort of perpetual flight might be performed.

(a) Airbus Zephyr

(b) Solar Impulse 2

Figure 1.14: HALE platforms

Naturally, it is fundamental to minimise the power required during the cruising phase to allow solar-powered flight. To this aim, the wing geometry exhibits a high aspect ratio. Another crucial factor is weight, that has to be limited. Ultra-light aerostructures are used to minimise the MTOM of the aircraft. Solar Impulse 2 presents an airframe, fuselage and empennages that are made of thin-ply composites unidirectional tapes with areal densities from $\rho_{areal} = 25\frac{g}{m^2}$ to $\rho_{areal} = 100\frac{g}{m^2}$. UD tapes were then resin-impregnated during the process and converted into $\pm 45°$ preforms. Shell dors are made of rigid polyurethane foam, characterised by a density of $\rho = 27.5\frac{kg}{m^3}$. Windshields and windows are made of Covestro's transparent polycarbonate with a density of about $\rho = 1200\frac{kg}{m^3}$ [12].

Small UAS

Unmanned Aerial Systems (UAS) can fulfill several types of missions, from military to institutional and civil. Those include long-lasting surveillance, inspection and security of critical infrastructures. An example of small fixed-wing UAS is the one provided by Zipline for the medical delivery in remote regions of Africa.

Figure 1.15: Zipline Medical UAV

2 | Effects of planetary environment on the aerodynamics and the design of fixed-wing UAVs

This chapter evaluates how various terrestrial and Martian environments affect both the aerodynamic performance and overall design of a fixed-wing VTOL UAV.

2.1. Effects on the aerodynamics

Mars atmosphere is characterised by very low density, low pressure and glacial temperature. Due to the fact that the density decreases with an increase in altitude, the design cruising altitude for the mission of the Martian UAV, will be set to $h_{\text{cruise}} = 1000$ m, where $\rho_{\text{Mars,1000 m}} = 0.0138 \ \frac{\text{kg}}{\text{m}^3}$ in order to guarantee, according to Mars topography, the possibility to explore the vast majority of the Red Planet, still avoiding lower density regions.

As mentioned during the introduction, this thesis will consider also an UAV conceived to replicate on Earth, a similar mission to the one of the Martian UAV. To assess some preliminary considerations about aerodynamics, especially in terms of Reynolds and Mach number regimes, the draft of test case has been exploited, with the following framework:

1. altitude has been set equal to h = 1000 m. Therefore, from the atmospheric models, the density, pressure, temperature and dynamic viscosity have been fixed;
2. the mean aerodynamic chord (M.A.C.) of the UAV, has been set arbitrarily equal to one metre. It is later indicated also as L, the reference length;
3. True airspeed, arbitrarily imposed to ($U_\infty = 50 \ \frac{\text{m}}{\text{s}}$)

2.1.1. Low Reynolds aerodynamics

Table 2.1 compares the Reynolds numbers at Martian and terrestrial atmospheric conditions, considering the same altitude, reference length, and freestream velocity.

Planet	Density	Airspeed	M.A.C.	Dynamic Viscosity	Re $= \frac{\rho U_\infty L}{\mu}$
Mars	$\rho = 0.0138 \frac{\text{kg}}{\text{m}^3}$	$U_\infty = 50 \frac{\text{m}}{\text{s}}$	L = 1 m	$\mu = 1.22 \times 10^{-5}$Pas	Re = 56500
Earth	$\rho = 1.1116 \frac{\text{kg}}{\text{m}^3}$	$U_\infty = 50 \frac{\text{m}}{\text{s}}$	L = 1 m	$\mu = 1.76 \times 10^{-5}$Pas	Re = 3150000

Table 2.1: Reynolds Number Comparison at 1000 m altitude

The Reynolds number on Mars is significantly lower (roughly two orders of magnitude lower) than the one of the terrestrial case. The Reynolds number for small UAVs on Mars is in the order of the tens of thousands. Therefore, low Reynolds aerodynamics will be discussed later in this section.

Still considering L and U_∞ of the previous example, the ratio between the Reynolds number on Mars with the Reynolds number on Earth depends by the density-to-dynamic viscosity ratio $\left(\frac{\rho}{\mu}\right)$. Trends of $\left(\frac{\rho}{\mu}\right)$ with altitude, on Mars and Earth are presented in figure 2.1.

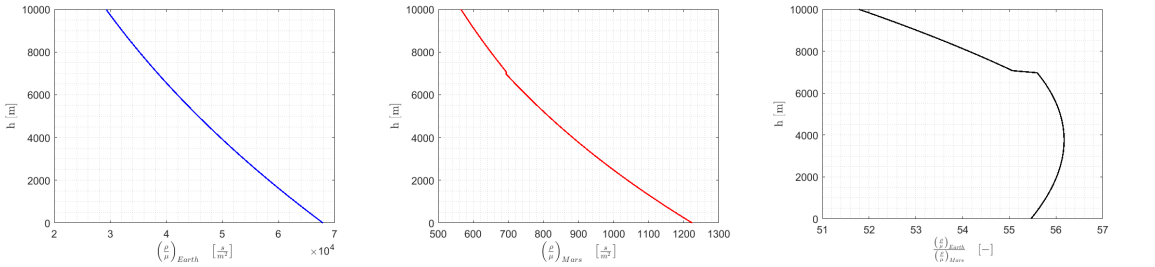

(a) Terrestrial case (b) Martian case (c) Ratio between $\left(\frac{\rho}{\mu}\right)_{\text{Earth}}$ and $\left(\frac{\rho}{\mu}\right)_{\text{Mars}}$

Figure 2.1: Density to viscosity ratio variation with altitude

Results show that the Reynolds number on Earth is about 55 times the one on Mars, for the same reference length and flight condition. The ratio between the Reynolds number on Earth over the Reynolds number on Mars, $\frac{\left(\frac{\rho}{\mu}\right)_{\text{Earth}}}{\left(\frac{\rho}{\mu}\right)_{\text{Mars}}}$ presents a slight increase from h = 0 m to h $\simeq$ 3700 m. Over that altitude, it decreases.

In any case the Reynolds number of Mars is extremely low compared to the equivalent on Earth. A cruising altitude of $h_{\text{cruise}} = 1000\ m$ is considered by this work as an acceptable

trade-off between the possibility to explore a wide area of the Red Planet, and to avoid extremely low densities. The cruising altitude will be at a lower altitude than the service ceiling, that will be $h_{\text{ceiling}} \geq 3000m$, so in case it would be required to reach higher altitudes, that possibility is still present.

It might be useful to try to increase the Reynolds number at the cruising condition, in order to avoid the low Reynolds regime and obtain better aerodynamic performance. To this aim, a possibility might be represented by a high-speed flight. Increasing the design cruising speed could be achievable, but the speed of sound on Mars is low, hence some limitations are present, as shown in section 2.1.2.

Another solution might be to increase the mean aerodynamic chord of the wing, but,for a given wing surface, it leads to a reduction in the wing aspect ratio $\left(\lambda = \frac{b^2}{\text{s}}\right)$. Therefore, in accordance with Prandtl's theory, the induced drag component will increase.

The atmospheric flight of UAVs on Mars would be at low Reynolds regime, which usually is defined as Re $<$ 100 000. This causes rapid performance degradation for conventional airfoils due to laminar separation without reattachment. Unconventional shapes are required, characterised by sharp leading edges and very low thickness to chord ratio.

The performance of conventional airfoils start to deteriorate when the Re is lower than the critical Reynolds number, roughly close to $Re_c \simeq 500\,000$. When the Reynolds number decreases, the relative force of viscous forces with respect to inertia forces increases. Disturbances are more and more damped, and laminar to turbulent transition is delayed. As a result, on the suction side of the airfoil, the flow is usually laminar even after the point of pressure recovery. The laminar boundary layer is not prone to sustain large adverse pressure gradient, therefore the flow separates. Separation produces a sharp increase in pressure drag component. Consequently, separation results in a decrease of the lift coefficient. In the end, the maximum lift-to-drag ratio for conventional airfoils at low Reynolds number is very poor.

Cambered plates outperform conventional airfoils in the low Reynolds regime. Hoerner book [19] presents a comparison between a conventional airfoil (N60), and cambered plates.

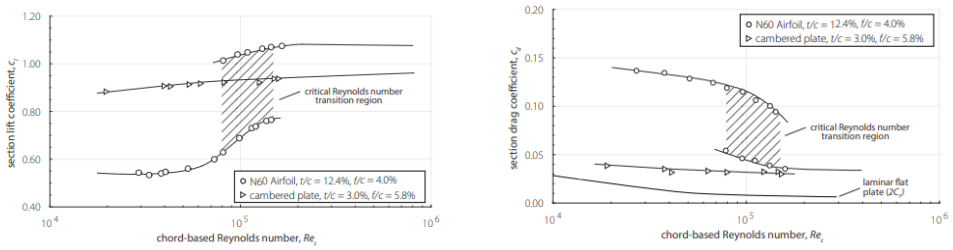

(a) C_l versus Re (b) C_d versus Re

Figure 2.2: Hoerner: C_l and C_d versus Re at constant α

Cambered thin airfoils at low Reynolds regime, and for a given α, show better performance both in terms of higher C_l and lower C_d with respect to conventional airfoils.

Sharp leading edges produce a high adverse pressure gradient at the leading edge, enforcing flow separation and promoting the shedding of vortices. Those vortices can reduce the total flow separation and facilitate laminar-turbulent transition and turbulent reattachment of the boundary layer in the form of an unsteady separation bubble.

A simplified scheme of the laminar separation bubble (LSB) is shown in figure 2.3

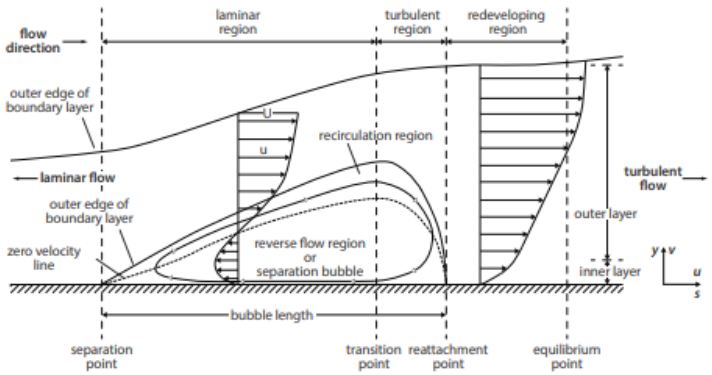

Figure 2.3: Laminar separation bubble

The formation of the LSB produces a non-linearity in the (C_l, α) curve, at low angles of attack. The separated region at low Re for an airfoil with sharp leading edge will be smaller than the separated region that appears on conventional airfoils. This justifies better C_l and C_d performances.

Two high-performance airfoils for the low Reynolds number regime are the Ishii airfoil and the Selig-Donovan 7003.

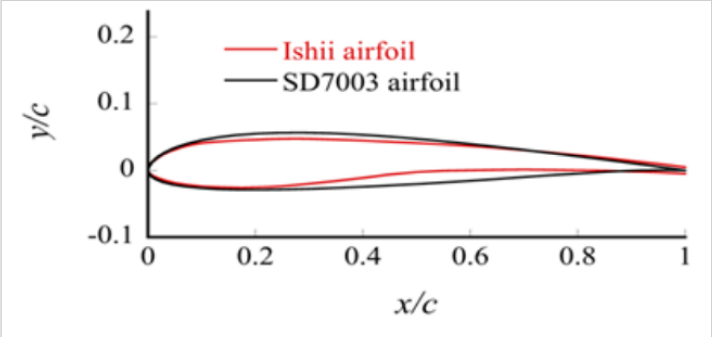

Figure 2.4: SD7003 and Ishii airfoils

Ishii is characterised by a maximum thikness-to-chord ratio $\frac{t}{c} = 7.1$ %, located at 25 % of the chord, and with a maximum camber of 2.3 %. SD7003 has a maximum thikness-to-chord ratio $\frac{t}{c} = 8.5$ %, located at 24 % of the chord, and with a maximum camber of 1.5 %.

Several studies have been performed over those two airfoils at low Reynolds number by Anyoji [3], for a Reynolds numbers from Re = 23 000 to Re = 60 000. In that framework Large Eddy Simulations were used.

At Re = 23 000, both airfoils present a non-linearity at $\alpha = 4°$ and a maximum lift angle of attack at $\alpha = 8°$. Ishii outperforms the SD7003 both in terms of $C_{l\,\max}$ (0.90 versus 0.75), both in terms of maximum lift-to-drag ratio, respectively about 15 versus 10. Those trends have been verified by Anyoji for all Reynolds numbers taken into account. Therefore, Ishii has better aerodynamic performance than SD7003 in general at that Reynolds regime.

Work by Anyoji et al. [4] at Re = 23 000 presented that Ishii produced a high lift coefficient even at low angles of attack. This is due to the fact that the flow was attached for a large percentage of the suction side and a small trailing-edge separation occured. The separation point moved towards the leading edge with an increase of the angle of attack. Reattachment was produced at $\alpha = 4°$, resulting in the non-linearity in the C_l, α curve.

In that framework, Ishii outperformed both a NACA0002 and a NACA0012 due to:

1) The camber on the pressure side, leading to a sort of very small rear loading

2) An extended flat part on the suction side, that reduces strong adverse pressure gradients and postpones separation

3) A small radius shape of the leading edge, that produces a suction peak

These features are shown by figure 2.5:

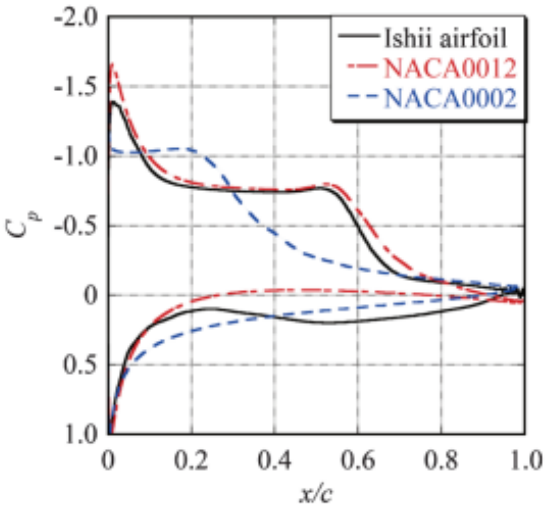

Figure 2.5: Ishii: $(C_p, \frac{x}{c})$ at $\alpha = 6°$

2.1.2. Compressibility effects

Martian atmosphere (indicated hereafter as M.A.), has a lower specific heat ratio with respect to air ($\gamma_{\text{MA}} < \gamma_{\text{air}}$), lower gas constant ($R_{\text{MA}} < R_{\text{air}}$) and lower temperature at a same altitude. Consequently, at the same altitude, the speed of sound $c = \sqrt{\gamma \text{R}}$ is significantly lower on Mars.

Table 2.2 compares the speeds of sound on Mars and on Earth for the example presented in the previous section 2.1.1.

Planet	**Velocity**	**speed of sound**	**M** $= \frac{U_\infty}{\sqrt{\gamma \mathbf{R}}}$
Mars	$U_\infty = 50 \frac{\text{m}}{\text{s}}$	$c = 336.43 \frac{\text{m}}{\text{s}}$	Ma $= 0.149$
Earth	$U_\infty = 50 \frac{\text{m}}{\text{s}}$	$c = 243.89 \frac{\text{m}}{\text{s}}$	Ma $= 0.205$

Table 2.2: Mach Number Comparison at 1000 m altitude

Therefore, for this example, the Mach number on Mars will be 38 % higher than on Earth.

Figure2.6 presents the variation of the speed of sound with altitude for air, according to the ISA model and the Martian atmospheric model.

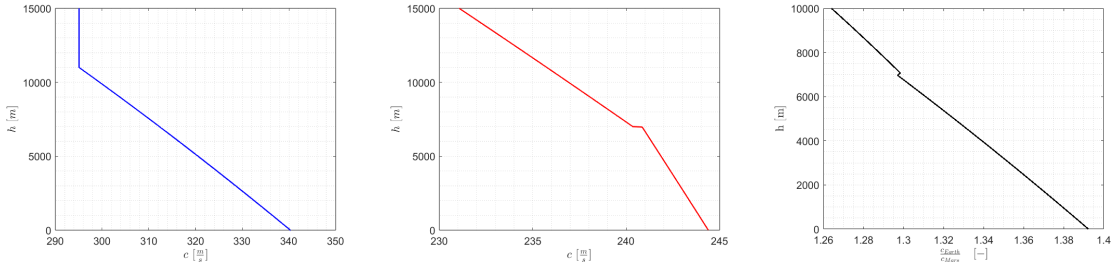

(a) Speed of sound on Earth (b) Speed of sound on Mars (c) Speed of sound ratio

Figure 2.6: speed of sound variation with altitude

Figure 2.6 shows that the speed of sound on Mars decreases with a moderate slope from $h = 0$m to $h = 7000$m, over that altitude the slope increases.

An example of compressible flow in the Martian environment is given by the Mars Helicopter, which is equipped with a co-axial rotor of 1.8 m diameter. Rotors are spaced apart at approximately 8–9 % of the diameter and are designed to operate at speeds up to 2800 RPM. As a result, the tip wing velocity is equal to $v_{\text{tip}} = 177\frac{\text{m}}{\text{s}}$, which corresponds to a tip Mach number of $M_{\text{tip}} = 0.76$.

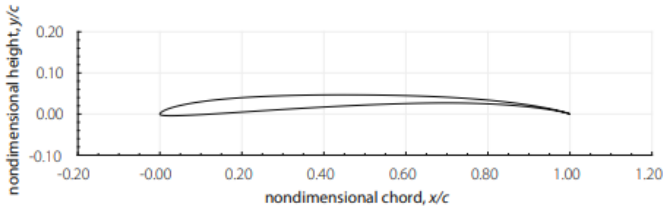

Figure 2.7: Outboard airfoil of the Mars Helicopter

Mach number effects on a flat plate and on a NACA0012-34 were investigated by Anyoji, Nagai, Numata and Asai [5], at a Reynolds number equal to $Re = 1.1 \cdot 10^4$ maintained constant for all experiments, and a Mach number from $M = 0.09$ to $M = 0.61$. Experiments were conducted in the Mars Wind Tunnel at Tohoku University. Results indicate that for the flat plate, lift curves are little affected by Mach number changes up to the case $M = 0.61$, when the C_l is slightly increased. Compressibility stabilizes the separated shear layer and delays laminar to turbulent transition, and reattachment.

For the NACA0012-34 case, at low angles of attack the aerodynamic performance are not affected by Mach number variations. However, for $\alpha > 7°$, the lift coefficient decreases with the increase in Mach number, in opposition to Prandtl-Glauert rule.

This pheonomenon is explained by the fact that in all cases, for $\alpha < 6°$, separation

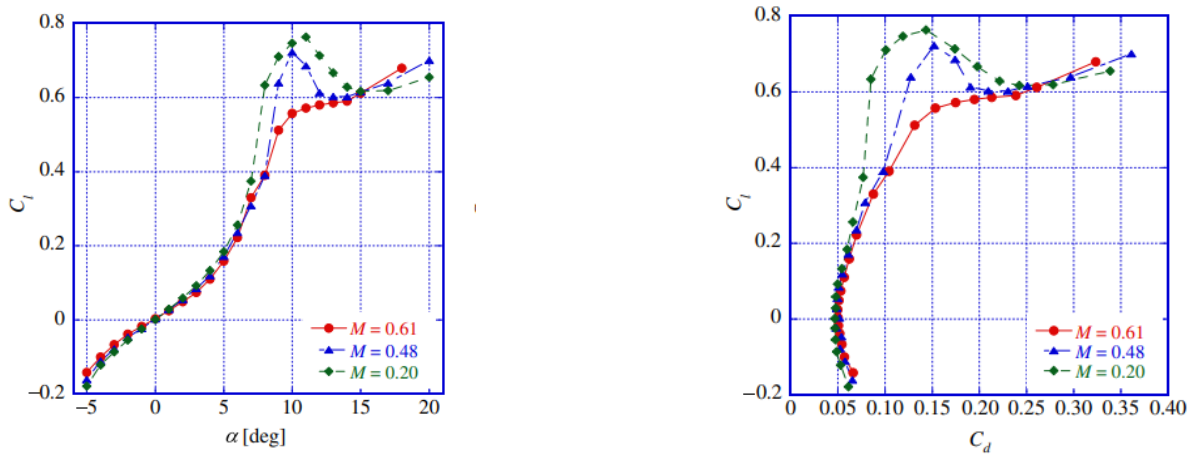

Figure 2.8: Mach effects at low Reynolds on a NACA0012-34

happens without reattachment, starting from the trailing edge and moving upstream with the increase in angle of attack. At $\alpha = 6°$, a separation bubble forms, only in the case $M = 0.21$, instead the flow remains separated for $M = 0.48$ and $M = 0.61$. Separation bubble forms at $\alpha = 8°$ for the case $M = 0.48$. For $M = 0.61$ the flow reattaches at $\alpha = 13°$.

Figure 2.8 shows the lift curve and drag polar for the NACA0012-34 at $Re = 1.1 \cdot 10^4$ and M = 0.2, M = 0.48, M = 0.61.

2.2. Effects on the design

The effects of atmospheric density ρ and planet gravitational acceleration g on the design of a fixed-wing UAV, and consequently on its performance and mission profile, have been evaluated in this section.

The Martian UAV is designed to carry out a scientific mission for the large-scale aerial exploration of Mars, therefore, the mission range has been identified as a fundamental parameter, to be maximised.

During the conceptual design phase of a propeller driven aircraft, or in a similar manner, a fixed-wing UAV two key parameters are defined: Wing loading and power loading. Wing loading is the ratio between the maximum take-off weight W in [N] and the wing surface in [m^2] and it is usually indicated as $\left(\frac{W}{S}\right)$. Power loading $\left(\frac{W}{P_b}\right)$ is the ratio between the maximum take-off weight W in [N] and the installed shaft power P_b in [W]. Wing loading is directly associated to the wing sizing, and typically the most strict condition is represented by the stall condition. Power loading is related to the maximum shaft power

that it is necessary to install on the UAV. The sizing condition is the vertical take-off.

The acceleration of gravity on Mars is different from the terrestrial, therefore it was preferred to consider the wing loading in terms of mass ($\frac{M}{S}$) and not weight ($\frac{W}{S}$), as usual. Similarly, the power loading is modified to ($\frac{M}{P_b}$), instead of ($\frac{W}{P_b}$).

Wing loading and power loading will be the key parameters during the conceptual design phase. In that circumstances, a Sizing Matrix Plot (SMP) is built to graphically report all constraints associated to the principal flight conditions such as take-off, cruise, stall, landing, fastest climb, steepest climb, coordinated turn, service ceiling. SMP allows to draft all constraints as function of wing loading and power loading and to retrieve an optimal solution. This is the one that maximises the wing loading, and minimises power loading, considering all solutions that satisfy all constraints. This thesis considers the vertical take-off and landing, therefore those two phases are analyzed in a different manner with respect to what concerns the design of traditional fixed-wing aircrafts or UAVs.

2.2.1. Range: cruising condition

The cruising phase is supposed to cover the vast majority of the flight profile, hence in order to maximise the mission range is necessary to maximise the range at cruising condition.

Starting from a point-mass model of a free standing aircraft in equilibrium of forces and moments in cruise, the following set of equations must be satisfied

$$\begin{cases} L = W \\ T = D \\ M_G = 0, \end{cases} \tag{2.1}$$

where L is the lift, T is the thrust generated by the UAV, D is the drag force, and m_G is the pitching moment about the centre of gravity.

The Martian environment is characterised by a very low density ($\rho = 0.0150 \, \frac{kg}{m^3}$ at a reference altitude of 0 metres). Aerodynamic forces are directly proportional to density, hence an extremely low density affects the capability of the UAV to generate sufficient lift. At the same time, the drag force will be low by the effects of the low density atmosphere. For this reason, it might be assumed that the power required to fly on Mars during the cruise phase will be low.

The Mars UAV must be able to carry out a long-range exploration of the Red Planet.

During the cruising phase, range can be estimated following the approach used by De Vries, Hoogreef and Vos [13] for a full-electric aircraft, shown by equation (2.2)

$$R = \eta_{\text{tot}} \frac{e^*_{\text{spec}}}{1000\text{g}} \left(\frac{L}{D}\right) \left(\frac{M_{\text{battery}}}{\text{MTOM}}\right), \tag{2.2}$$

where the range R is expressed in [km], η_{tot} accounts for propulsive, transmission and gearbox (if present) and electric motor efficiencies ($\eta_{\text{tot}} = \eta_p \eta_{tr} \eta_m$), e^*_{spec} is the battery specific energy in $[\frac{J}{kg}]$, $\left(\frac{L}{D}\right)$ is the lift-to-drag ratio, M_{battery} is the mass of the battery package in [kg] and MTOM is the maximum take-off mass of the aircraft in [kg].

A sensitivity study on range has been carried out, considering as variables the gravitational acceleration g and battery specific energy e^*_{spec}. The ratio between the mass of the battery and the MTOM has been assumed equal to 0.2, along with an electric motor efficiency of 0.9 , and a propulsive efficiency of 0.65. The lift-to-drag ratio has been considered equal to $\frac{L}{D} = 15$. Results are shown by figure 2.9

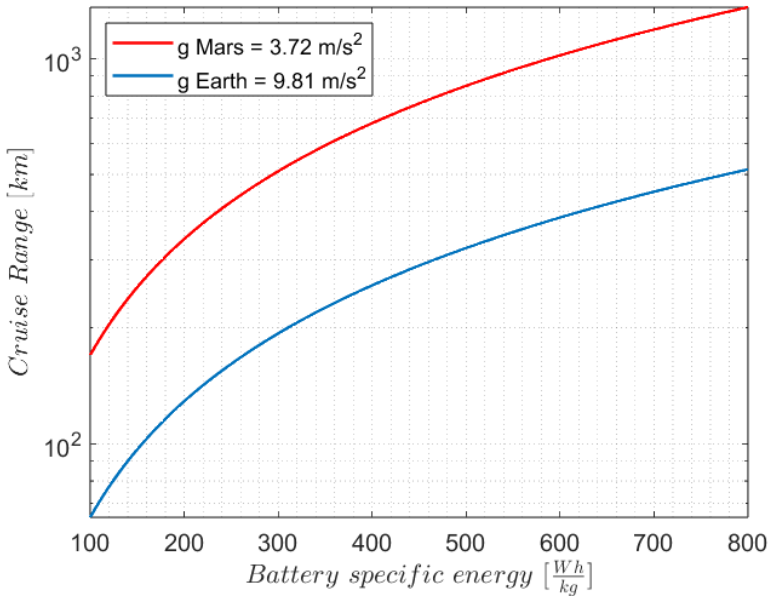

Figure 2.9: Range variation with specific energy and acceleration of gravity

As expected, battery packages with high specific energy are required in order to enhance the mission range. Thus, state-of-the-art battery technology must be used in order to extent the mission range as long as possible. To this aim, lithium sulfur and lithium metal oxide batteries will be discussed. The low gravitational acceleration at Mars surface ($g_{\text{Mars}} = 3.72 \frac{\text{m}}{\text{s}^2}$) with respect to the one on Earth ($g_{\text{Earth}} = 9.81 \frac{\text{m}}{\text{s}^2}$), facilitate to perform longer missions.

2.2.2. Wing sizing: stall condition

Concerning wing loading $\left(\frac{W}{S}\right)$, the sizing condition is often dictated by the stall. At stall the following relation is valid (2.3)

$$\frac{M}{S} = \frac{1}{2}\frac{\rho}{g} v_{\text{stall}}^2 C_{L\,\max}, \tag{2.3}$$

considering ρ as the atmospheric density at the altitude of the UAV in $\left[\frac{\text{kg}}{\text{m}^3}\right]$, and v_{stall} the stalling speed expressed as true airspeed, in $\left[\frac{\text{m}}{\text{s}}\right]$.

To investigate the effects of planetary atmospheric density and gravitational conditions, a test case has been considered where the maximum lift coefficient $C_{L\,\max}$ and the stalling speed v_{stall} are fixed, and the wing loading depends only by the density-to-gravity ratio $\left(\frac{\rho}{g}\right)$. To this aim, the maximum lift coefficient has been set equal to $C_{L\,\max} = 1.0$ and the stalling speed $v_{\text{stall}} = 10\ \frac{\text{m}}{\text{s}}$. Due to the linear relation between density-to-gravity ratio and wing loading, an increase in density produces a higher wing loading, meaning that if the MTOM of the aircraft is known and fixed, the wing surface could be reduced. This clearly implicates a reduction in wetted area along with, in general, a lower mass. In an opposite way, a larger acceleration of gravity reduces the wing loading, thus a bigger wing surface is required to satisfy the stalling constraint.

Figure 2.10 shows, in logarithmic scale, the results of the sensitivity study on wing loading with the variation of density and gravitational acceleration.

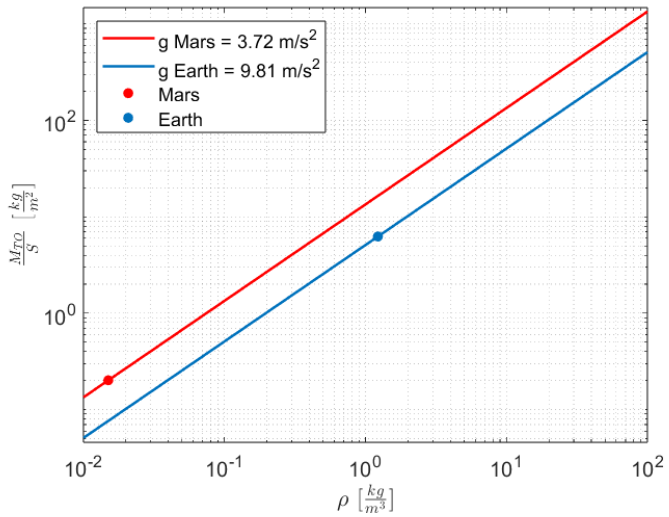

Figure 2.10: Wing loading variation with density and acceleration of gravity

The Blue point in the figure corresponds to terrestrial conditions, and the Red Point to the

Martian ones. For Earth, a density of $\rho_{\text{Earth}} = 1.225 \frac{\text{kg}}{\text{m}^3}$ and a gravitational acceleration of $g_{\text{Earth}} = 9.81 \frac{\text{m}}{\text{s}^2}$ were considered. Instead for Mars, a density of $\rho_{\text{Mars}} = 0.015 \frac{\text{kg}}{\text{m}^3}$ and a gravitational acceleration of $g_{\text{Mars}} = 3.72 \frac{\text{m}}{\text{s}^2}$.

The density-to-gravitational acceleration ratio on Earth is close to $(\frac{\rho}{g})_{\text{Earth}} = 0.125 \ \frac{\text{kgs}^2}{\text{m}^4}$, whereas on Mars is $(\frac{\rho}{g})_{\text{Mars}} = 0.0040 \ \frac{\text{kgs}^2}{\text{m}^4}$. The ratio among those two quantity has been considered in order to understand the effects that produce on the design of a UAV for Martian flight with respect to conventional UAVs, $\frac{(\frac{\rho}{g})_{\text{Earth}}}{(\frac{\rho}{g})_{\text{Mars}}} = 30.968$. This result implicates that, for the same stalling speed and maximum lift coefficient, the Martian UAV has a wing loading roughly 31 smaller than the one of the terrestrial drone, hence it should have a wing surface 31 times greater. This may lead to several issues.

For the same example, the wing loading for the Earth and Mars case are: $(\frac{M}{S})_{\text{Earth}} = 6.2436 \ \frac{\text{kg}}{\text{m}^2}$ and $(\frac{M}{S})_{\text{Mars}} = 0.2016 \ \frac{\text{kg}}{\text{m}^2}$. The maximum take-off mass has been set equal to MTOM = 10 kg, therefore, from wing loading results, the corresponding wing surfaces are $S_{\text{Earth}} = 1.60 \text{ m}^2$ and $S_{\text{Mars}} = 49.60 \text{ m}^2$. In case that the same materials and technology were used for the wing manufacturing, wing masses would be extremely different. In order to estimate the wing masses, statistical and semi-empirical formulae reported by Sadraey [36] have been used

$$M_{\text{wing}} = \rho_{\text{mat}} \cdot K_\rho \cdot S \cdot \text{MAC} \left(\frac{t}{c}\right)_{\text{max}} \left(\frac{\text{AR } n_{\text{ult}}}{\cos(\Lambda_{c4})}\right)^{0.6} \lambda^{0.04}, \tag{2.4}$$

where ρ_{mat} is the density of the material of the wing, K_ρ is the wing density factor and depends on the aircraft category, S is the wing surface, MAC is the mean aerodynamic chord, $\left(\frac{t}{c}\right)_{\text{max}}$ is the maximum thickness-to-chord ratio of the airfoil, AR is the aspect ratio, n_{ult} is the ultimate load factor and it is defined as $n_{\text{ult}} = 1.5 n_{\text{max}}$, Λ_{c4} is the quarter chord sweep angle and λ is the taper ratio.

For this analysis, the following values have been used: $\rho_{\text{mat}} = 1800 \ \frac{\text{kg}}{\text{m}^3}$, $K_\rho = 0.0063$, $\left(\frac{t}{c}\right)_{\text{max}} = 10 \ \%$, AR = 10, $n_{\text{max}} = 2$, $\Lambda_{c4} = 0°$ and $\lambda = 0.60$.

Figure 2.11 shows the results of the sensitivity analysis on wing surface and wing mass with respect to variation in density and acceleration of gravity.

Results indicate that for the terrestrial UAV, a wing mass of $M_{\text{wing,Earth}} = 5.48$ kg can be retrieved, whereas for the Martian drone $M_{\text{wing,Mars}} = 944.57$ kg. The latter result is much greater than the maximum take-off mass of the UAV itself, MTOM = 10 kg. As a conclusion, the condition for the Mars drone is not feasible.

In order to retrieve feasible solutions for the Mars case, it is required to increase the wing

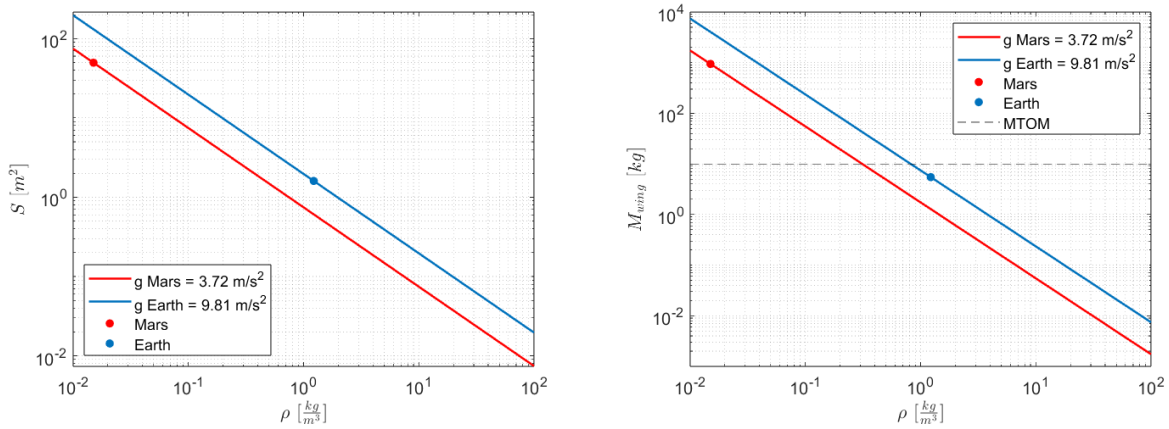

Figure 2.11: Wing surface and wing mass variation with density and acceleration of gravity

loading. The limit imposed by the stalling constraint over the wing loading is proportional to $\left(\frac{\rho}{g}\right)$, v_{stall} and $C_{L\,\max}$; $\left(\frac{\rho}{g}\right)$ is dictated by the planetary environmental conditions, the only two parameters are $C_{L\,\max}$ and v_{stall}.

A possible solution may be to make use of high lift devices. This will lead to an increase in the maximum take-off mass of the UAV, due to higher complexity. Another possibility could be to select an airfoil with very high $C_{L\,\max}$, but, as the project aims to preliminary design a UAV for the large scale exploration of Mars, to have a high lift-to-drag ratio at cruise is of paramount importance, in order to extend the mission range. Requirements of a high $C_{L\,\max}$ and high $\frac{L}{D}$ are often in conflict. Moreover, the Mars UAV will operate at low Reynolds numbers, therefore the expected aerodynamic performance will be poor, also in terms of $C_{L\,\max}$.

The most simple and most effective solution might be to accept higher stalling speed, justified by the fact that the drone must have VTOL capabilities, therefore at low speeds it will make use of the thrust vectoring system and operate in transition configuration.

2.2.3. Power requirements: vertical take-off

The sizing condition for the power loading is the one that corresponds to the sizing condition in terms of maximum shaft power to be installed on the UAV, which is represented by the vertical take-off phase The aim of the analysis is to establish the shaft power to be installed to guarantee a sufficient static thrust to perform the vertical take-off.

From Blade Element Momentum Theory (BEMT) [20], at hovering condition, the rotor hover power is equal to the sum of the induced power (energy lost in the wake, because the rotor generates thrust) with the profile power (energy lost due to section drag forces).

This approach has been used by Johnson, Withrow-Maser et al. for the conceptual design of Ingenuity, as shown by reference [21].

At hover, the vertical static thrust generated by the rotors must equilibrate the weight of the aircraft. The power required for hovering, according to BEMT is given by equation (2.5)

$$\begin{cases} P = \kappa \dfrac{T^{\frac{3}{2}}}{(2\rho A_{\text{disk}})} + N_b \dfrac{\rho}{8} C_{d,\text{mean}} A_b V_{\text{tip}}^3 \end{cases} \tag{2.5}$$

where, P is the rotor power in [W], T the rotor thrust in [N], A_{disk} the disk area in [m^2], A_b the blade area in [m^2], N_b is the number of blades, $C_{d,\text{mean}}$ is the mean drag coefficient of the blade, V_{tip} the blade tip speed in $\left[\frac{\text{m}}{\text{s}}\right]$. κ is the induced power factor defined as the ratio of the actual induced power with the ideal power, typical values are $\kappa = 1.2$ at hover, and $\kappa = 2.0$ or greater in edgewise forward flight of a rotor, such as during transition to forward flight phase for a VTOL UAV.

From this formulation, low disk loading $\left(\frac{T}{A}\right)$, meaning large diameter and high lift-to-drag ratio of the blade airfoil $\left(\frac{C_l}{C_d}\right)$ reduce the power required.

A parametric study on number of rotors N_{rotors} and disk diameter D_{disk} has been carried out in order to retrieve the minimum power required for vertical take-off. Equation (2.5) has been rearranged to take into account multiple rotors. Additional consideration about the mass of rotors and motors, number of rotors, diameter and configuration complexity will lead to a trade-off study during the design of the two UAVs. In addition, an excess of thrust will be beneficial in order to permit a fast vertical take-off with adequate vertical acceleration. To this aim, a multiplicative factor $a = 1.1$ has been used to require a vertical thrust equal to a times the weight.

Equation (2.5) has been rearranged to equation (2.6), to retrieve the power required by vertical take-off phase

$$\begin{cases} P_{\text{req,1rotor}} = \kappa \left(\frac{a \ \text{MTOM} \ g}{N_{\text{rotors}}}\right)^{\frac{3}{2}} \frac{1}{(2\rho A_{\text{disk}})} + N_b \frac{\rho}{8} C_{d,\text{mean}} A_b V_{\text{tip}}^3 \\ P_{\text{tot,req}} = N_{\text{rotors}} P_{\text{req,1rotor}} \end{cases} \tag{2.6}$$

From BEMT, the low density conditions of Mars atmosphere bring severe difficulty to perform vertical take-off, due to higher induced power. In contrast, a beneficial effect is provided by the lower gravitational acceleration.

Figure 2.12 shows the induced power at vertical take-off as function of atmospheric density ρ and gravitational acceleration g. As an example, it has been considered the case of an

UAV with MTOM = 10 kg, 4 rotors of diameter $D = 10\ in$, $a = 1.05$ for vertical take-off and an induced power factor of $\kappa = 1.2$.

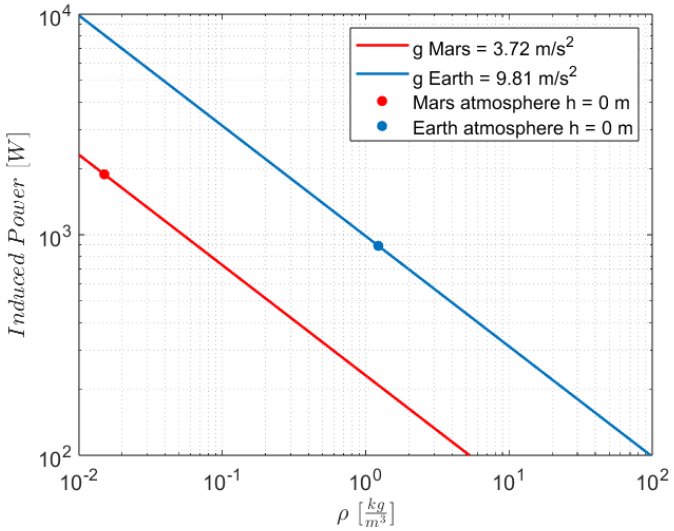

Figure 2.12: Induced power at vertical-take off as function of ρ and g

The low gravitational acceleration on Mars fosters the limitation of induced power, however the low density produces an increase of induced power component. At the atmospheric conditions of Mars surface, the effect produced by the low density is dominant with respect to the one resulting by the low acceleration of gravity. Results indicate induced power for the vertical take-off on Earth would be about $P_{\text{induced,Earth}} = 890\ W$, on Mars $P_{\text{induced,Mars}} = 1878\ W$. For this test case, the induced power on Mars is 2.11 times the induced power on Earth.

The induced power depends on the structure of the rotor wake, typically with the generation of rolled-up tip vortexes. The use of coaxial rotors may help in reducing the rotor power, due to the mutual interaction between the wake generated by the upper with the lower rotor.

This phenomenon is explained by Johnson [20], *"A rolled-up tip vortex with strong swirl velocities forms just behind the blade, and convects downward and inward due to the mutual interference with tip vortices below it. When this tip vortex encounters the following blade, it is inboard of and very close below the tip. The airloads produced by this encounter are crucial to the performance of the rotor. After encountering this blade, the vortex is convected downward at a higher rate, proportional to the mean induced velocity at the rotor disk. There is also a sheet of vorticity emanating from the inboard portion of the blade, which is rapidly convected downward".*

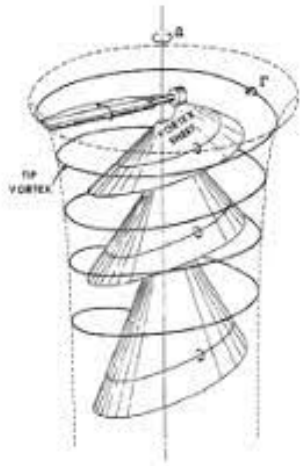

Figure 2.13: Wake structure generated by the rotor at hover

Low fidelity methods have been used for the aerodynamic simulation carried out during this thesis, therefore a simple approach excluded to take into account coaxial rotor configurations.

Considering the profile power component, the blade tip velocity V_{tip} must be limited in order to avoid large separated regions due to the presence of strong shocks. In addition, the tip velocity must be high to minimize the blade area. To this aim, a maximum Mach number at tip equal to $M_{\text{tip}} = 0.76$ has been set, similarly to what presented by Johnson, Withrow-Maser, Young et al. [21]. On Mars, the reference speed of sound at 0 m altitude is $c_{\text{Mars}} = 244.4\ \frac{\text{m}}{\text{s}}$, significantly lower than the speed of sound on Earth at 0 m $c_{\text{Earth}} = 340.3\ \frac{\text{m}}{\text{s}}$.

Mars low density conditions brings to low profile power, but at the same time the Reynolds numbers is very low , hence the $C_{d,\text{mean}}$ of the blade is higher than it is in the terrestrial case. $C_{d,\text{mean}} = 0.01$ for the Earth case and $C_{d,\text{mean}} = 0.04$ for the Mars case have been used.

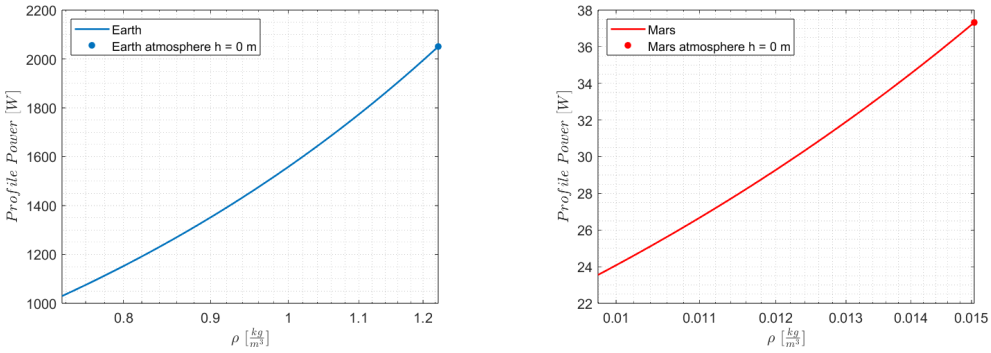

(a) On Earth (b) On Mars

Figure 2.14: Profile power variation with density

Still for the same test case of the UAV of MTOM = 10 kg, a sensitivity study has been carried out for the induced, profile and total power required at vertical take-off as function of rotor diameter and number of rotors. Results are presented hereafter.

The induced power decreases with an increase in rotor diameter D_{disk} and number of rotors N_{rotors}.

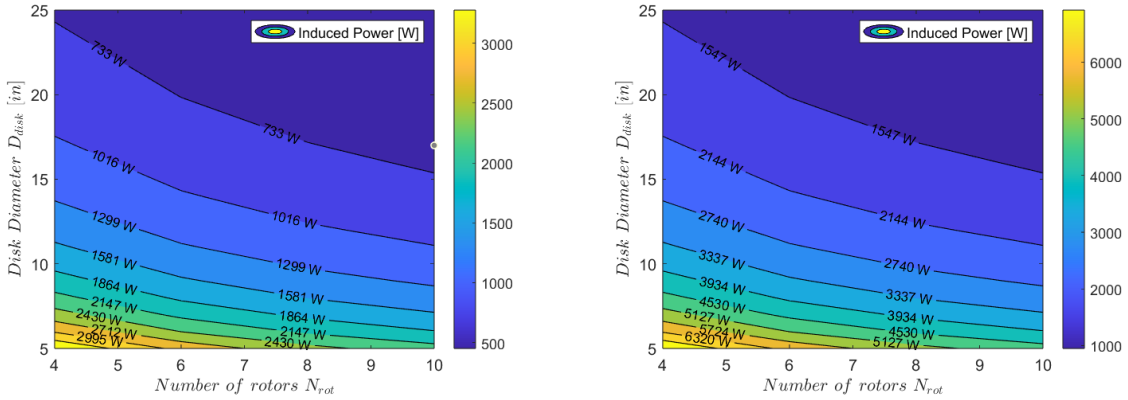

(a) Earth (b) Mars

Figure 2.15: Induced power required at vertical take-off as function of diameter and number of rotors

The induced power required for the Mars case is significantly higher than the terrestrial ones.

The profile power increases both with the number of rotors both with the diameter.

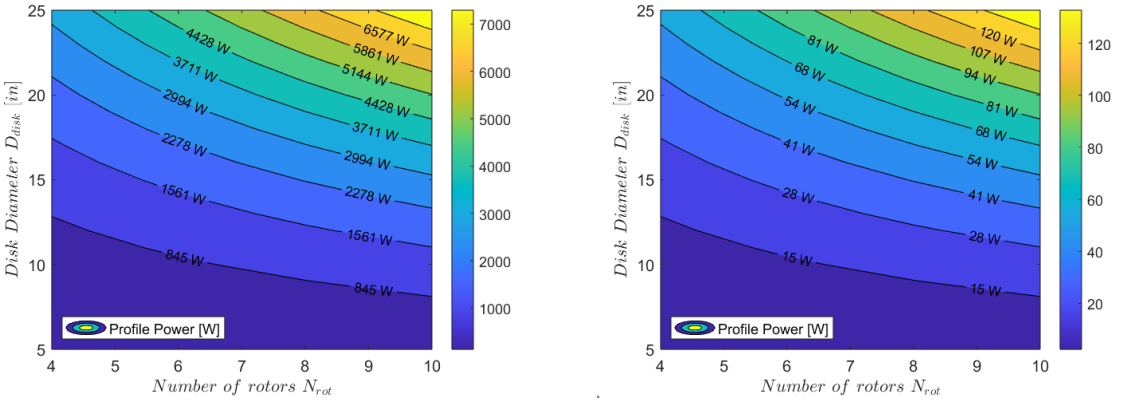

(a) Earth (b) Mars

Figure 2.16: Profile power required at vertical take-off as function of diameter and number of rotors

The profile power required for the Mars case is significantly lower than the terrestrial one.

The sum of the induced and profile power gives the total power required at vertical take-off.

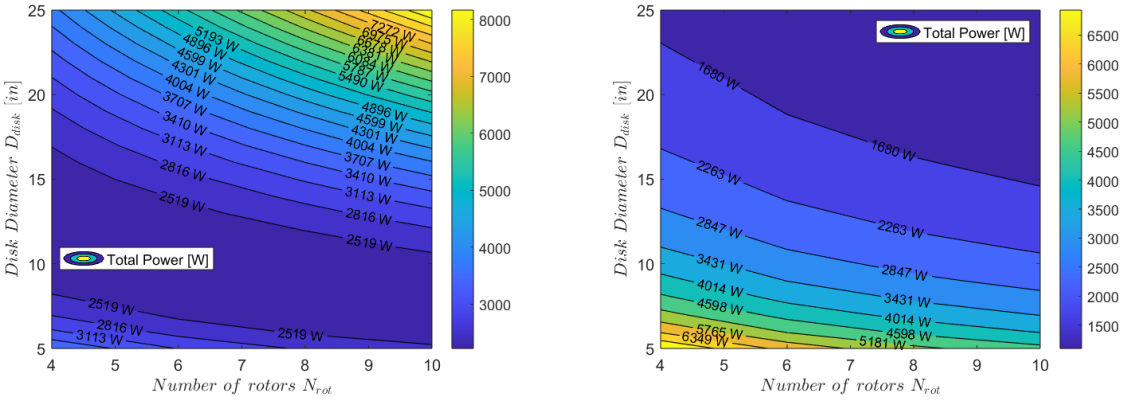

(a) Earth (b) Mars

Figure 2.17: Total Power Required at VTO as function of diameter and number of rotors

The trend of the total power required at vertical take-off as function of number of rotors and diameter is different for the terrestrial and the Martian case. On Mars, the induced power contribution is dominant, hence the total power decreases with an increase of rotor diameter and number of rotors. On Earth, the profile and induced power contributions are comparable, with opposite trends. As a result, the minimum total power is given by a

trade-off between the number of rotors and diameter. These features are visible in figure 2.18.

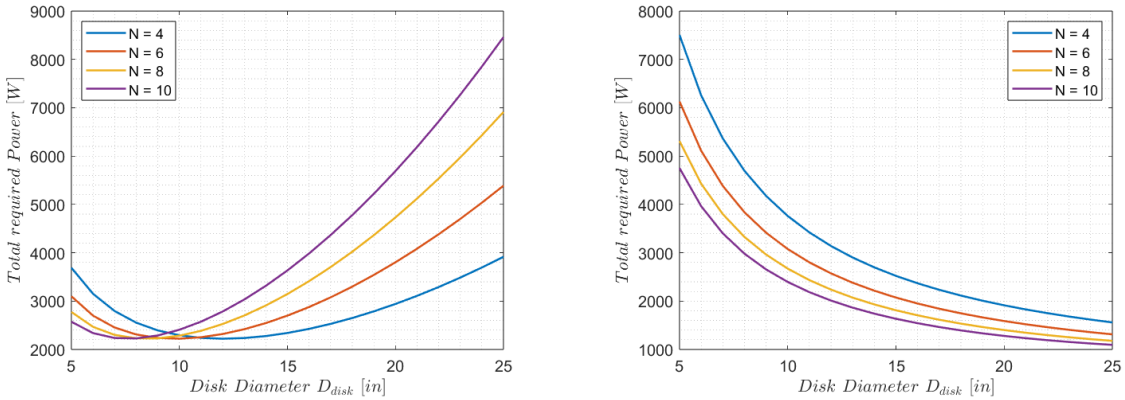

(a) On Earth

(b) On Mars

Figure 2.18: Total power required at vertical take-off as function of number of rotors and diameter

3 | Design of the Mars UAV

3.1. Pre-conceptual design

Future scientific missions on Mars will require the aerial exploration of the planet at a large scale. In order to achieve long-range capabilities, cost-effectiveness, and relatively compact dimensions, one of the most promising solutions involves the use of fixed-wing UAVs.

The extreme conditions on the surface of Mars, including glacial temperatures and very low density, necessitate the use of ultra-light materials that ensure high performance in terms of mechanical properties and resistance to very low temperatures. Furthermore, the rough terrain characteristics mandate the UAV ability to perform vertical take-off and landing. The primary and relatively abundant source of energy on Mars is provided by solar irradiance. The UAV will be equipped with solar panels to ensure self-recharging capabilities. To maximize the operational range of the UAV, state-of-the-art batteries must be utilized. A recharge time of $t_{\text{recharge}} \leq 2$ sol has been required. State-of-the-art technologies necessary for Martian flight will be discussed later in this chapter, specifically in section 3.1.2.

Furthermore, considering cost constraints during the transportation phase from Earth to Mars, it is imperative to minimize the mass of the UAV. Therefore, a constraint over the maximum take-off mass has been imposed, ensuring that MTOM ≤ 20 kg. Additionally, limitations were placed on the wingspan $b \leq 3.5$ m and fuselage length $L_{\text{fus}} \leq 4$ m due to storage considerations.

The objective is to significantly extend the cruising phase to maximize the mission range, denoted as R. The target value for the mission range has been set at $R \geq 200\ km$.

3.1.1. Draft of a scientific mission on Mars

The mission designed for the Mars UAV involves analyzing gases from the atmosphere and vaporized solid samples using a miniaturized gas chromatograph (GC) coupled with a

mass spectrometer (MS). The mass spectrometer provides information about the molecular and isotopic structure of the analysed species, thereby enhancing accuracy through the coupling of GC and MS. Through the characterization of soil samples from Martian regolith, it becomes possible to search for organic compounds and gather more information about signs of ancient life on the Red Planet.

The state-of-the art is represented by the Sample Analysis at Mars (SAM), a component of Mars Curiosity Rover. SAM is a suite of three instruments, that include a mass spectrometer, gas chromatograph, and tunable laser spectrometer, as presented by [25]. It has a mass of approximately 40 kilograms. SAM is designed to search for carbon compounds, including methane (CH_4), which are associated with life. SAM explores the processes involved in the generation and destruction of these compounds in the Martian ecosphere. Additionally, it measures the abundances of other light elements associated with life, such as hydrogen, oxygen, and nitrogen.

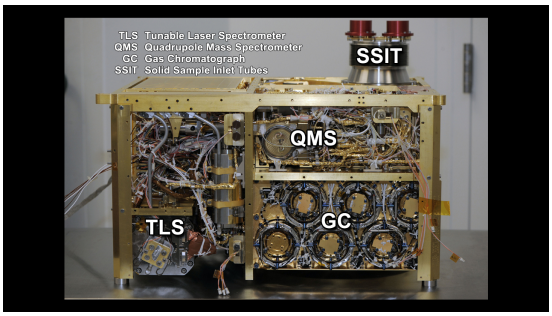

Figure 3.1: Sample Analysis at Mars (SAM)

SAM heats the soil samples and the components are vaporized and are analysed by the three instruments. The gas chromatograph separates the gases into various components for analysis. The mass spectrometer identifies elements and compounds based on their mass. The tunable laser spectrometer measures the abundance of various isotopes of carbon and oxygen in carbon dioxide and oxygen in water vapor. Additionally, it measures trace levels of methane and its carbon isotope ratio.

Recently, there has been a growing interest in advancing the miniaturization of space gas chromatographs. These efforts aim to significantly reduce both the volume and mass required by GC and MS instrumentation, approaching a reduction of close to one order of magnitude. The work by Szopa, Coscia, Cabane, and Buch [40] highlights promising results achieved with micro electro-mechanical systems (MEMS), even though their analytical performance is slightly lower compared to classical chromatography. This should not be a major concern, as the analytical targets for extreme environments are expected to be more limited.

The Mars UAV is supposed to be equipped with both a miniaturised gas chromatograph and a mass spectrometer, identified as the payload of the UAV. Assuming to make use of the next-generation of miniaturised GC and MS proposed by [40], which is projected to be operational in 5 to 10 years, the estimated payload mass has been set equal to $M_{\text{payload}} = 2.0\text{kg}$.

3.1.2. Innovative technology

Li-S and Lithium-metal batteries

For the design of an UAV for Martian atmospheric flight, it is essential to embrace a technology enabling completely autonomous recharge. Hence, the use of a full-electric propulsion system has been considered, taking advantage of the possibility to use wing-mounted solar panels. A typical electric propulsion system is composed by a battery package, inverters, electric motors, drive shafts, optional gearboxes, and propellers. Figure 3.2 shows the typical layout of the propulsive system for an electric aircraft.

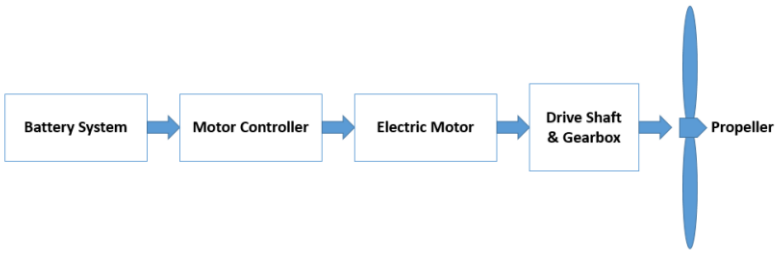

Figure 3.2: Layout of a full-electric propulsive system

Battery cells are mainly characterised by two parameters: specific energy e^*_{spec} and specific power p^*_{spec}. Aeronautical applications are very demanding in both terms, but differently with respect to the specific phase of the flight profile. In fact, during vertical take-off, the propulsive system is required to supply the maximum power, so high power density cells are preferred in order to minimise the mass of the battery package. Nevertheless, in order to extend the mission range as much as possible, it is necessary to perform a long cruise phase, which typically requires moderate shaft power for a long time. Hence, opting for high energy density cells is the optimal choice to achieve a battery package with significant capacity and moderate mass.

Due to the low density of the Martian atmosphere ($\rho_{1000\text{ m}} = 0.0138\ \frac{\text{kg}}{\text{m}^3}$, at 1000 m altitude), drag force D will assume moderate values, resulting in a correspondingly moderate required power $P_r = Dv$. However, the UAV will operate in the low Reynolds regime,

leading to higher-than-common values for the drag coefficient C_D.

Battery packages consist of a collection of cells arranged in series and in parallel. When two equal cells are disposed in series, the result is a doubling of the voltage of the battery package, but not its capacity. Conversely, when two cells are connected in parallel, the effect is a doubling of the capacity without a change in the overall voltage. The current state-of-the-art cells with regard to specific power are of the lithium-polymer type (Li-Po), with values in the order of $p^* = 8000\ \frac{W}{\text{kg}}$. However, Li-Po cells are characterised by moderate energy densities, approximately $e^* = 160\ \frac{\text{Wh}}{\text{kg}}$. These cells are widely used in MINI UAVs and quadcopters. On the other hand, lithium-ion cells (Li-Ion) are the preferred choice in terms of specific energy, with values around $e^* = 250\frac{\text{Wh}}{\text{kg}}$, even though they exhibit moderate power densities (about $p^* = 750\frac{W}{\text{kg}}$). Other key drivers with regard to the battery performance and the possible applications, are the variation of performance with number of life-cycles and the effects of temperature.

Figure 3.3 shows the current landscape of battery technology types, in terms of energy density and specific energy.

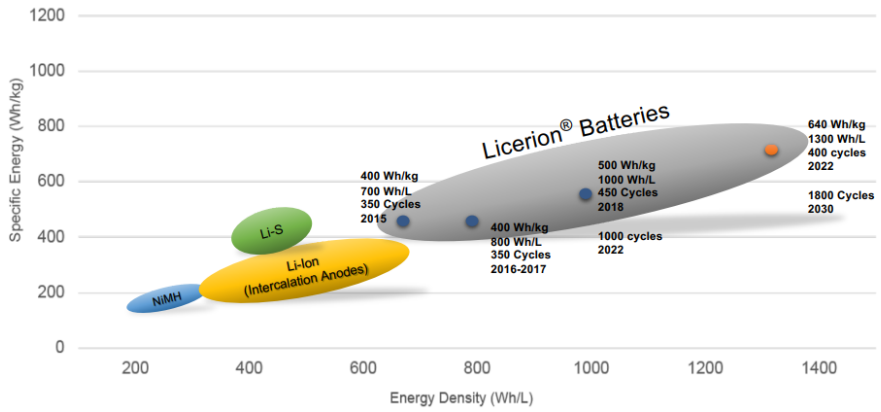

Figure 3.3: Performance of state-of-the art batteries and future developments

New generation batteries are characterised by lithium-sulfur technology (Li-S). Some prototypes are already available but this kind of cell is not ready for the use at large scale, both in terms of performance (NASA is conducting several projects on Li-S batteries and significant improvement in specific energy are predicted), but also with regard to the number of cycles that can be sustained by the battery before degradation of its characteristics, which is in the order of 100 cycles. NASA states, in reference [11], that a model developed by Oxis Energy with initial specific energy of $e^* = 300\frac{\text{Wh}}{\text{kg}}$, after 100 cycles the specific energy was reduced to $e^* = 170\frac{\text{Wh}}{\text{kg}}$. Several studies attest that in 5 to 10 years Li-S cells will overcome the presented issues and will be ready for an extensive use on the

market.

Another promising battery technology is the one offered by Licerion batteries produced by Sion Power Corporation. Licerion is a Lithium-Metal Oxide Rechargeable Battery. This technology presents enhanced performance in terms of both specific energy and specific power, outperforming Li-Ion technology. Those kind of batteries are also able to sustain a much higher number of cycles before degradation of cell capacity and specific energy, when compared to Li-S cells. Licerion cells are probably the most suitable for the design of Mars UAV, because of their combination of high specific energy and high specific power.

Possible applications of Licerion batteries and performance and degradation data from 2018 and 2020 NASA Aerospace Battery Workshop, reference[29] and [30], are presented in figure 3.4 :

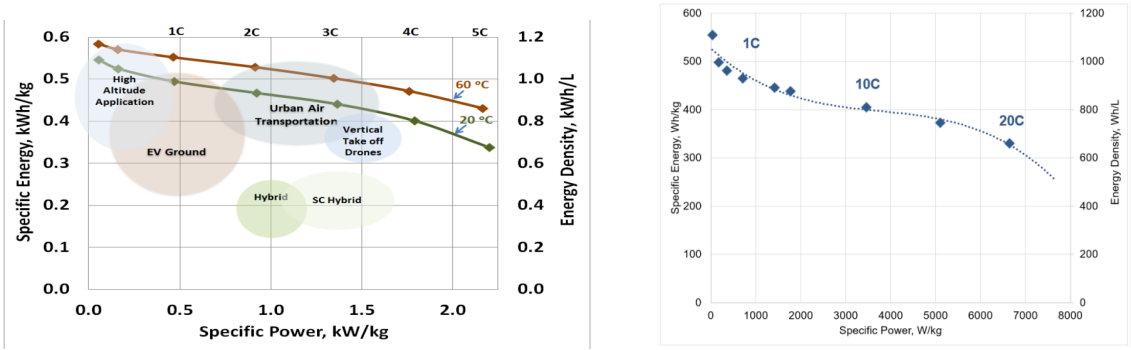

(a) Possible applications (b) Effects of C_{rate}

Figure 3.4: Licerion batteries: Applications and performance

With regards to low-temperature effects, a 4C discharge at $T = -25°C$ and a 1C discharge at $T = -40°C$ exhibited 70% of retained capacity, as shown by figure 3.5.

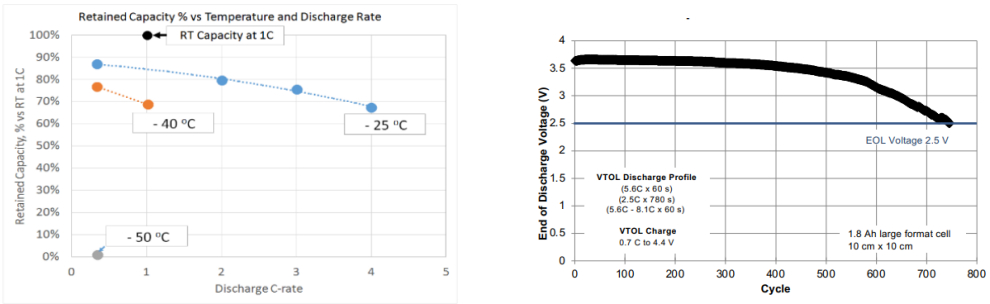

(a) Effects of temperature (b) Effects of cycles

Figure 3.5: Licerion batteries: Performance degradation

For the design of the Mars UAV, Lithium-Metal Oxide have been considered, in particular, an hypothetical cell similar to the ones developed by Licerion has been selected, with the following characteristics:

Parameter	Value
Specific energy	$e^* = 450\ \frac{\text{Wh}}{\text{kg}}$
Specific power	$p^* = 1000\ \frac{W}{\text{kg}}$
Nominal capacity	$Q_{\text{nom}} = 17.5$ Ah
max C rate	$\max C_{\text{rate}} = 1$
max C rate T-O	$\max C_{\text{rateTO}} = 3$
SOC min	$SOC_{\text{min}} = 10$ %

Table 3.1: Mars UAV: battery specifications

Parameter	Value
Nominal Voltage	$V_{\text{nom}} = 3.83$ V
Ideal Voltage	$V_0 = 4.3$ V
Internal resistivity	$R_I = 0.001\ \Omega$
SOC Voltage decreasing rate	$V_{\text{SOC}} = 0.7$ V
Cell mass	$M_{\text{cell}} = 0.166$ kg
Cell weight factor	$\omega_f = 0.85$

Table 3.2: Mars UAV: battery specifications

These types of batteries are expected to undergo more than 500 cycles with minimal performance degradation. The characterisation of cell performance and the sizing of the propulsive system of the UAV has been conducted making reference to [52].

C_{rate} serves as an indicator of how quickly the battery can be discharged, with a higher C rate corresponding to a higher maximum current output. In this work, $\max C_{\text{rate}}$ is meant as the maximum continuous C rate, $\max C_{\text{rateTO}}$ is meant as the maximum C rate that can be achieved for a limited period of time (usually 60-90 seconds). A weight factor ω_f has been used for the sizing of the battery package, it accounts for the increase in mass due to the auxiliary components, such as structures, electrical connections, the battery management system (BMS), and battery cooling system.

The battery voltage decreases with the discharged capacity and it is influenced by the required current. The cell voltage can be approximated by means of a linearization:

$$V = f(\text{SOC}, I) = V_0 - (1 - \text{SOC}) \cdot V_{\text{SOC}} - R_I \cdot I, \tag{3.1}$$

where V_0 is the ideal voltage of the cell, when the state of charge (SOC) is equal to 100 % and zero current is required; V_{SOC} represents the state of charge voltage decreasing rate, serving as a sort of resistance that takes into account the decrease in cell voltage with the discharged capacity; and R_I is the internal resistivity which represents the fact that the cell voltage decreases if the discharge current increases.

V_0, V_{SOC}, R_I were chosen based on a review of the data provided in [30] for high power Licerion batteries. The comparison is illustrated in figure 3.6.

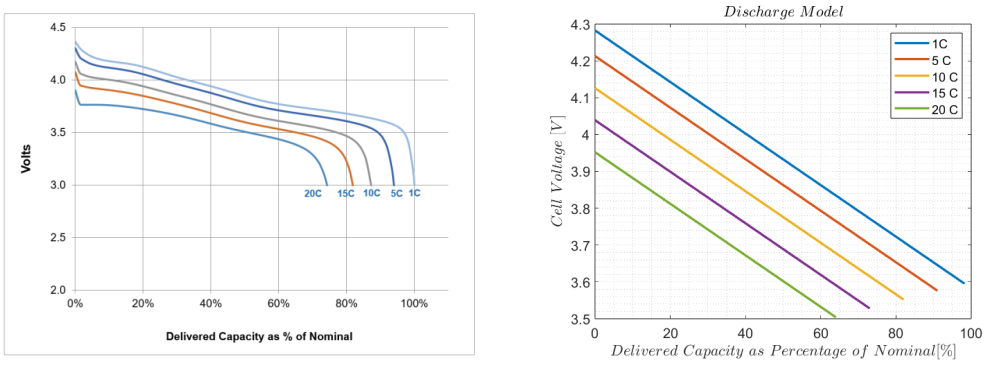

(a) Discharge data (b) Discharge model

Figure 3.6: Comparison between battery discharge data and linearised model

This model has been implemented in MATLAB. Later, an energetic analysis has been carried out in order to size the battery pack in accordance with multiple constraints concerning all flight phases. Batteries are supposed to operate always at $T \geq -25°C$, otherwise a heater must activate.

Solar Panels

In designing the Mars UAV, batteries are recharged by the effect of the solar energy, the sizing of the solar panel system and its performance are subjects of discussion. Flexible solar panels represent the state-of-the art. This kind of panels can be mounted on the top of the wing surface, or on other surfaces where the curvature is moderate. For this work, CTJ30 model has been taken as reference. CTJ30 is a Triple-Junction Solar Cell for Space Applications developed by CESI. Data are reported in reference [43].

CTJ30 solar cell is composed by multiple layers made of Indium-Gallium-Phosphorus (InGaP), Gallium-Arsenic (GaAs), and Germanium (Ge). It is indicated as InGaP/GaAs/Ge. The solar cell is characterised by an extremely low thickness, between $t = 80 \pm 20$ μm, high radiation resistance, and thermal degradation below 1%. The cell size is of $S_{\text{cell}} = 26.5$ $c\text{m}^2$ and it has a declared efficiency of $\eta = 29.5$ % at $G = 1367$ $\frac{\text{W}}{\text{m}^2}$ and $T = 25°\text{C}$. CTJ30 is also characterised by a very low areal density $\left(\rho_{\text{areal}} = 500 \ \frac{g}{\text{m}^2}\right)$.

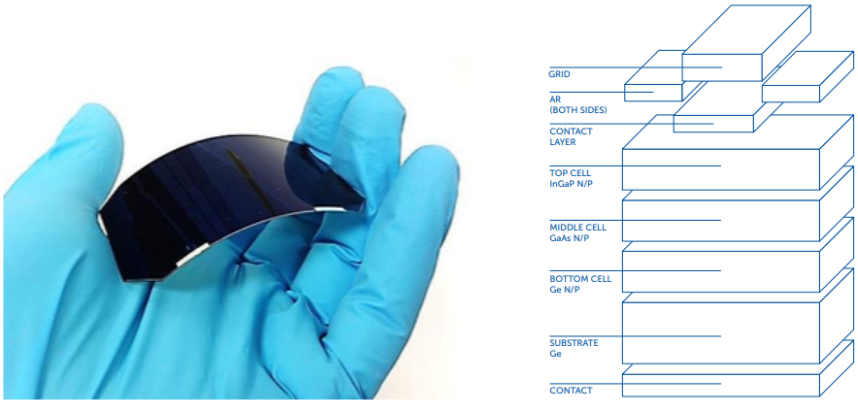

(a) CTJ30 THIN flexibility (b) CTJ30 THIN layers composition

Figure 3.7: Thin Triple-Junction solar cell

Solar irradiance under Martian amtospheric conditions has been presented in section 1.1.3. That model has been implemented using MATLAB.

The reference landing site chosen for the computation of solar irradiance and solar cell performance is the location of Viking 1, situated at coordinates $22.30°N$, $47.90°W$, with an altitude very close to $h = 0\ m$. From equation 1.2, the heliocentric distance at the landing site, when the areocentric longitude is equal to $L_S = 120°$, is equal to $r = 1.5706$ AU. Opacity assumes the value of $\tau = 0.4$ (as illustrated by reference [6]), in case of absence of dust storms. The sunset hour angle is provided by equation 1.14, and it is equal to 99 °. The sunrise hour angle is the opposite of the sunset hour angle.

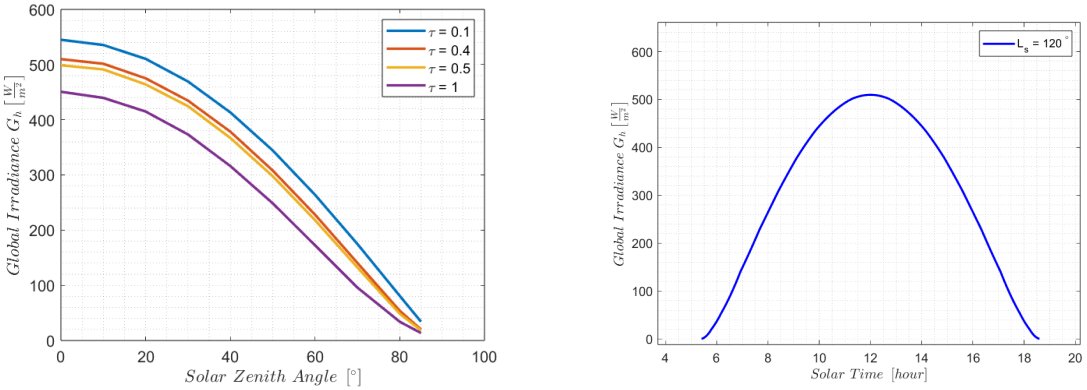

(a) Global irradiance variation with zenith angle (b) Global irradiance variation with solar time

Figure 3.8: Global irradiance on a horizontal surface at reference landing site

By integrating the global irradiance on a horizontal surface across solar time, it is possible to compute the energy irradiated during a day on a surface of 1 m^2, defined as E^*_{daily}, in $\left[\frac{\text{Wh}}{m^2}\right]$. At the presented reference conditions, $E^*_{daily} = 4012.3\ \frac{\text{Wh}}{m^2}$.

The solar panels are sized using a set of thin, flexible cells to ensure a recharge time for the Mars UAV that is below the maximum recharge time of 2 sols. Assuming a cell efficiency of $\eta = 20\ \%$ due to the low Martian temperature, each squared metres of solar panels can collect daily $E^*_{daily} = 802\ \frac{\text{Wh}}{m^2}$ of energy.

In the preliminary design phase of the Mars UAV, an energy analysis over the flight profile will be conducted. This involves computing the total energy required for the mission. Subsequently, it can be verified whether the installed solar panels can ensure a recharge time lower than the maximum recharge time of 2 sols.

Materials

As discussed in section 2.2, the wing loading of the UAV takes on significantly lower values than those typical for terrestrial applications due to the rarefied Martian atmosphere. Consequently, the wing surface, along with all other aerodynamic surfaces, will be large. To minimize the MTOM of the UAV, it is crucial to utilize ultra-light materials with high-performance mechanical properties. Another critical consideration is the resistance to the glacial temperatures characteristic of the Martian surface.

To ensure satisfactory mechanical properties and light-weight, the use of carbon fiber reinforced material has been considered. State-of-the art of fabrics for extreme environments is represented by a special version of fabric developed by TeXtreme Composite Materials for the design of Ingenuity's rotor blades. No specific datasheet is available, but it has been referred that the fabric has areal density around $\rho_{\text{areal},f} = 40 - 60\ \frac{g}{m^2}$. Conventional pre-pregs typically have areal densities between $\rho_{\text{areal},f} = 160 - 240 \frac{g}{m^2}$ and thicknesses that vary in the range $t_f = 0.2 - 0.4mm$. Fabrics do not include the resin content, that generally is in range 40% - 50%, depending on the desired mechanical properties. Epoxy is characterised by a density of about $\rho_m = 1000 - 1200 \frac{\text{kg}}{m^3}$.

In designing the Mars UAV, a special fabric with an areal density of $\rho_{\text{areal},f} = 60 \frac{g}{m^2}$ and a fabric thickness of $t_f = 0.225\ mm$ has been considered. Additionally, a 40 % epoxy resin content has been assumed, characterized by a density of $\rho_m = 1000 \frac{\text{kg}}{m^3}$. Consequently, the composite material is characterised by a density of $\rho = 1063 \frac{\text{kg}}{m^3}$. If a traditional fabric type was considered, with $\rho_{\text{areal},f} = 180 \frac{g}{m^2}$, the carbon fiber reinforced material would have been characterised by a density value of about $\rho = 1596 \frac{\text{kg}}{m^3}$.

The material density is necessary for the aircraft design tool to make an initial estimation of the main components of the UAV. Masses of the wing, horizontal tail, vertical tail, and fuselage have been estimated using semi-empirical formulas found in Sadraey's book [36].

Subsequently, after sizing the preliminary geometry of the UAV, a more detailed model was created using OpenVSP [28]. Material properties were assigned, taking into account the areal density of the ultra-thin carbon fiber-reinforced material. It was assumed that two plies of this material would be used for the skin of the aerodynamic surfaces and the fuselage. Ribs and spars were also considered, with the assumption that they would be formed by a honeycomb structure.

Ingenuity employs a combination of Kapton polyimide thin-film heaters and a metallised Kapton insulation layer. This combination is designed to maximize the absorption of solar heat while simultaneously minimizing heat loss from inside the box to the Martian atmosphere. These materials serve to protect the on-board electronics and instrumentation. The ultra-thin metallised layer can operate over a wide temperature range, from -250 °C to 290 °C.

(a) Textreme fabric for blades (b) Kapton insulation material

Figure 3.9: Advanced materials for extreme applications

3.1.3. Initial requirements

The project proposes the design of a UAV capable of large-scale operations in the Martian environment. Its primary objective is to analyze both the atmosphere and soil samples, utilizing a gas chromatograph and mass spectrometer. These instruments constitute the payload of the UAV. To enhance the large-scale operability of the UAV, the objective is to maximise the mission range, that must be at least of $R \geq 200\ km$.

Further considerations are essential due to the unique operational conditions, including factors like the propulsion system type and self-charging capability of the UAV. Additionally, economic and storage constraints, that involve the maximum wingspan, maximum

fuselage length, and maximum take-off mass, must be taken into account.

Table 3.3 contains the initial requirements for the design of the Mars UAV.

Characteristics	Requirements
Payload Mass	$M_{\text{payload}} = 2.0$ kg
Mission Range	$R \geq 200\ km$
Maximum Take-Off Mass	MTOM ≤ 20 kg
Fuselage Maximum Length	$L_{\text{fus}} \leq 4.0$ m
Maximum Wingspan	$b \leq 3.5$ m
Propulsive system	Electric
Recharge time	$t_{\text{recharge}} \leq 2$ sols

Table 3.3: Initial requirements

3.1.4. Baseline mission profile

In addition to the initial requirements, a baseline mission profile has been drafted. The mission profile is formed by the following flight phases: Vertical Take-Off, Transition to forward flight, Climb, Cruise, Descent, Transition to vertical flight, and Vertical-Landing.

Figure 3.10 illustrates the layout of the mission profile.

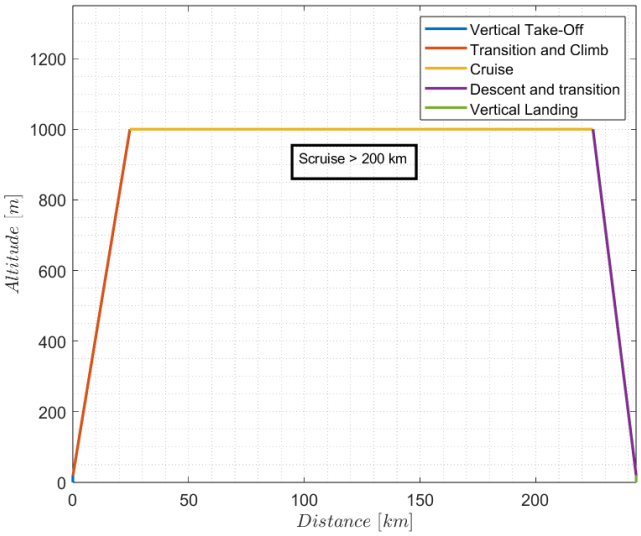

Figure 3.10: Baseline mission profile

Because the UAV does not fall under any specific category, common regulatory frameworks such as FAR 23 or CS-23 could not be applied. Consequently, the requirements on

performance and target aerodynamic coefficients have been determined through trade-off studies. Additionally, loiter and diversion are not mandated by this flight profile.

Each phase of the flight profile is briefly described.

1. Vertical Take-Off (VTO): The maximum shaft power is deployed in order to perform vertical take off. The estimated time for this phase around 10 seconds. The propulsive system is able to guarantee the maximum power for at least 30 seconds during this phase, in case of emergencies.
2. Transition from VTO to Climb: Making use of the thrust vectoring system, the propellers rotate progressively from the vertical configuration to the forward flight configuration, as the speed of the UAV increases.
3. Climb: A minimum rate of climb of 25 $\frac{\mathrm{m}}{\mathrm{s}}$ is required to guarantee satisfactory climb performance.
4. Cruise: A minimum cruising speed of 90 $\frac{\mathrm{m}}{\mathrm{s}}$ at the design cruising altitude (set to $h_{\mathrm{cruise}} = 1000$ m) has been imposed. or the cruising distance has been defined as $S_{\mathrm{cruise}} \geq 200\ km$. Since the cruising phase is expected to cover more than 80 % of the flight time, cruising performance have been later analysed in order extend as maximum as possible the mission range.
5. Descent: No particular constraints were set for descent phase, but a parametric study on shaft power and trajectory has been carried out.
6. Transition from Descent to VLND: Making use of the thrust vectoring system, the propellers rotate progressively from the forward flight configuration to the vertical configuration, as the speed of the UAV decreases.
7. Vertical Landing (VLND): The estimated time for vertical landing is 20 seconds. Similarly for take-off, the propulsive system is sized such that it is able to deploy the maximum power for at least 30 seconds, in case some emergency occurs.

All velocities are reported as true airspeeds (TAS).

3.1.5. Performance requirements

In order to design an UAV with satisfactory performance characteristics, some requirements have been established. The required performance are illustrated by table 3.4.

Mission Phase	Parameter	Configuration	Value
Vertical Take-Off	Vertical velocity ($V_{v\ \mathrm{TO}}$)	Vertical thrust	$V_{v\ \mathrm{TO}} \geq 1\frac{\mathrm{m}}{\mathrm{s}}$
Climb	Rate of Climb (RC *or* V_v)	Clean	$V_v \geq 25\frac{\mathrm{m}}{\mathrm{s}}$
Climb	Climb angle (CGR *or* γ)	Clean	$\gamma_{\max} \geq 14°$
Cruise	Cruising speed (V_{cruise})	Clean	$V_{\mathrm{cruise}} \geq 90\frac{\mathrm{m}}{\mathrm{s}}$
Cruise	High speed cruise ($V_{\max}$)	Clean	$V_{\max} \geq 160\frac{\mathrm{m}}{\mathrm{s}}$
Transition	Stalling speed (V_{stall})	Clean	$V_{\mathrm{stall}} \leq 75\frac{\mathrm{m}}{\mathrm{s}}$
Maneuver	Maximum load factor ($n_{\max}$)	Clean	$n_{\max} = 1.4$
Service ceiling	Altitude (h_{ceiling})	Clean	$h_{\mathrm{ceiling}} \geq 3000\mathrm{m}$

Table 3.4: Required performance

Two remarkable aspects are evident. First, the stalling and cruising speeds are higher than usual for terrestrial small UAVs. This is attributed to the low density of the Martian atmosphere, necessitating the generation of sufficient lift with a limited wing surface. Second, there is a notably low value for the maximum load factor (typical values are $n \geq 2.5$), in order to keep the wing loading at sufficiently high values. $n = 1.4$ corresponds to a coordinated turn with bank angle $\phi = 44.4°$, considered as satisfactory for that extreme environment.

3.1.6. Required aerodynamic coefficients

Along with the definition of the performance requirements, the aerodynamic characteristics of the drone have been evaluated, considering them as minimum values to be ensured. The following table 3.5 illustrates the required aerodynamic performance. All coefficients that are reported by the table are intended as the aerodynamic coefficients of the complete aircraft.

Mission Phase	Parameter	Configuration	Value
Transition to climb	$C_{L\,\max}$	Clean	0.8
Cruise	$C_L\ target$	Clean	0.35-0.55
Cruise	$E = \frac{L}{D}$	Clean	10
Fastest climb	$F_{\max}$	Clean	7
Descent to transition	$C_{L\,\max}$	Clean	0.8

Table 3.5: Target aerodynamic coefficients

Where $F_{\max}$ is the maximum power index F, defined as $F = E\sqrt{C_L}$.

3.2. Conceptual design

The objective of the conceptual design phase is to evaluate the technical feasibility of the Mars UAV, compare different configurations, and select the most promising one for more in-depth investigations.

In this phase, a sizing matrix plot (SMP) has been drafted. SMP is a graph reporting all the principal constraints for each flight phase of the mission. It embeds requirements on performance and aerodynamics. The objective is to find the optimal combination of power loading $\left(\frac{W}{P_b}\right)$ and wing loading $\left(\frac{W}{S}\right)$, ensuring some safety margin with respect to limits imposed by the constraints.

Subsequently, a concept of the Mars UAV has been designed.

3.2.1. Sizing Matrix Plot

The aircraft design process was carried out using ad-hoc MATLAB codes.

The maximum take-off mass of the Martian drone was set equal to MTOM = 20 kg, a choice related to mission and payload requirements, along with economical and storage considerations.

The sizing matrix plot (SMP) reports constraints for vertical take-off, vertical landing, stall, maneuver, rate of climb, rate of climb gradient, high speed cruise, service ceiling. Subsequently, the optimal wing loading and power loading were calculated.

At this early stage few information are available, therefore the aerodynamics of the complete UAV has been estimated by means of a parabolic polar ($C_D = C_{D0} + kC_L^2$), where C_{D0} is the zero-lift drag coefficient and k is defined as $k = \frac{1}{\pi\lambda e}$, related to the aspect ratio λ, or AR and the Oswald factor e. At the initial iteration, C_{D0} and e have been estimated with a statistical approach, according to the formulation present in Roskam book [34]. However, as these empirical formulas are not suitable for small UAVs, the build-up drag method was subsequently employed for estimating the UAV polar after the preliminary geometry was defined.

In order to draft the parabolic polar of the aircraft, some geometric characteristics of the wing and fuselage have been assumed. The wingspan b and the aspect ratio of the wing λ have been guessed, and C_{D0} and k have been computed. Since the MTOM has been set equal to 20 kilograms, the SMP provided as output the wing loading as well as the wing surface S. Subsequently, the aspect ratio was updated and the SMP script was repeated up to reach convergence on aspect ratio. Typically, various aircraft polars must

be taken into account, depending on the configuration (clean, take-off, landing). However, given the Vertical Take-Off and Landing (VTOL) characteristics of the UAV, it has been decided not to employ high-lift devices. This decision aims to minimize manufacturing complexity. Consequently, only one polar, corresponding to the clean configuration, has been considered.

The constraint associated to vertical take-off has been analysed according to the procedure presented in section 2.2. Trade-off studies have indicated that employing six propellers with a diameter of 20 inches is recommended.

From SMP, wing loading $\left(\frac{W}{S}\right)$ and power loading $\left(\frac{W}{P_b}\right)$ have been computed, and being the MTOM initially set to 20 kg, the wing surface was retrieved. The sizing matrix plot is illustrated by figure 3.11.

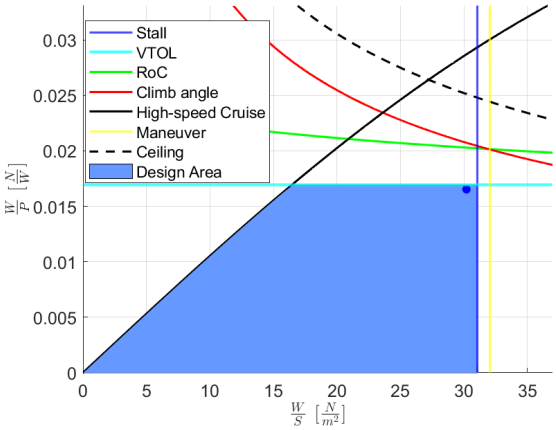

Figure 3.11: Sizing Matrix Plot

The results of the sizing matrix plot are: Wing loading $\frac{W}{S} = 29.2\ \frac{\mathrm{N}}{\mathrm{m}^2}$, power loading $\frac{W}{P_b} = 0.0165\ \frac{\mathrm{N}}{\mathrm{W}}$.

3.2.2. Concept

Different concepts have been evaluated, but the one illustrated hereafter has been considered as the most promising. A traditional tail configuration was selected to ease controllability and decouple longitudinal and lateral-directional dynamics in further studies.

Six tilt-rotors enhance vertical take-off and landing capabilities of the UAV. The sweep angle will be set in order to permit the alignment of rotors with the center of gravity during vertical take-off in order to avoid an undesired pitching moment.

The payload should be positioned as far forward as possible to enable the instrumentation

to operate under undisturbed conditions. The landing gear consists of a simple skid, located in proximity to the centre of gravity. Mid-wing configuration has been selected.

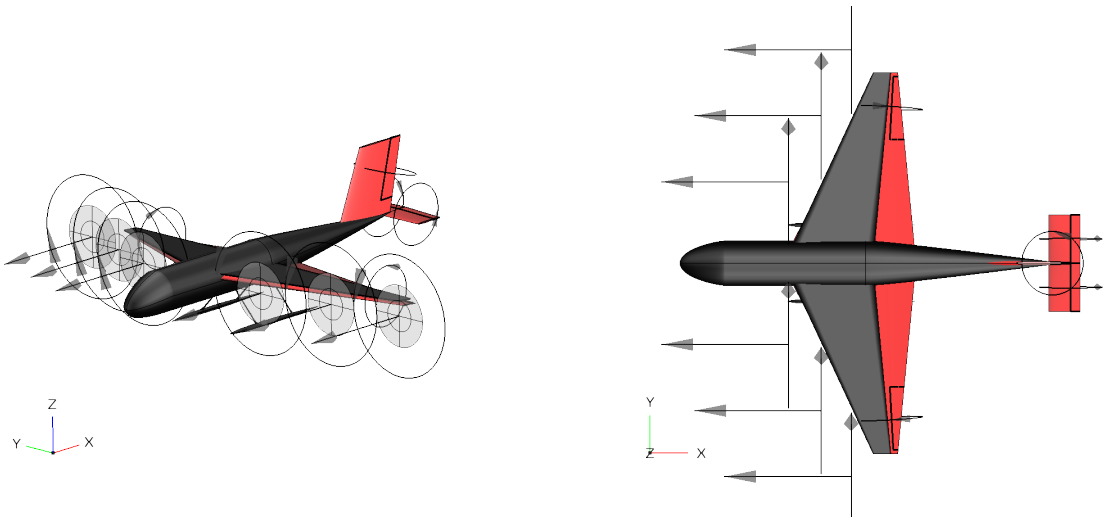

(a) Front-left view (b) Top view

Figure 3.12: Concept of the Mars UAV

The concept has been sketched on open source software *OpenVSP*.

3.3. Preliminary design

The preliminary design has been carried out in MATLAB, developing ad-hoc codes. The MTOM has been set to MTOM = 20 kg. The goal is to maximize the mission range. To this aim, particular emphasis has been posed for cruise condition, referring to equation (2.2) presented in section 2.2. The cruising speed must be determined to enable the cruise to be conducted at the maximum lift-to-drag ratio. This value can be retrieved by the polar of the complete aircraft.

To enhance the mission range, the ratio between the mass of the battery and the MTOM must be maximised. Due to the fact that the MTOM is set equal to MTOM = 20 kg, it is necessary to minimise the mass of all components apart from the battery, and of course, the payload which is kept constant to $M_{\text{payload}} = 2.0$ kg. An optimisation problem has been set up in MATLAB, after the selection of an objective function to be minimised, which has been defined as the opposite of the mission range $f_{obj} = -R$.

Few design variables have been defined, the ones evaluated as the most significant for the overall design, in order to limit the computational time. Table 3.6 shows the design

variables that have been chosen.

Design Variable	Symbol
Wingspan	b
Wing taper ratio	λ
Horizontal tail wingspan	b^{ht}
Horizontal tail volume coefficient	V^{ht}
Horizontal tail arm	L^{ht}
Vertical tail wingspan	b^{vt}
Vertical tail volume coefficient	V^{vt}
Vertical tail arm	L^{vt}

Table 3.6: Design variables

Prior to initiating the optimization tool, the results from SMP ($\frac{W}{S}$, $\frac{W}{P_b}$) were employed to determine the wing surface (S) and the maximum shaft power installed (P_b). As a result, the maximum take-off mass is equal to MTOM = 20 kg, the wing surface is $S = 2.53$ m^2, and maximum shaft power installed is equal to $P_b = 4.5$ kW.

At each iteration the design tool:

1. Builds the geometry of the wing, horizontal and vertical tail;
2. Adapts the fuselage;
3. Performs an estimation of the masses of the wing M_{wing}, horizontal tail M_{ht}, vertical tail M_{vt}, and fuselage M_{fus};
4. Retrieves the battery mass $M_{\text{battery}} = \text{MTOM} - \sum_{i=1}^{N_{\text{components}}} M_i$;
5. Computes the (nominal) total energy that can be stored by the battery package;
6. Drafts the polar of the aircraft and retrieves the condition of maximum lift-to-drag ratio E_{max}, hence the cruising speed v_{cruise};
7. Computes the energy that can be used during the cruising phase and the power required at the battery during cruise: $P_{\text{battery,cruise}} = \frac{1}{\eta_p \eta_{tr} \eta_m} \frac{1}{2} \rho_{\text{cruise}} v_{\text{cruise}}^3 S C_D$;
8. Determines the cruising time and cruising distance;
9. Evaluates the longitudinal and lateral-directional static stability;
10. Performs checks on stability requirements and if the cruising distance is higher than the minimum distance required

11. Computes the objective function $f_{obj} = -R$

M_i are the masses of all components that are important for the determination of the mass of the UAV, apart from the battery package. It will be explained in detail later in section 3.3.1.

Some constraints have been applied to the design variables:

Constraints
$1.5 \leq b \leq 3.5$ m
$0.4 \leq \lambda \leq 1.0$
$0.5 \leq b^{\text{ht}} \leq 1.5$ m
$0.2 \leq V^{\text{ht}} \leq 0.8$
$1.5 \leq L^{\text{ht}} \leq 3.0$m
$0.5 \leq b^{\text{ht}} \leq 1.5$ m
$0.02 \leq V^{\text{vt}} \leq 0.2$
$1.5 \leq L^{\text{vt}} \leq 3.0$ m

Table 3.7: Constraints on the design variables

The optimisation loop breaks if the objective function decreases with a step tolerance lower than 10^{-6} or when the program reaches the maximum number of iterations, which has been set to $iter_{max} = 200$. SQP algorithm has been used.

Result indicate that the best solution is an UAV with wingspan $b = 3\ m$, and a wing mean aerodynamic chord MAC = 0.85 m. A cruising speed $v_{\text{cruise}} = 92\ \frac{\text{m}}{\text{s}}$ at $h_{\text{cruise}} = 1000$ m has been retrieved, which corresponds to a Reynolds number of about $Re = 92\ 000$ and a Mach number of $Ma = 0.38$ at Martian atmospheric conditions.

3.3.1. Mass breakdown

The mass of the battery package has been estimated as the difference between the maximum take-off mass, the payload and all major contributors to the mass of the UAV.

Masses of wing, horizontal tail, vertical tail, and fuselage have been estimated in MATLAB, exploiting the semi-empirical formulae proposed by Sadraey [36]. These depend on the density of the material (ρ_{mat}), which is considered to be the Ultra Thin carbon fiber composite material described in section 3.1.2, for the aerodynamic surfaces and the fuselage. In addition, Sadraey's formulation requires to establish the value of a statistical parameter (K_ρ), which depends on the manufacturing technology and the aircraft cate-

gory. The categories available on Sadraey book are not applicable for the unconventional application presented by this thesis. Therefore, some assumptions on the manufacturing process have been made, and some tests have been carried out on OpenVSP, using the structural section of the software, to estimate the mass of some test geometries in order to retrieve the values of the empirical coefficients to be used in the simple formulation implemented in MATLAB.

The skin of the aerodynamic surfaces is supposed to be made of two plies of carbon fiber composite disposed with a $\pm 45°$ orientation to sustain properly bending and torsion. Ribs and spars, made of a honeycomb structure, have been considered in order to sustain loads and preserve the aerodynamic shape. Two spars placed at a quarter chord and at three quarter chord have been considered. For the fuselage, the skin has been supposed to be identical to the one for the aerodynamic surfaces. In addition, formers and stringers have been used. The fuselage also includes the internal structure for the housing of the payload, avionics, electronics, battery package. The internal structure is supposed to be made of honeycomb, with a thickness of $t = 0.5\ cm$.

The set of equations 3.2 show the expressions of Sadraey's book for the estimation of the mass of the wing, horizontal and vertical tails and fuselage.

$$\begin{cases} M_{\text{wing}} = \rho_{\text{mat}} \cdot K_\rho \cdot S \cdot \text{MAC} \left(\frac{t}{c}\right)_{max} \left(\frac{\text{AR} n_{ult}}{cos(\Lambda_{c4})}\right)^{0.6} \lambda^{0.04} \\ M_{\text{ht}} = \rho_{\text{mat}} \cdot K_\rho \cdot S^{\text{ht}} \cdot \text{MAC}^{\text{ht}} \left(\frac{t}{c}\right)_{max} \left(\frac{\text{AR}^{\text{ht}} n_{ult}}{cos(\Lambda_{c4}^{\text{ht}})}\right)^{0.6} \lambda_{\text{ht}}^{0.04} V_{\text{ht}}^{0.3} \left(\frac{c_{\text{elevator}}}{\text{MAC}^{\text{ht}}}\right)^{0.4} \\ M_{\text{vt}} = \rho_{\text{mat}} \cdot K_\rho \cdot S^{\text{vt}} \cdot \text{MAC}^{\text{vt}} \left(\frac{t}{c}\right)_{max} \left(\frac{\text{AR}^{\text{vt}} n_{ult}}{cos(\Lambda_{c4}^{\text{vt}})}\right)^{0.6} \lambda_{\text{vt}}^{0.04} V_{\text{vt}}^{0.2} \left(\frac{c_{\text{rudder}}}{\text{MAC}^{\text{vt}}}\right)^{0.4} \\ M_{\text{fus}} = \rho_{\text{mat}} \cdot K_\rho \cdot n_{\text{ult}}^{0.25} L_{\text{fus}} D_{\text{mean,fus}} \end{cases} \tag{3.2}$$

The ultimate load factor is supposed to be 1.5 times the maximum loading factor $n_{ult} = 1.5\ n_{max}$.

Figures 3.13 show the structural modelling of the wing and fuselage on OpenVSP.

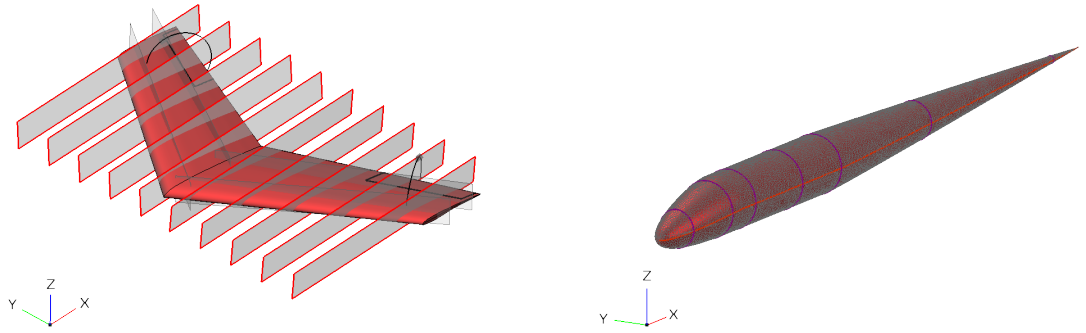

(a) Wing skin, ribs and spars (b) Fuselage structural modelling

Figure 3.13: MARS UAV: Structural modelling on OpenVSP

Additional components have been included, in particular: avionics and systems, solar panels, skid, electric motors and propellers. The mass of avionics and systems has been estimated as $M_{\text{sys}} = 0.500$ kg. Propellers made of carbon fiber reinforced material have been considered, of a diameter equal to $D = 20\ in$. The propeller mass has been estimated as $M_{\text{prop}} = 0.100$ kg each.

Various types of electric motors that are available off-the shelf have been analysed, as explained later in section 3.3.2. In this work, the determination of the required shaft power is given by the vertical take-off constraint, with the number of electric motors chosen based on the results of the study in Section 2.2. After establishing the total power needed, the T-Motor AT2826 900KV has been selected, distinguished by a mass of $M_{\text{em}} = 0.175$ kg.

The sizing of the solar panels follows the formulation outlined in section 3.1.2, where the absorbed power during one sol for each square metre of solar panels is computed. To limit the recharge time, it has been assumed that the wing surface should be covered as extensively as possible. Consequently, solar panels are installed on the first three-quarters of the wing chord, avoiding the last quarter due to the presence of ailerons in proximity of the wing tip. Subsequent verification confirmed that this design choice aligns coherently with the constraint on recharge time.

The solar panels consist of multiple thin, flexible cells. By determining the covered area, the number of cells was identified. To account for all auxiliary components necessary for

constructing the solar panels, a weight factor of $\omega_f = 0.85$ has been applied. The mass of the solar panels has been estimated as: $M_{\text{panels}} = \frac{N_{\text{cells}} M_{1\ \text{cell}}}{\omega_f}$.

Table 3.8 presents the results of the mass breakdown of the Mars UAV.

Component	**Estimated Mass**
Payload	$M_{\text{payload}} = 2.00$ kg
Wing	$M_{\text{wing}} = 3.66$ kg
Horizontal tail	$M_{\text{ht}} = 0.28$ kg
Vertical tail	$M_{\text{vt}} = 0.94$ kg
Fuselage	$M_{\text{fus}} = 4.87$ kg
Solar panels	$M_{\text{panels}} = 1.09$ kg
Avionics and systems	$M_{\text{sys}} = 0.50$ kg
Skid	$M_{\text{skid}} = 0.21$ kg
Electric motors and propellers	$M_{\text{em,prop}} = 1.63$ kg
Battery package	$M_{\text{battery}} = 4.80$ kg
Total Mass	MTOM = 20.00 kg

Table 3.8: Mars UAV: Mass breakdown

3.3.2. Sizing of the propulsive system

The propulsive system is formed by a battery package, a battery management system a thermal management system, 6 electric motors and 6 propellers. The selection of rotors was based on a trade-off study involving the consideration of the number of rotors and their diameters, along with the corresponding total power required to achieve vertical take-off. Each rotor is composed by 3 blades.

Results are reported by figure 3.14.

The graph illustrates that an increase in the number of rotors and their size has a favorable impact on the total power required for vertical take-off. It is noteworthy that an increase in the number of rotors results in a more complex configuration, while excessive augmentation of rotor diameter poses geometric challenges concerning the disposition of tilt-rotors relative to the wing and fuselage. Striking a balance between moderate total power requirements for take-off and complexity, six propellers with a diameter of 20 inches each ($D = 0.508\ m$) have been selected. The total power required for vertical take-off is $P_{b,TO} = 4.40\ kW$.

A maximum tip Mach number of $M_{\text{tip}} = 0.76$ has been imposed, hence the number of

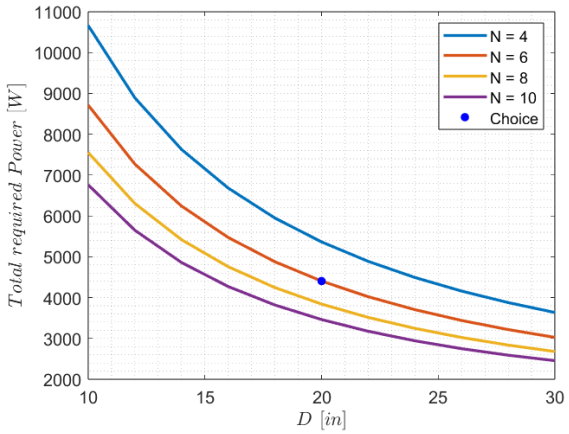

Figure 3.14: Power required at vertical take-off

maximum revolutions per minute RPM_{max} has been retrieved. Correspondingly, the maximum tip velocity at zero altitude $h_{VTO} = 0\ m$ is equal to $v_{\text{tip}} = 185.74\ \frac{\text{m}}{\text{s}}$, the limit on maximum RPM is $RPM_{\text{max}} = 6983\ RPM$.

Various types of electric motors are available in the market, with brushless motors being particularly prevalent for small and medium-sized UAVs. This study has considered several off-the-shelf electric motors, with a focus on those manufactured by T-MOTOR for fixed-wing UAVs. For the Mars UAV, T-Motor AT2826 900KV has been selected, with a motor efficiency of $\eta_{motor} = 0.90$ taken into account. Details are provided in table 3.9.

Characteristics	Value
Mass	$M_{\text{em}} = 0.175$ kg
Peak current (180 s)	$I_{\text{max}} = 57$ A
Max power (180 s)	$P_{\text{max}} = 820$ W
Idle current	$I_{\text{idle}} = 2.2$ A

Table 3.9: T-MOTOR AT2826 KV900 specifications

The battery package comprises a collection of cells, as detailed in section 3.1.2, arranged both in series and in parallel, in order to increase, respectively, the voltage or the capacity of the system.

Throughout the preliminary design phase, two different procedures for the sizing of the propulsive system have been applied. Within the optimization loop, a simplified approach was employed: The Maximum Take-Off Mass (MTOM) was held constant at $MTOM = 20$ kg. Based on the values assumed by the design variables at each iter-

ation, the UAV geometry was constructed, enabling the estimation of the mass for all components excluding the battery package. The battery mass was then determined as the difference between the MTOM and the sum of the masses of all other components, expressed as: $M_{\text{battery}} = \text{MTOM} - \sum_{i=1}^{N_{\text{components}}} M_i$.

After determining the mass of the battery package, the specific energy is derived from the characteristics of the cells comprising the battery package $e^* = 450\ \frac{\text{Wh}}{\text{kg}}$, along with the minimum state of charge $SOC_{\text{min}} = 10\%$, and the weight factor $\omega_f = 0.85$. The storable energy has been retrieved.

The mission profile has been analysed in order to compute the energy required by each flight phase. The energy required at the battery during vertical take-off, first transition, climb, descent, second transition and vertical landing has been computed. Consequently, the energy available for the cruising phase has been retrieved as the difference by the total energy stored by the battery and the consumed energy. The power required at the battery during the cruising phase is $P_{\text{battery,cruise}} = \frac{1}{\eta_p \eta_{\text{em}}} \frac{1}{2} \rho_{\text{cruise}} v_{\text{cruise}}^3 C_D S$. From the energy available for cruise, and the power required at the battery, the cruising time, and cruising distance have been computed.

An alternative approach to size the propulsive package has been considered, beginning with the characteristics of the individual cells comprising the battery package. Following the completion of the optimization process and the establishment of UAV specifications, a detailed UAV model has been created using OpenVSP and subsequent vortex lattice method (VLM) analyses have been conducted, providing a new polar of the UAV. Being low-fidelity aerodynamic simulations, VLM still exhibit limitations, especially at relatively high or high angles of attack, but they align with the requirements of this preliminary design study. The VLM simulations are deemed more reliable compared to the aerodynamic model implemented in MATLAB, which relies on Prandtl theory and the build-up drag method [38].

From the results of the new polar of the UAV, a new energetic analysis of the flight profile has been carried out. The method used for the sizing of the battery package is similar to the one presented in reference [52], accounting for multiple constraints, the cell characteristics and performance deterioration with an the discharge current and state of discharge, as shown in section 3.1.2.

The number of cells that is required to connect in parallel (N_p) is the result of two constraints. The first ($N_{p,\text{TO}}$) requires that the battery package is able to deliver the maximum power required, equal to the power required to perform the vertical take-off $\left(P_{\text{battery},max} = \frac{P_{req,VTO}}{\eta_p \eta_{\text{em}}}\right)$, even when the battery package is partially discharged. This

conditions considers the situation in which at the end of the mission, during vertical landing, it is required to deploy the maximum power for a short time due to an emergency. The second constraint ($N_{p,\text{cap}}$) regards the capacity of the battery package, that must be sufficient to guarantee that the package can store enough energy for the conduction of the design mission profile.

$$\begin{cases} N_{p,\text{TO}} = \frac{P_{\text{battery,max}}}{V_{\text{cell}}(\text{SOC},I)N_s Q_{\text{cell}} C_{\text{rate,max}}} \\ N_{p,\text{cap}} = \frac{E_{\text{battery,mission}}}{V_{\text{cell}} Q_{\text{cell}}} \\ N_p = max(N_{p,\text{TO}}\ ,\ N_{p,\text{cap}}) \end{cases} \tag{3.3}$$

where, the energy required at the battery during the complete mission is equal to

$$\begin{aligned} E_{\text{battery,mission}} = P_{\text{battery,VTO}} t_{\text{VTO}} \ + \ P_{\text{battery,transition}} t_{\text{transition}} \ + \\ + \ P_{\text{battery,climb}} t_{\text{climb}} \ + \ P_{\text{battery,cruise}} t_{\text{cruise}} \ + \ P_{\text{battery,descent}} t_{\text{descent}} \ + \\ + \ P_{\text{battery,transition2}} t_{\text{transition2}} \ + \ P_{\text{battery,VLND}} t_{\text{VLND}} \end{aligned} \tag{3.4}$$

Considering the number of cells to be connected in series (N_s), this affects the maximum voltage of the battery package. The voltage of the battery package must be compatible with the minimum and maximum allowable by the electric motors.

$$N_s = \frac{V_{\text{battery}}}{V_{\text{cell}}} \tag{3.5}$$

The number of cells to be connected in series and in parallel has been computed, accounting for a weight factor $\omega_f = 0.85$ to consider all additional components forming the battery package (structures, cables, connectors ...), the new total mass of the battery package has been retrieved and the mission range has been verified.

N cells in series	N cells in parallel	Total number of cells	Total mass
$N_s = 4$	$N_p = 6$	$N_{\text{tot}} = 24$	$M_{\text{battery}} = 4.68$ kg

Table 3.10: Battery Package Data

The prediction of the battery discharge during the mission is illustrated by figure 3.15. Table 3.11 shows the characteristics of the recharging system of the Mars UAV.

3.3.3. Aerodynamics

The assessment of aerodynamic performance has been carried out in this section. Particular focus was set to the cruising condition, which is at a Reynolds number of $Re =$

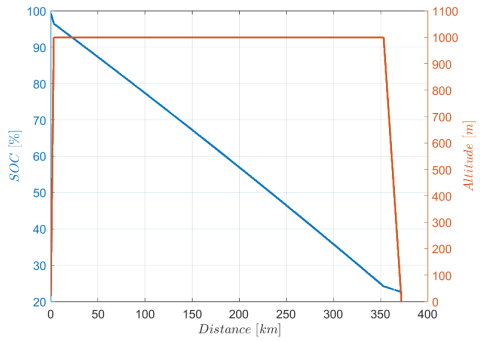

Figure 3.15: Discharge of the battery package

Parameter	Value
N solar cells	$N_{\text{solar cells}} = 746$
Total area	$A_{\text{panels}} = 1.85\ \text{m}^2$
Mass	$M_{\text{panels}} = 1.09\ \text{kg}$
Daily specific energy	$e^*_{\text{daily}} = 802\ \frac{\text{Wh}}{\text{m}^2}$
Recharge time	$t_{\text{recharge}} = 1.22$ sols

Table 3.11: Characteristics of the recharging system

92 000 and Mach number $M = 0.38$. At cruise, the Reynolds number is lower than the critical Reynolds number, it is in the low Reynolds regime. As presented in section 2.1.1, this regime suggests the use of sharped leading edge airfoils with low thickness-to-chord ratio.

Airfoils

In the low Reynolds regime, the Ishii airfoil is proven as one of the best airfoils in terms of performance, especially referring to the maximum lift-to-drag ratio, which is the key parameter in order to extend as maximum as possible the mission range of propeller driven aircrafts. Hence, Ishii has been selected as the airfoil for the wing of the Mars UAV.

The effects of Reynolds number and Mach number on the polar and C_l, α curve of Ishii airfoil have been drafted using Xfoil, and illustrated by figure 3.16 and 3.17.

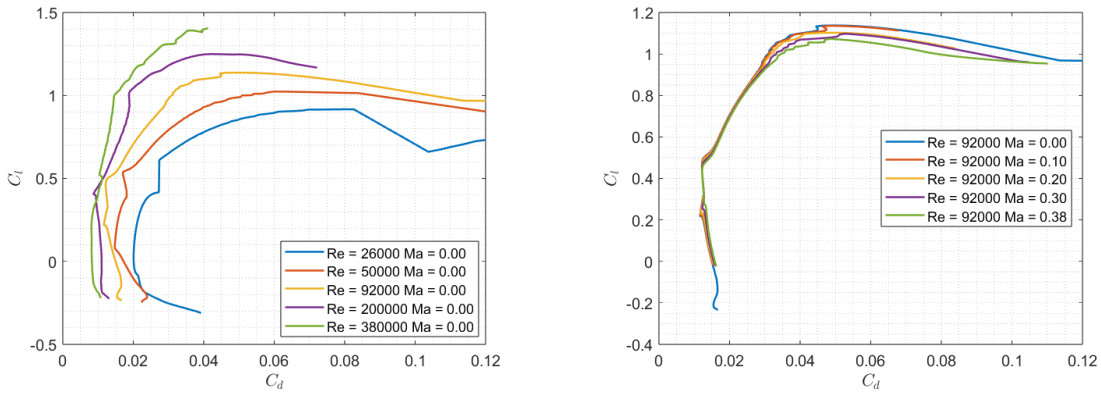

(a) Effects of Reynolds number variation

(b) Effects of Mach number variation

Figure 3.16: Ishii: Effects of Reynolds and Mach on polar curves on Xfoil

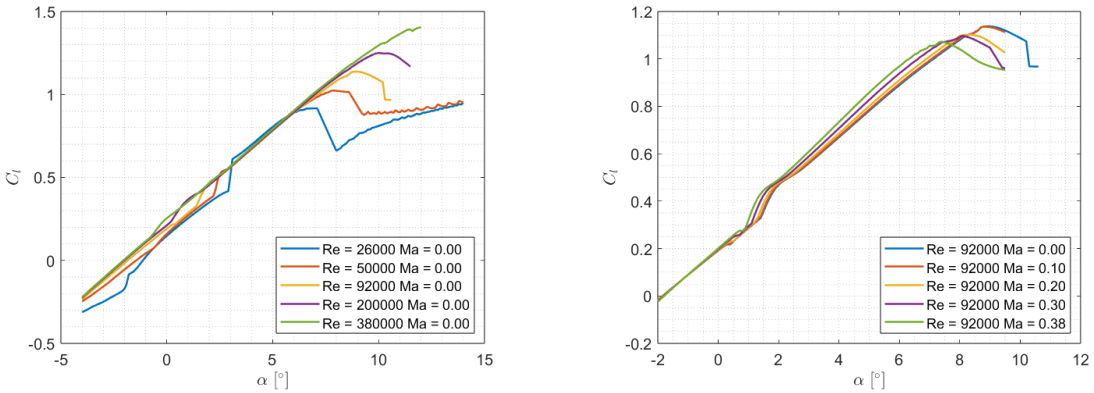

(a) Effects of Reynolds number variation

(b) Effects of Mach number variation

Figure 3.17: Ishii: Effects of Reynolds and Mach on (C_l, α) curves on Xfoil

For the airfoil selection for the horizontal tail and vertical tail, NACA 0006 and NACA 0012 airfoils have been compared. The Reynolds associated to the mean aerodynamic chord of the horizontal tail is $Re^{\text{ht}} = \frac{\rho_{\text{cruise}} v_{\text{cruise}} \text{MAC}^{\text{ht}}}{\mu_{\text{cruise}}} = 32000$. Where ρ_{cruise} and μ_{cruise} are the atmospheric density and dynamic viscosity at $h_{\text{cruise}} = 1000$ m.

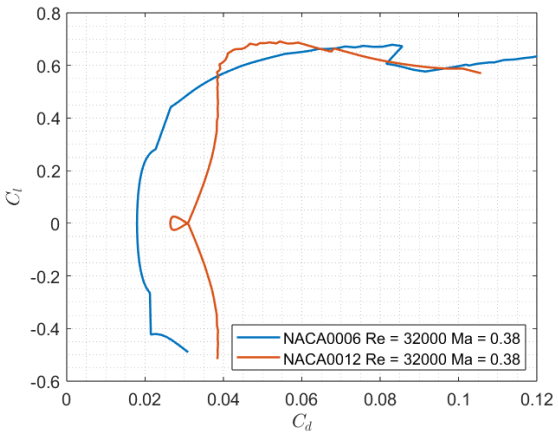

Figure 3.18: Polar curves of NACA 0006 and NACA 0012 at cruise conditions on Xfoil

The NACA 0006 airfoil reports a significantly lower drag coefficient at cruising condition on Mars, in accordance with the theory. Hence, it has been selected as the airfoil of the horizontal and vertical tail.

Wing geometry

In order to avoid excessively low Reynolds numbers, a low aspect-ratio wing was preferred to a high aspect ratio wing. With regard to the wing geometry, a taper ratio of $\lambda = 0.6$ was

adopted to mitigate the induced drag component and root bending moment while avoiding excessively low tip Reynolds numbers that could adversely impact the wing's aerodynamic performance in that region. During cruise, the wing tip operates at a Reynolds number around $Re_{\text{tip}} \simeq 65000$. The dihedral angle was set to $\phi = -4°$ due to lateral-directional stability considerations.

The cruising Mach number is moderate, $M = 0.38$, therefore a swept wing was not required in order to avoid the drag rise phenomenon, but a quarter chord sweep angle equal to $\Lambda_{c4} = 35°$ has been selected as the result of a study on the positioning of the propellers in order to adopt configuration for the vertical take-off and vertical landing phases. This setup permits the alignment of propellers with respect to the centre of mass, as illustrated by figure 3.19.

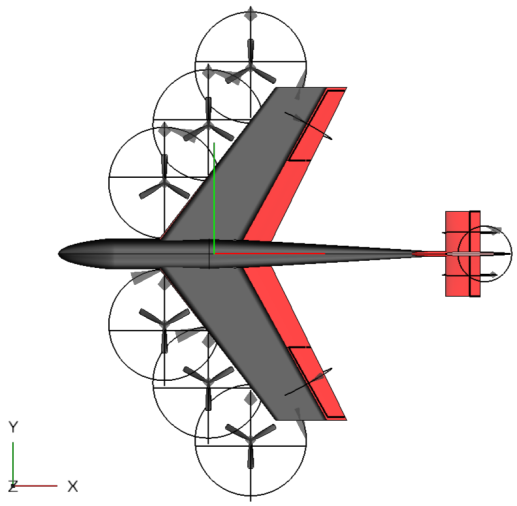

Figure 3.19: Vertical take-off and landing configuration

Table 3.12 presents the characteristics of the aerodynamic surfaces of the Mars UAV.

Parameter	Wing	Horizontal Tail	Vertical Tail
Wing surface	$S = 2.53\ m^2$	$S = 0.236\ m^2$	$S = 0.52\ m^2$
Wingspan	$b = 3.0\ m$	$b = 0.76\ m$	$b = 0.76\ m$
Airfoil	Ishii	NACA0006	NACA0006
Aspect ratio	AR = 3.55	AR = 2.45	AR = 1.11
Mean aerodynamic chord	MAC = 0.85 m	MAC = 0.31 m	MAC = 0.66 m
Incidence	$i = 6°$	$i = -4°$	$i = 0°$
Taper ratio	$\lambda = 0.6$	$\lambda = 1.0$	$\lambda = 0.8$
Sweep angle	$\Lambda_{c4} = 35°$	$\Lambda_{c4} = 0°$	$\Lambda_{c4} = 20°$
Dihedral	$\Gamma = -4°$	$\Gamma = 0°$	$\Gamma = 0°$

Table 3.12: Aerodynamic surfaces geometry

UAV Polar

In order to evaluate the performance of the UAV, VLM analyses on OpenVSP have been carried out. The geometry of the UAV was simplified to the fuselage, wing, horizontal and vertical tail. Figure 3.20 shows the results of the VLM analyses at cruising conditions, at $Re = 92\ 000$ and $M = 0.38$.

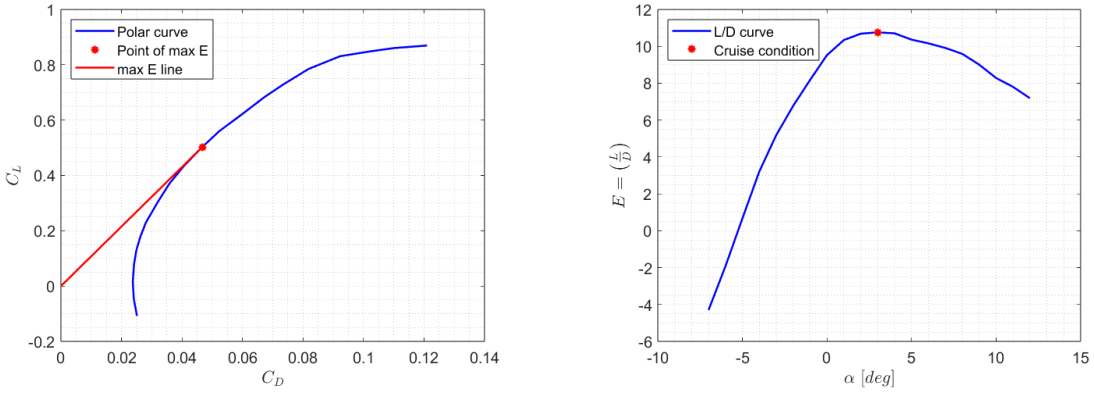

(a) Polar Curve (b) Lift to Drag ratio versus α

Figure 3.20: VLM Results on OpenVSP

In order to enhance the mission range, the UAV must operate at maximum lift-to-drag ratio, hence at $C_L = 0.51$ and $\alpha = 3°$. A maximum lift-to-drag ratio $\left(\frac{L}{D}\right) = 11$ has been retrieved.

3.3.4. Stability

At a first stage, control fixed static stability analysis have been conducted using MATLAB, following the formulation outlined by Roskam [34] and Pamadi [32].

Longitudinal static stability requires the pitching moment about the centre of mass of the UAV to be negative $C_{m_{G\alpha}} < 0$. It has been guaranteed making reference to the two surface formulation. The static margin (SM) was set to be in the range $5 \leq SM \leq 25$ %, in order to guarantee longitudinal static stability along with good maneuverability. The static margin is defined as the longitudinal distance between the centre of mass (X_G) and the aerodynamic centre of the aircraft (X_{AC}), nondimensionalised with respect to the wing mean aerodynamic chord $\text{SM} = \frac{X_G - X_{\text{AC}}}{\text{MAC}}$. The obtained static margin for the trimmed cruising condition is SM = 20.9 %.

The lateral static stability requires $C_{l_{G\beta}} < 0$ for the rolling moment and the directional static stability $C_{n_{G\beta}} > 0$ for the yawing moment. Moreover, simplified models for the longitudinal and lateral-directional dynamics have been implemented in MATLAB.

Later, stability analyses have been carried out using OpenVSP. Hence, light adaptations to the UAV geometry and the disposition of internal components have been made to guarantee a proper positioning of the centre of mass and the neutral point. Control surfaces have been sized according to the formulation reported by Sadraey [36]. Elevator, aileron and rudder are extended 25% of the local chord.

Figure 3.21 illustrates the eigenvalue maps of the longitudinal and lateral-directional dynamics of the UAV, starting from the cruising equilibrium condition.

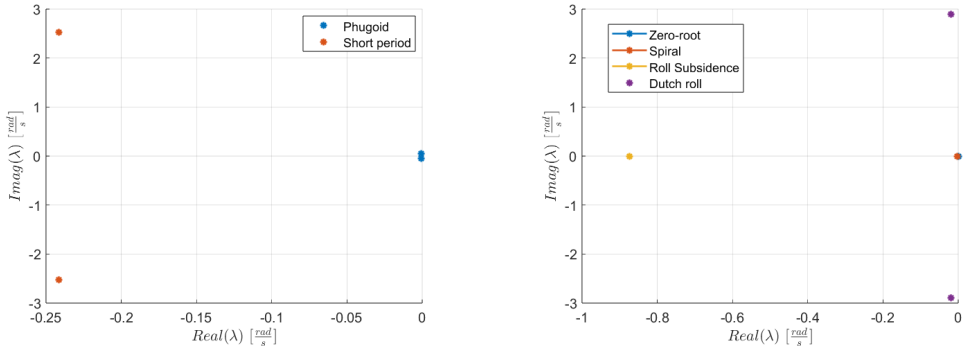

(a) Longitudinal dynamics (b) Lateral-directional dynamics

Figure 3.21: Eigenvalue Maps: Longitudinal and lateral-directional dynamics

Parameter	Value
Centre of gravity longitudinal position	$X_{CG} = 0.82\ m$
Horizontal tail surface ratio	$\frac{S_{\text{ht}}}{S} = 0.093$
Tail volume coefficient	$V_{\text{ht}} = 0.216$
Vertical tail surface ratio	$\frac{S_{\text{vt}}}{S} = 0.197$
Vertical tail volume coefficient	$V_{\text{vt}} = 0.107$
$C_{m_{G\alpha}}$	$C_{m_{G\alpha}} = -0.712\ \frac{1}{rad}$
$C_{l_{G\beta}}$	$C_{l_{G\beta}} = -0.171\ \frac{1}{rad}$
$C_{n_{G\beta}}$	$C_{n_{G\beta}} = 0.308\ \frac{1}{rad}$

Table 3.13: Mars UAV: Stability data

It is worth noting that the rarefied atmospheric conditions on Mars necessitate a significant oversizing of the vertical tail compared to conventional UAVs to ensure lateral-directional stability. Typically, the vertical tail volume coefficient falls within the range of $V_{\text{vt}} = 0.02 - 0.04$.

3.4. Results

The Mars UAV features a conventional tail configuration and is equipped with six tilting rotors, each with a diameter of 20 inches, providing Vertical Take-Off and Landing (VTOL) capabilities. Additionally, wing-mounted solar panels are incorporated to ensure self-charging capabilities in the Martian environment. The fuselage spans a length of 3.65 metres with a maximum diameter of 0.275 metres. The UAV has a maximum take-off mass of 20 kg, including a 2 kg payload, and a battery package with a mass of 4.68 kg. The mission range is equal to $R = 375$ km.

This section is devoted to the illustration of the Mars UAV, the presentation of its main features and the mission profile.

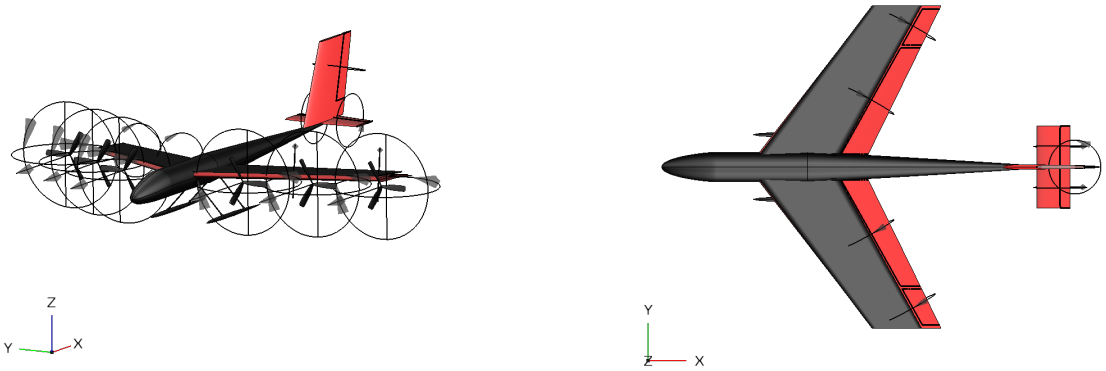

(a) Front-Left view (b) Top view

Figure 3.22: Mars UAV front-left and top views

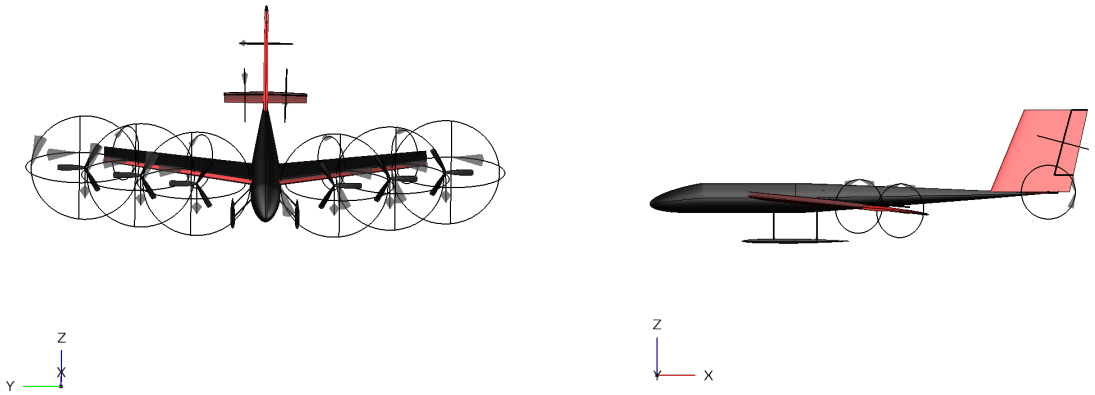

(a) Front view (b) Lateral view

Figure 3.23: Mars UAV front and lateral views

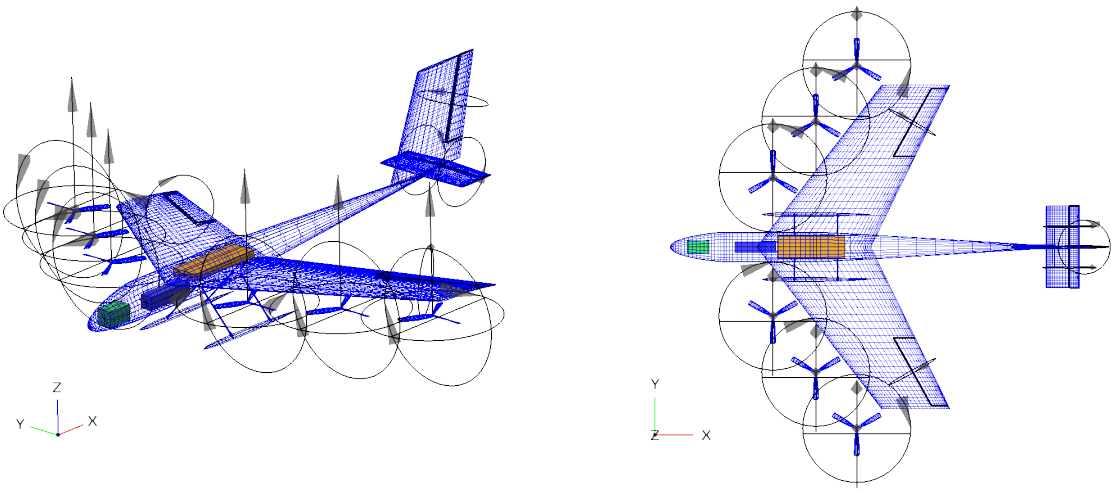

(a) Front-left view (b) Top view

Figure 3.24: Mars UAV view of internal components

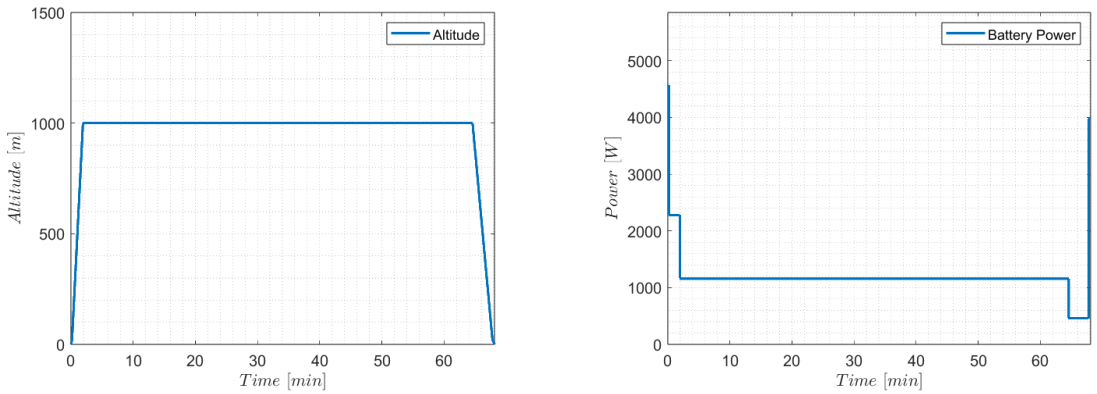

(a) Altitude versus time (b) Battery power versus time

Figure 3.25: Altitude and battery power versus time

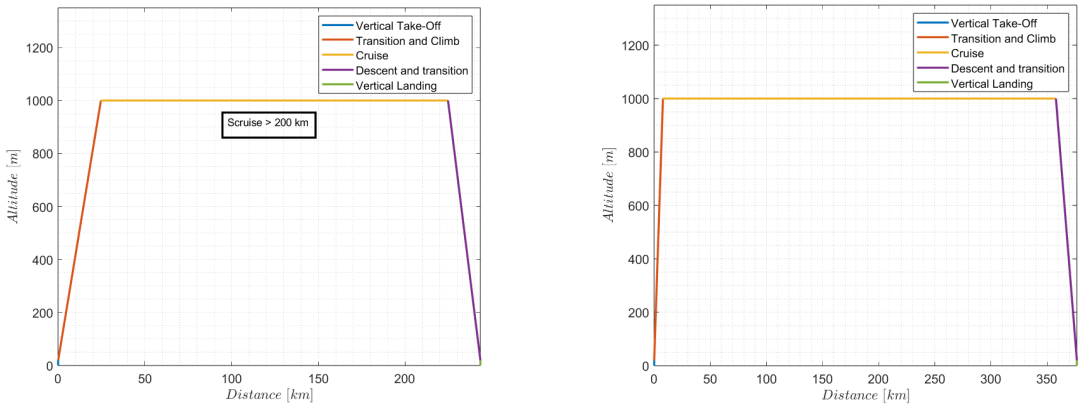

(a) Baseline mission profile

(b) Actual mission profile

Figure 3.26: Mars UAV Mission Profile comparison

Flight Phase	Parameter	Value
Vertical Take-Off	Vertical velocity, for $t = 20$ s	$V_{v\ \mathrm{TO}} = 1.3\ \frac{\mathrm{m}}{\mathrm{s}}$
Climb	Rate of Climb, max 180 s	$V_v = 32.0\ \frac{\mathrm{m}}{\mathrm{s}}$
Cruise	Design cruising speed (V_{cruise})	$V_{\mathrm{cruise}} = 92.0 \frac{\mathrm{m}}{\mathrm{s}}$
Transition	Stalling speed (V_{stall})	$V_{\mathrm{stall}} = 51.2 \frac{\mathrm{m}}{\mathrm{s}}$
Maneuver	Maximum load factor (n_{max})	$n_{\mathrm{max}} = 1.4$
Service ceiling	Altitude (h_{ceiling})	$h_{\mathrm{ceiling}} > 3000$ m
Transition	Maximum lift coefficient	$C_{L\,\mathrm{max}} = 0.87$
Cruise	Design lift coefficient	$C_{L,\mathrm{cruise}} = 0.50$
Cruise	Maximum $E = \frac{L}{D}$	$E_{\mathrm{max}} = 10.76$
Fastest climb	Maximum $F = E\sqrt{C_L}$	$F_{\mathrm{max}} = 8.50$

Table 3.14: Mars UAV: Data

4 | Design of the Earth UAV

4.1. Pre-conceptual design

This section presents the design of a fixed-wing UAV conceived to replicate on Earth the baseline mission profile of the Mars UAV.

The terrestrial drone incorporates electric propulsion, wing-mounted solar panels, and employs identical battery technology to that utilized by the Mars UAV. In this context, lithium metal oxide cells have been chosen, with their corresponding characteristics detailed in section 3.1.2, as outlined in tables 3.1 and 3.2.

Regarding the material selected for the Earth UAV, carbon fibre composites have been used, with an estimated density of $\rho = 1596 \frac{\text{kg}}{\text{m}^3}$. Given the necessity for vertical take-off and landing, the UAV employs a tilt-rotor configuration. To align with the design cruising altitude of the Mars UAV, the Earth UAV maintains a cruising altitude set at $h_{\text{cruise}} = 1000$ m.

4.1.1. Initial Requirements

The Earth UAV is conceived to accommodate an identical payload as the Mars UAV. The objective for the design of the terrestrial drone is to minimize its maximum take-off mass, ensuring a minimum mission range of $R \geq 200\ km$.

Based on the findings outlined in section 2.2, it is anticipated that the terrestrial UAV will exhibit more compact dimensions, when compared to the Mars UAV. This is due to the greater density on Earth, roughly 81.7 times greater ($\frac{\rho_{Earth}}{\rho_{Mars}} = 81.7$) at 0 metres altitude; and despite the fact that gravitational acceleration is larger on Earth, around 2.63 times greater ($\frac{g_{Earth}}{g_{Mars}} = 2.63$).

The initial requirements for the design of the Earth UAV have been collected and reported in table 3.3.

Characteristics	Requirements
Payload Mass	$M_{\text{payload}} = 2.0$ kg
Mission Range	$R \geq 200$ km
Maximum Take-Off Mass	MTOM ≤ 10 kg
Fuselage Maximum Length	$L_{\text{fus}} \leq 1.8$ m
Maximum Wingspan	$b \leq 1.5$ m
Propulsive system	Electric

Table 4.1: Initial requirements

It's noteworthy that, in this design, no constraints have been imposed on the recharge time of the UAV. Consequently, there are no restrictions on the sizing of the recharging system or the wing area to be covered by the solar panels. Despite the higher solar irradiance on Earth compared to Mars, as established in the introduction 1.2.2, the Earth UAV will be designed with a significantly smaller wing surface than the Martian drone. Even with the increased solar intensity, the system will not be capable of recharging the UAV within a reasonable time frame, ideally, within a few hours to a maximum of one day. Therefore, the sizing of the wing-mounted solar panels is such to provide sufficient power to feed the onboard electronics, estimated at approximately $P_{electronics} \simeq 10 - 20\ W$.

4.1.2. Baseline mission profile

The Earth UAV has been conceived to replicate in the terrestrial environment, the mission profile of the Mars UAV. Hence, the baseline mission profile is identical to the one of the Martian drone. Detailed characteristics can be found in section 3.1.4.

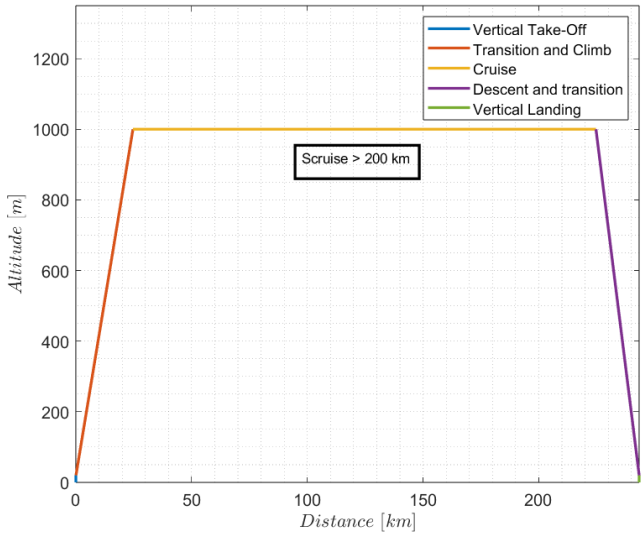

Figure 4.1: Design Mission Profile

4.1.3. Performance requirements

Similarly to the Martian case, also for the Earth UAV specific targets have been established across various parameters to ensure satisfactory performance.

Mission Phase	Parameter	Configuration	Value
Vertical Take-Off	Vertical velocity ($V_{v\ \mathrm{TO}}$)	Vertical thrust	$V_{v\ \mathrm{TO}} \geq 2\ \frac{\mathrm{m}}{s}$
Climb	Rate of Climb (RC *or* V_v)	Clean	$V_v \geq 12\ \frac{\mathrm{m}}{\mathrm{s}}$
Climb	Climb angle (CGR *or* γ)	Clean	$\gamma_{\max} \geq 22°$
Cruise	Cruising speed (V_{cruise})	Clean	$V_{\mathrm{cruise}} \geq 25\ \frac{\mathrm{m}}{\mathrm{s}}$
Cruise	High speed cruise ($V_{\max}$)	Clean	$V_{\max} \geq 65\ \frac{\mathrm{m}}{\mathrm{s}}$
Transition	Stalling speed (V_{stall})	Clean	$V_{\mathrm{stall}} \leq 24\ \frac{\mathrm{m}}{\mathrm{s}}$
Maneuver	Maximum load factor ($n_{\max}$)	Clean	$n_{\max} = 1.6$
Service ceiling	Altitude ($h_{ceiling}$)	Clean	$h_{ceiling} \geq 9000$ m

Table 4.2: Target performance

Exploiting the fact that the terrestrial environment allows to obtain a higher wing loading, hence a smaller and lighter wing with respect to the Martian case, a more stringent requirement on the maximum load factor have been enforced, $n_{\max} = 1.6$. All velocities in table 4.2 are true airspeeds.

4.1.4. Required aerodynamic coefficients

As mentioned, the terrestrial UAV is expected to have more compact dimensions with respect to the Mars UAV. Nevertheless, it will operate at larger Reynolds. The avoidance of the low Reynolds regime allows to demand enhanced aerodynamic performance. Therefore, more severe constraints have been set, especially when referring to $C_{L\,\max}$, E_{cruise} and $F_{\max}$.

Mission Phase	Parameter	Configuration	Value
Transition-to-climb	C_{Lmax}	Clean	1.0
Cruise	C_L *target*	Clean	0.4-0.65
Cruise	$E = \frac{L}{D}$	Clean	16
Fastest climb	$F_{\max}$	Clean	15
Descent-to-transition	C_{Lmax}	Clean	1.0

Table 4.3: Target aerodynamic coefficients

4.2. Conceptual design

Similarly to the case of the Mars UAV, a sizing matrix plot have been drafted in order to identify the optimal design point that satisfies all constraints related to geometry, performance and aerodynamics.

4.2.1. Sizing Matrix Plot

Figure 3.11 illustrates the sizing matrix plot.

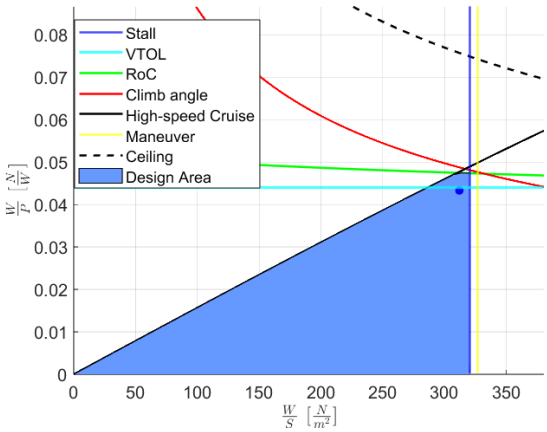

Figure 4.2: Sizing Matrix Plot

The results of the sizing matrix plot provide a wing loading of $\frac{W}{S} = 311.98\ \frac{N}{m^2}$, and a power loading equal to $\frac{W}{P_b} = 0.0432\ \frac{N}{W}$.

4.2.2. Concept

The winning concept for the Earth UAV adopts a conventional tail configuration, prioritizing controllability and decoupling longitudinal and lateral-directional dynamics. This design incorporates solar panels mounted on the wings to facilitate onboard electronics with power during the day. A tilt-rotor configuration has been selected to avoid structural and manufacturing complexities derived by the tilt-wing configuration.

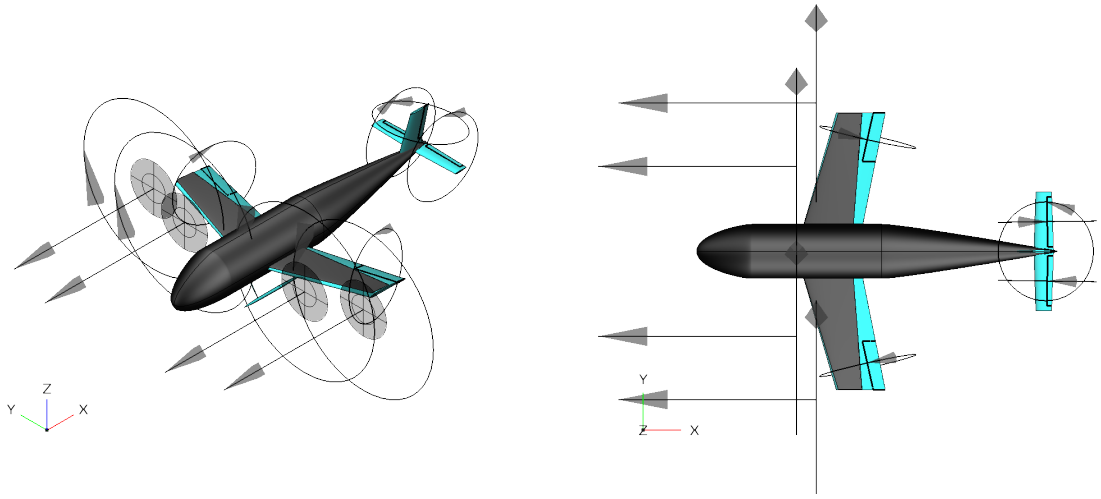

(a) Front-left view (b) Top view

Figure 4.3: Concept of the Earth UAV

4.3. Preliminary design

The task of the Earth UAV is to replicate in the terrestrial environment the flight profile of the Martian drone, drafted for the execution of the scientific mission on Mars. To achieve this goal, the mission range of the Earth UAV is mandated to meet or exceed the baseline mission range for the Mars UAV. The primary objective is to design a UAV that complies with this requirement while minimizing its mass. Consequently, a multidisciplinary optimization framework have been set up, adapting the the Mars UAV case. However, the optimization objective function has been redefined to as the maximum take-off mass of the eVTOL UAV $f_{obj} = \text{MTOM}$.

The design variables selected for the constrained optimisation problem are the same of

the Martian case, reported by the following table 4.4. In addition, a new design variable has been considered: the maximum take-off mass MTOM.

Constraints
$0.5 \leq b \leq 1.5$ m
$0.4 \leq \lambda \leq 1.0$
$0.6 \leq b^{\text{ht}} \leq 1.5$ m
$0.2 \leq V^{\text{ht}} \leq 0.8$
$0.6 \leq L^{\text{ht}} \leq 1.5$ m
$0.2 \leq b^{\text{vt}} \leq 0.5$m
$0.02 \leq V^{\text{vt}} \leq 0.2$
$0.6 \leq L^{\text{vt}} \leq 1.5$ m
MTOM ≤ 10 kg

Table 4.4: Constraints on the design variables

Also for the terrestrial case, the MATLAB function *fmincon* has been used for the setup of the optimisation problem. The optimisation tool stops when the step between two iterations falls below a specified value ($step_{\text{min}} = 10^{-4}$), or when the maximum number of iterations is reached ($iter_{\text{max}} = 200$).

The design tool adopts same logic presented in section 3.3, with the key distinction that MTOM is now a variable, allowing the utilization of results of the SMP in each iteration to compute the wing surface S and the maximum shaft power that must be installed P_b. Afterwards, the procedure aligns with the steps detailed in list 11. At point 8, a verification is carried out to ensure that the mission range is above the minimum limit specified. At point 11, the objective function is modified to $f_{obj} = \text{MTOM}$.

From the results of the optimisation loop, the geometry of the UAV has been created using OpenVSP and mass properties have been assigned. Results indicate a maximum take-off mass equal to MTOM = 7.50 kg. The wing surface is equal to $S = 0.2352$ m^2 and the maximum shaft power is $P_b = 1.67$ kW.

4.3.1. Mass breakdown

Table 4.5 presents the results of the mass breakdown of the terrestrial UAV.

Component	Estimated Mass
Payload	$M_{\text{payload}} = 2.00$ kg
Wing	$M_{\text{wing}} = 0.33$ kg
Horizontal tail	$M_{\text{ht}} = 0.03$ kg
Vertical tail	$M_{\text{vt}} = 0.04$ kg
Fuselage	$M_{\text{fus}} = 0.66$ kg
Solar panels	$M_{\text{panels}} = 0.22$ kg
Avionics and systems	$M_{\text{sys}} = 0.50$ kg
Skid	$M_{\text{skid}} = 0.15$ kg
Electric motors and propellers	$M_{\text{em,prop}} = 0.45$ kg
Battery package	$M_{\text{battery}} = 3.12$ kg
Total Mass	MTOM $= 7.50$ kg

Table 4.5: Earth UAV: mass breakdown

4.3.2. Sizing of the propulsive system

In the Earth UAV design process, a trade-off study was conducted to assess the relationship between the required shaft power for vertical take-off and rotor number and diameter. The objective was to limit the total power required for vertical take-off, without unnecessary complexity associated with a large number of rotors.

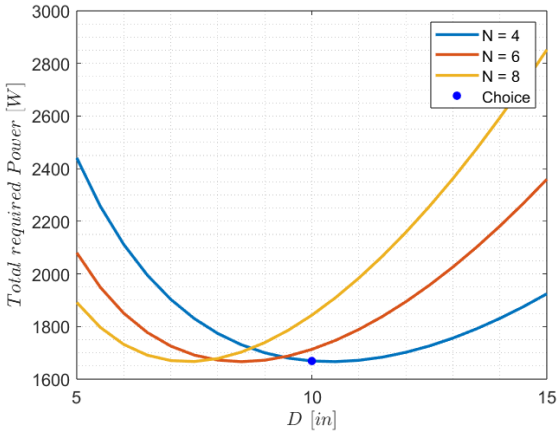

Figure 4.4: Earth UAV: Power required at vertical take-off

In this investigation, scenarios involving four, six, or eight rotors have been evaluated, each with a diameter ranging from 5 to 15 inches. The minimum power required appears to be little affected by the number of rotors, as long as the appropriate rotor diameter is selected.

This phenomenon arises from the reduction in induced power with an increase in both rotor diameter and number of rotors, while the opposite holds true for profile power. This trend is observed in the Martian case too, but with a notable difference: the profile power is considerably lower than the induced power component. Therefore, at Martian conditions, the total power required exhibits a decreasing trend with the increment of rotor diameter and the number of rotors.

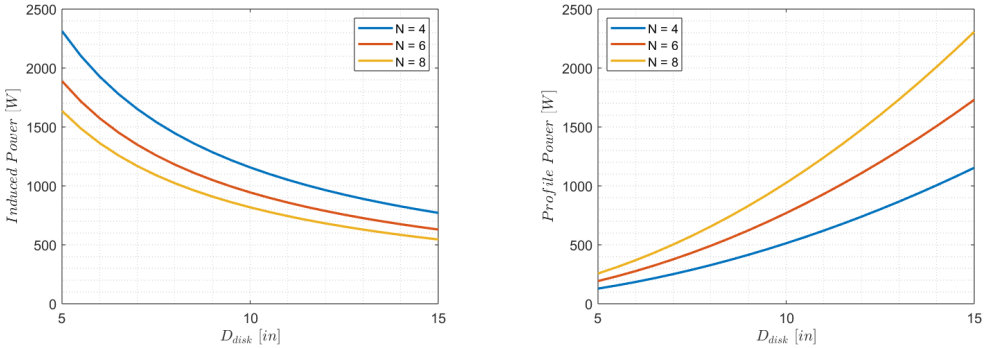

(a) Induced Power (b) Profile Power

Figure 4.5: Induced and profile power at vertical-take off

The quadrotor configuration is the simplest in terms of manufacturing complexity, hence it has been adopted for the design of the terrestrial drone. As a result, the total shaft power required at vertical take-off is $P_{b,\mathrm{TO}} = 1.67\ k\mathrm{W}$, therefore, the battery must be capable to provide $P_{\mathrm{max,battery}} = 1.80\ k\mathrm{W}$

In order to size the battery package based on the specifications of a single cell, the same approach presented in section 3.3.2 has been used. Results of the sizing of the battery package are reported by table 4.6.

N cells series	N cells parallel	Total Number of Cells	Total Mass
$N_s = 4$	$N_p = 4$	$N_{\mathrm{tot}} = 16$	$M_{\mathrm{battery}} = 3.12$ kg

Table 4.6: Battery package data

The electric motor has been selected in agreement with the coupling requirements of the four propellers, of 10 inches diameter. Charactetistics are reported by table 4.7.

Characteristics	Value
Mass	$M_{em} = 0.093$ kg
Peak current (180s)	$I_{max} = 30$ A
Max power (180s)	$P_{max} = 450$ W
Idle current	I_{idle} 1.2 A

Table 4.7: T-MOTOR AT2321 KV950 specifications

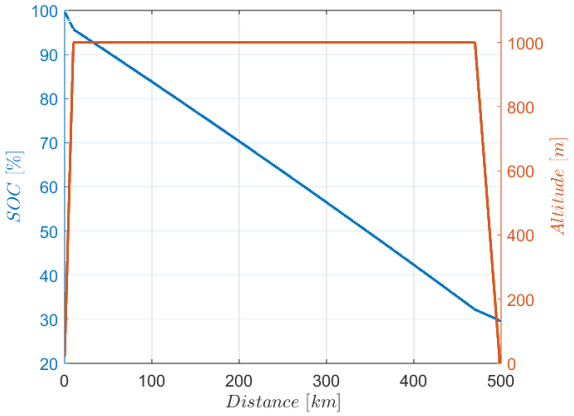

Table 4.8: Discharge of the battery package

The sizing of the wing-mounted solar panels aimed to provide sufficient power to the onboard electronics, exploiting the ModelE AR5 Simulations [37]. The software required as input the coordinates of the location where it was required to compute the daily insolation, along with the month of the year. For this analysis, Milano and June 2023 have been selected. Results of the sizing of the solar panels are presented in table 4.9.

Parameter	Value
N solar cells	$N_{\text{solar cells}} = 69$
Total area	$A_{\text{panels}} = 0.17$ m^2
Mass	$M_{\text{panels}} = 0.22$ kg
Mean power	$P_{\text{mean}} = 13$ W
Daily specific energy	$e^*_{\text{daily}} = 1120\ \frac{\text{Wh}}{\text{m}^2}$

Table 4.9: Solar panels data

4.3.3. Aerodynamics

All flight phases underwent comprehensive analysis to assess performance, with particular attention given to the cruising phase. This phase, being the predominant contributor in terms of both time and distance within the flight profile, was deemed most crucial in shaping design decisions. To enhance the mission range, the cruise phase is carried out at maximum lift-to-drag ratio, determined at $C_L = 0.60$. The wing mean aerodynamic chord measures MAC $= 0.168$ m and the wing surface is $S = 0.2352$ m^2. From equilibrium, the cruising speed is close to $v_{\text{cruise}} = 31\ \frac{\text{m}}{\text{s}}$. At an altitude of 1000 metres, $h_{\text{cruise}} = 1000$ m, the international standard atmosphere presents an atmospheric density of $\rho_{\text{cruise}} = 1.112 \frac{\text{kg}}{\text{m}^3}$, a speed of sound of $c_{\text{cruise}} = 336.4 \frac{\text{m}}{\text{s}}$, leading to a Reynolds number of $Re = 330\ 000$ and

a Mach number of $M = 0.09$.

Airfoils

To select the wing airfoil, a comprehensive comparison of several airfoils was conducted. A scoring system was established, aligning with the target aerodynamic performance outlined in table 4.3, that are inherently associated with the aerodynamic characteristics of the airfoils. The scoring system involves evaluations of $C_{l\ max}$, E_{max}, F_{max}, $C_{d\ min}$, and $C_{m\ at\ E_{max}}$.

The score of an airfoil is associated to an element of the score vector **s**, defined as the product between the performance matrix **P** and the weight vector **w**.

$$\mathbf{s} = \mathbf{P}\mathbf{w}, \tag{4.1}$$

The performance matrix is related to the value matrix **V** and the best performance vector **b**. The generic element of the **P** matrix is described by

$$P(i,k) = \begin{cases} \frac{V(i,k)}{b(k)}\ , & \text{if b(k) = max(V(i,k))} \\ \frac{b(k)}{V(i,k)}\ , & \text{if b(k) = min(V(i,k))}\ , \end{cases} \tag{4.2}$$

where i is the index of the airfoil (i = 1 ... 7) and k is the index of the performance (k = 1 ... 5). Essentially, the performance of an airfoil within a specific category is determined by its value in that category, normalized against the best value observed among all airfoils in that same category. Subsequently, a weighted sum across all categories is carried out to calculate the overall score for an airfoil.

The value matrix **V**, encompassing all the values associated with airfoils across all categories, is presented in table 4.10, columns 2 to 6.

The weighting for the scoring system has been established based on the following logics:

1. A crucial objective is to maximize the mission range, which, according to Breguet's formula adapted for electric aircraft, is directly proportional to the lift-to-drag ratio. To emphasize the importance of this condition, a weight of w = 0.40 has been assigned to it in the scoring system;

2. To attain high maximum speeds, it is crucial to maintain low C_d values, especially in conjunction with moderate and low C_l values. To emphasize this feature, the $C_{d\ \text{min}}$ of the airfoil has been evaluated. A weight of w = 0.40 has been set;

3. The pitching moment coefficient holds significance in both horizontal tail sizing and trim considerations. A desirable characteristic is a low absolute value for the pitching moment coefficient C_m. To highlight this feature, a weight of w = 0.10 has been assigned in the scoring system;

4. The fastest climb is achieved when the power index F is maximized, defined as $F = E\sqrt{C_L}$. Given that the climb phase is relatively brief in the overall flight profile, a relatively low weight (w = 0.05) has been assigned to this parameter in the scoring system;

5. Regarding the maximum lift coefficient, the UAV features VTOL capabilities, leading to a relatively tolerant requirement for the complete aircraft with $C_{L\ max} = 1.0$. A low weight (w = 0.05) has been assigned in the scoring system.

The weight vector **w** is: $\mathbf{w} = [0.05,\ 0.40,\ 0.05,\ 0.40,\ 0.10]^T$

The best performance vector **b** is: $\mathbf{b} = [1.3688,\ 87.1911,\ 89.8716,\ 0.0063,\ -0.0012]^T$

The considered airfoils included Ishii, Clark Y, NACA 2408, NACA 2410, NACA 2412, NACA 23012, and SD7003. Analyses were carried out using Xfoil, and the resulting polar (C_l, C_d) and ($\frac{C_l}{C_d}$, α) curves are illustrated in figure 4.6. Comprehensive results are detailed in table 4.10.

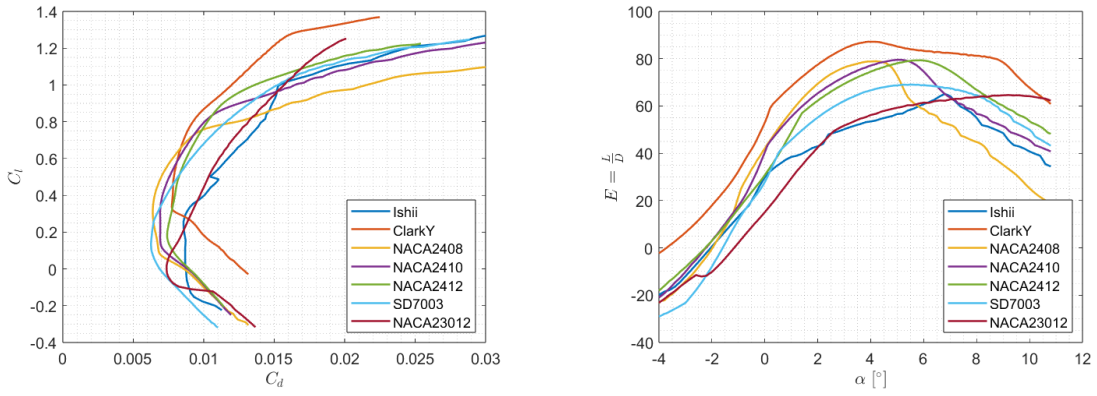

(a) Polar Curves

(b) Lift-to-drag ratio versus α

Figure 4.6: Xfoil results at Re = 330 000 and M = 0.09

Airfoil	$C_{l\ max}$	E_{max}	F_{max}	$C_{d\ min}$	$C_{m\ at\ E_{max}}$	**Score**
Ishii	1.3278	65.5635	65.7730	0.0086	-0.0511	0.6775
Clark Y	1.3688	87.1911	89.8716	0.0077	-0.0812	0.8249
NACA 2408	1.1395	78.9266	66.9774	0.0064	-0.0497	**0.8351**
NACA 2410	1.2335	79.5522	71.9789	0.0069	-0.0489	0.8146
NACA 2412	1.2254	79.3298	75.4626	0.0074	-0.0480	0.7907
NACA 23012	1.2524	64.6760	70.2025	0.0073	-0.0012	0.8016
SD7003	1.2470	69.0611	65.7646	0.0063	-0.0305	0.8215

Table 4.10: Aerodynamic performance of airfoils

In accordance with the applied scoring system, the top-performing airfoil is identified as the NACA 2408. Consequently, it has been selected for further analyses.

For the horizontal and vertical tail, the NACA 0012 airfoil has been selected. The Reynolds numbers relative to the mean aerodynamic chord of the horizontal and vertical tail are $Re_{\text{ht}} = 165\ 000$ and $Re_{\text{ht}} = 232\ 000$, respectively, at the cruise condition ($v_{\text{cruise}} = 31 \frac{m}{s}$).

Wing geometry

A study on the wing geometry has been carried out. The wing exhibits a taper ratio of $\lambda = 0.5$. The dihedral angle has been set to $\phi = 3°$ due to lateral-directional stability considerations. In a similar manner to the Mars case, a sweep angle $\Lambda_{c4} = 20°$ has been selected to permit the alignment of rotors with respect to the centre of mass during the vertical take-off and landing phases.

Table 4.11 illustrates the main characteristics of the aerodynamic surfaces of the Earth UAV.

Parameter	Wing	Horizontal Tail	Vertical Tail
Wing surface	$S = 0.2352$ m^2	$S = 0.0180$ m^2	$S = 0.0216$ m^2
Wingspan	$b = 1.4$ m	$b = 0.30$ m	$b = 0.18$ m
Airfoil	NACA2408	NACA0012	NACA0012
Aspect ratio	AR $= 8.33$	AR $= 5$	AR $= 1.50$
Mean aerodynamic chord	MAC $= 0.168$ m	MAC $= 0.06$ m	MAC $= 0.12$ m
Incidence	$i = 2°$	$i = -2°$	$i = 0°$
Taper ratio	$\lambda = 0.5$	$\lambda = 1.0$	$\lambda = 0.8$
Sweep angle	$\Lambda_{c4} = 20°$	$\Lambda_{c4} = 0°$	$\Lambda_{c4} = 10°$
Dihedral	$\Gamma = 3°$	$\Gamma = 0°$	$\Gamma = 0°$

Table 4.11: Aerodynamic surfaces geometry

UAV Polar

VLM analyses have been conducted using OpenVSP. The geometry of the UAV has been simplified to a fuselage, wing, horizontal and vertical tail. Figure 4.7 shows the results of VLM analyses at cruising conditions, hence at a Reynolds number of Re = 340 000 and a Mach number of M = 0.09.

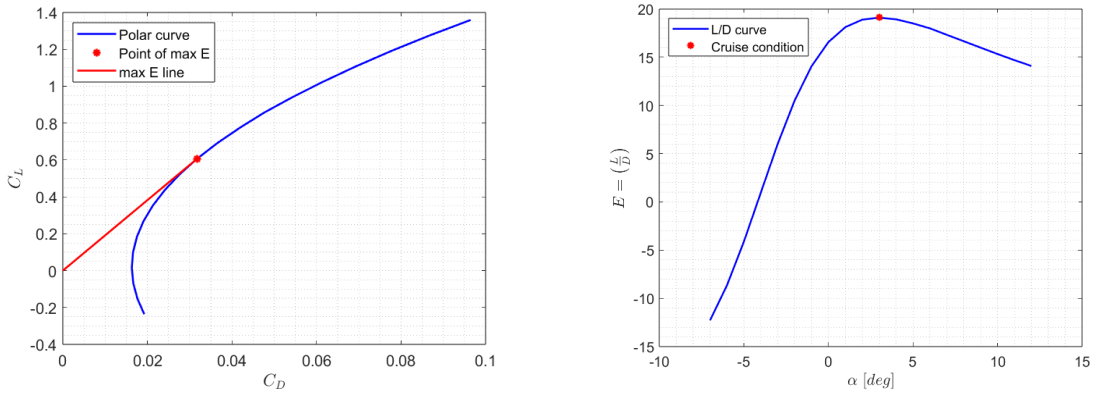

(a) Polar Curve

(b) Lift to Drag ratio versus α

Figure 4.7: Earth UAV: VLM Results on OpenVSP

In order to enhance the mission range, the UAV must operate at maximum lift-to-drag ratio, hence at $C_L = 0.60$ and $\alpha = 3°$. The corresponding cruising speed is $v_{\text{cruise}} = 31\frac{m}{s}$. A maximum lift-to-drag ratio $\frac{L}{D} = 18.7$ has been retrieved.

4.3.4. Stability

For the evaluation of the static and dynamic stability of the Earth UAV, the same procedure described in 3.3.4 has been applied. Figure 4.8 illustrates the eigenvalue maps for longitudinal and lateral-directional dynamics of the Earth UAV.

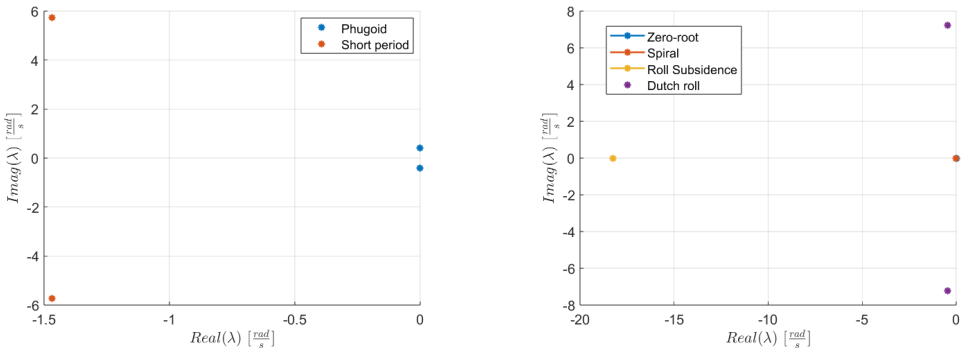

(a) Longitudinal dynamics (b) Lateral-directional dynamics

Figure 4.8: Eigenvalue Maps: Longitudinal and lateral-directional dynamics

At trimmed cruising condition, a static margin of SM = 21.9 % has been obtained.

Table 4.12 presents the longitudinal positioning of the centre of gravity, along with the geometric features of the UAV that influence stability and the control-fixed static stability criteria.

Parameter	Value
Centre of gravity longitudinal position	$X_{CG} = 0.167$ m
Horizontal tail surface ratio	$\frac{S_{\text{ht}}}{S} = 0.076$
Tail volume coefficient	$V_{\text{ht}} = 0.092$
Vertical tail surface ratio	$\frac{S_{\text{vt}}}{S} = 0.12$
Vertical tail volume coefficient	$V_{\text{vt}} = 0.013$
$C_{m_{G\alpha}}$	$C_{m_{G\alpha}} = -1.056\ \frac{1}{rad}$
$C_{l_{G\beta}}$	$C_{l_{G\beta}} = -0.119\ \frac{1}{rad}$
$C_{n_{G\beta}}$	$C_{n_{G\beta}} = 0.135\ \frac{1}{rad}$

Table 4.12: Stability data

4.4. Results

The Earth UAV is an electric fixed-wing drone, equipped with wing-mounted solar panels. It adopts a tilt-rotor configuration that allows vertical take-off and landing. This configuration is achieved through the use of four propellers, each with a diameter of 10 inches.

The UAV has a maximum take-off mass of MTOM = 7.5 kg, two of which are reserved for the payload mass $M_{\text{payload}} = 2$ kg. The battery package has a mass of $M_{\text{battery}} = 3.12$ kg. According to VLM analysis, the UAV should be capable to accomplish a mission with a range of $R = 495$ km in a time period of approximately 4 hours and 26 minutes.

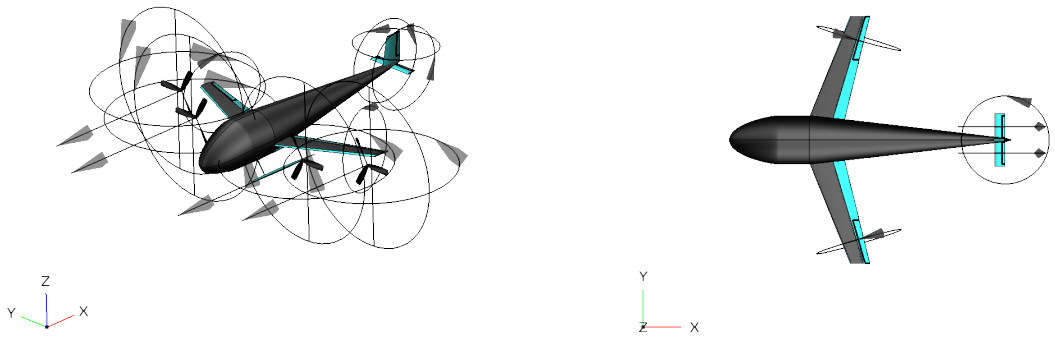

(a) Front-Left view (b) Top view

Figure 4.9: Earth UAV front-left and top views

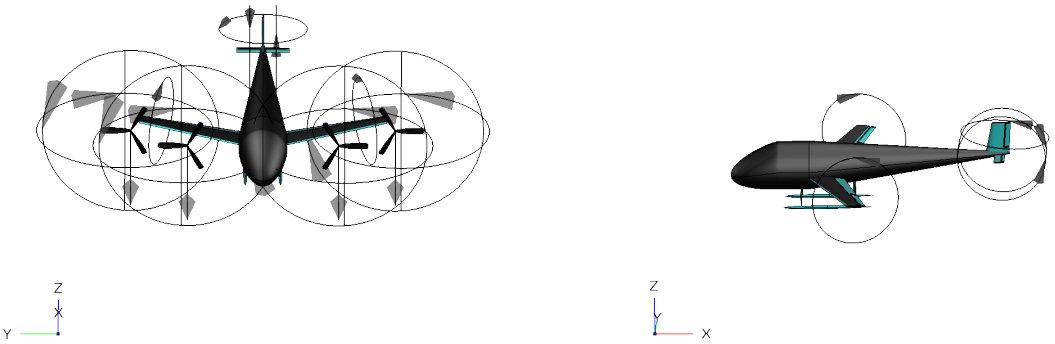

(a) Front view (b) Lateral view

Figure 4.10: Earth UAV front and lateral views

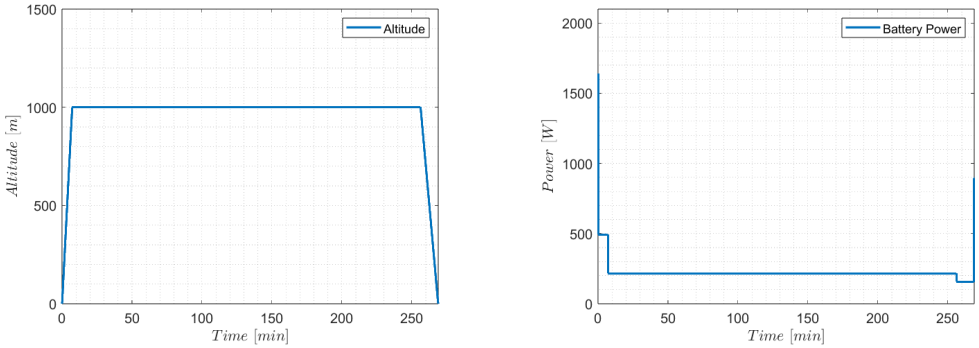

(a) Altitude versus time (b) Battery power versus time

Figure 4.11: Altitude and battery power versus time

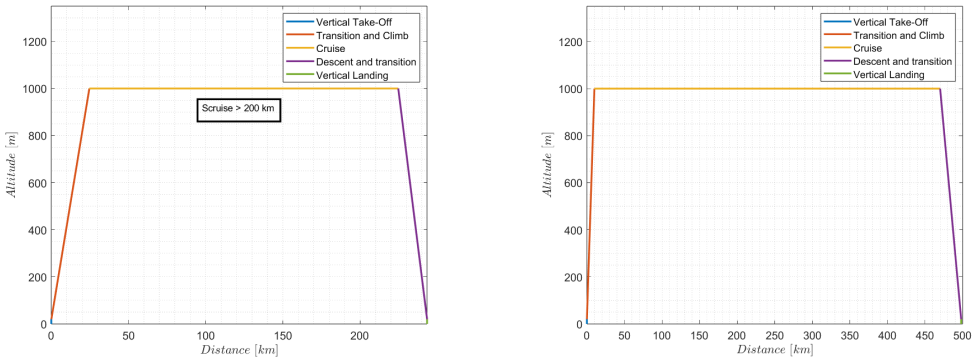

(a) Baseline mission profile

(b) Actual mission profile

Figure 4.12: Mission Profile comparison

Flight Phase	**Parameter**	**Value**
Vertical Take-Off	Vertical velocity, for $t = 20\ s$	$V_{v\ \mathrm{TO}} = 2.1\ \frac{\mathrm{m}}{\mathrm{s}}$
Climb	Rate of Climb, max 180 s	$V_v = 13.8\ \frac{\mathrm{m}}{\mathrm{s}}$
Cruise	Design cruising speed (V_{cruise})	$V_{\mathrm{cruise}} = 30.8 \frac{\mathrm{m}}{\mathrm{s}}$
Transition	Stalling speed (V_{stall})	$V_{\mathrm{stall}} = 20.6 \frac{\mathrm{m}}{\mathrm{s}}$
Maneuver	Maximum load factor (n_{max})	$n_{\mathrm{max}} = 1.6$
Service ceiling	Altitude (h_{ceiling})	$h_{\mathrm{ceiling}} > 9000\mathrm{m}$
Transition	Maximum lift coefficient	$C_{L\,\mathrm{max}} = 1.36$
Cruise	Design lift coefficient	$C_{L,\mathrm{cruise}} = 0.60$
Cruise	Maximum $E = \frac{L}{D}$	$E_{\mathrm{max}} = 18.7$
Fastest climb	Maximum $F = E\sqrt{C_L}$	$F_{\mathrm{max}} = 16.7$

Table 4.13: Earth UAV: Data

5 | Conclusions and future developments

5.1. Comparison between Mars UAV and Earth UAV

A comparison between the Mars UAV and Earth UAV is presented in this section.

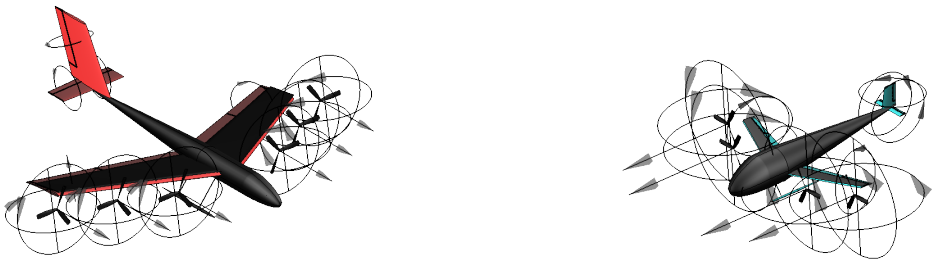

(a) Mars UAV (b) Earth UAV

Figure 5.1: Mars and Earth UAV comparison

The two UAVs share identical payloads, each featuring a compact gas chromatograph coupled with a mass spectrometer, estimated to have a mass of $M_{payload} = 2.0$ kg. However, the maximum take-off mass of the Mars UAV is close to 3 times greater than the MTOM of the Earth UAV. This feature is primarily attributed to a significantly greater structural mass (M_s), which includes the combined mass of the wings, horizontal and vertical tail, fuselage, and skid. In fact, the structural mass of the Martian drone is $M_s = 9.96$ kg versus the $M_s = 1.21$ kg of the terrestrial. Furthermore, the wing surface of the Mars UAV is about 10.8 times greater than the wing surface of the Earth UAV. This is asso-

ciated to to the poor wing loading observed at Martian atmospheric conditions. This is observed even when operating at higher speeds. The maximum shaft power necessary to perform the vertical take-off of the Martian drone is roughly 2.7 times greater than the one required by the terrestrial UAV.

Parameter	**Mars UAV**	**Earth UAV**
Maximum take-off mass	MTOM = 20.0 kg	MTOM = 7.5 kg
Payload mass	$M_{\text{payload}} = 2.0$ kg	$M_{\text{payload}} = 2.0$ kg
Structural mass	$M_s = 9.96$ kg	$M_s = 1.21$ kg
Battery package mass	$M_{\text{battery}} = 4.8$ kg	$M_{\text{battery}} = 3.12$ kg
Maximum shaft power	$P_b = 4.5$ kW	$P_b = 1.67$ kW
Wing surface	$S = 2.53$ m^2	$S = 0.235$ m^2

Table 5.1: Mars and Earth UAVs

Due to the Martian atmospheric characteristics, the Mars UAV operates a much lower Reynolds and higher Mach number with respect to the Earth UAV. The maximum lift-to-drag ratio of the Mars drone is about 58 % of its terrestrial counterpart.

It is noteworthy to compare the characteristics associated to the cruising conditions of the Mars UAV and the Earth UAV, as reported by table 5.2.

Parameter	**Mars UAV**	**Earth UAV**
Cruising altitude	$h_{\text{cruise}} = 1000$ m	$h_{\text{cruise}} = 1000$ m
Density	$\rho_{\text{cruise}} = 0.0138$ $\frac{\text{kg}}{\text{m}^3}$	$\rho_{\text{cruise}} = 1.12$ $\frac{\text{kg}}{\text{m}^3}$
Speed of sound	$c_{\text{cruise}} = 243.8\frac{\text{m}}{\text{s}}$	$c_{\text{cruise}} = 336.4\frac{\text{m}}{\text{s}}$
Dynamic viscosity	$\mu_{\text{cruise}} = 1.22 \cdot 10^{-5}$Pas	$\mu_{\text{cruise}} = 1.76 \cdot 10^{-5}$Pas
Reynolds	$Re = 92000$	$Ma = 330000$
Mach	$M = 0.38$	$M = 0.09$
Cruising speed	$v_{\text{cruise}} = 92\frac{\text{m}}{\text{s}}$	$v_{\text{cruise}} = 31\frac{\text{m}}{\text{s}}$
Lift coefficient	$C_L = 0.503$	$C_L = 0.606$
Drag coefficient	$C_D = 0.0467$	$C_D = 0.0324$
Lift-to-drag ratio	$E = 10.76$	$E = 18.70$

Table 5.2: Comparison of the cruising condition

Despite the atmospheric density at 1000 meters altitude on Mars being approximately 81 times lower than the density at the same altitude on Earth, the power required for

the Mars UAV during the cruising phase is remarkably higher. The Mars UAV demands about five times the power of the terrestrial case, with $P_{r,\text{Mars}} = 634.8$ W in contrast to Earth UAV's $P_{r,\text{Earth}} = 127.0$ W.

The terrestrial UAV exhibits significantly better aerodynamic characteristics, when compared to the martian drone.

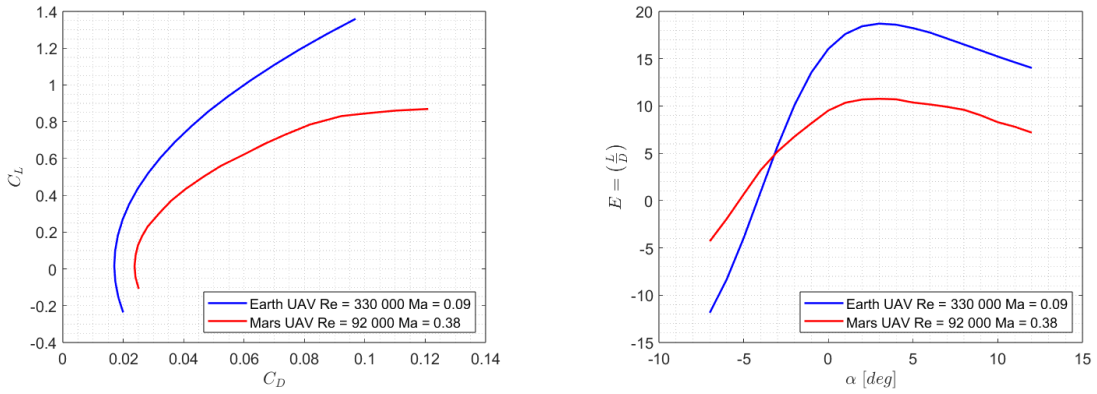

(a) Polar Curves (b) Lift to Drag ratio versus α curves

Figure 5.2: Comparison of VLM Results on OpenVSP

In addition, the terrestrial UAV is capable to operate for a larger mission range.

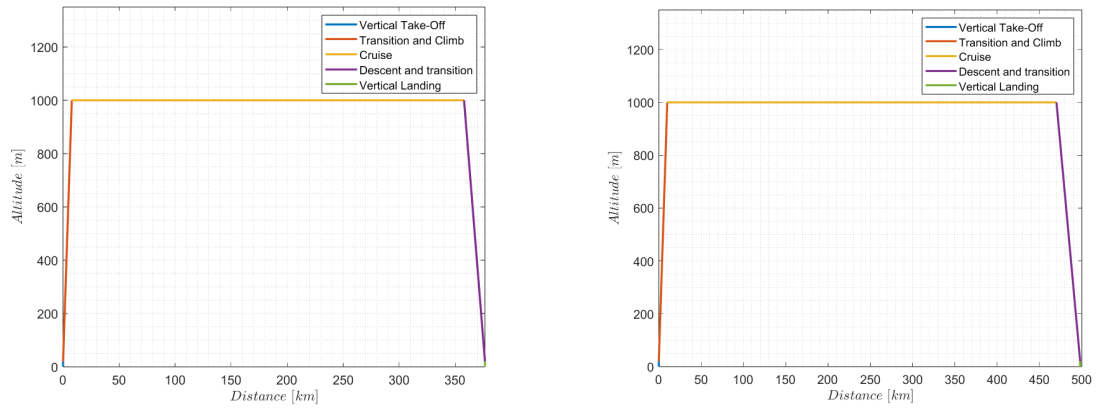

(a) Mars UAV Mission Profile (b) Earth Mission Profile

Figure 5.3: Comparison of flight profiles

Even operating at a larger gravitational acceleration, combining an higher battery mass fraction $\left(\frac{M_{battery}}{MTOM}\right)$ with an higher lift-to-drag ratio $\left(\frac{L}{D}\right)$, the mission range of the terrestrial UAV is about 32% higher ($R_{\text{Earth}} = 495$ km versus $R_{\text{Mars}} = 375$ km).

5.2. Future missions: Venus and Titan

Mars is not the only extra-terrestrial atmosphere gathering significant attention today. In fact, NASA is planning to launch a mission to Saturn's giant moon, Titan, by 2027. As reported by [39] and [18], the Dragonfly mission will have the objective to understand the prebiotic chemistry, that are the chemical steps that occurred on Earth that ultimately led to the formation of life. This mission will be performed by a rotorcraft called Dragonfly. The UAV will make use of a mass spectrometer named Dragonfly Mass Spectrometer (DraMS). Titan atmosphere is rich of organic compounds and, in the past, it presented liquid water on its surface. Titan's atmosphere is mostly composed by nitrogen (about 95 %) and methane (about 5 %), with traces of other carbon-rich compounds [50].

At high altitude, the energy provided by the Sun splits the methane and nitrogen molecules, that later recombine to form complex organic compounds. Often, these include nitrogen, oxygen and other elements important to life on Earth.

An engineering model of the atmosphere of Titan can be found in reference [14]. The atmosphere at the surface is characterised by a very low temperature $T = 92.1K$, a very high density $\rho = 5.26\ \frac{kg}{m^3}$, and a pressure 40 % higher than the standard pressure on Earth at 0 m altitude, with a reference value of $P = 141900\ Pa$. The gas constant is equal to $R = 292.91\ \frac{J}{KgK}$ and the speed of sound is extremely low, about $c = 194\ \frac{m}{s}$. The acceleration of gravity on the surface of Titan is very low, around $g = 1.35\ \frac{\mathrm{m}}{\mathrm{s}^2}$.

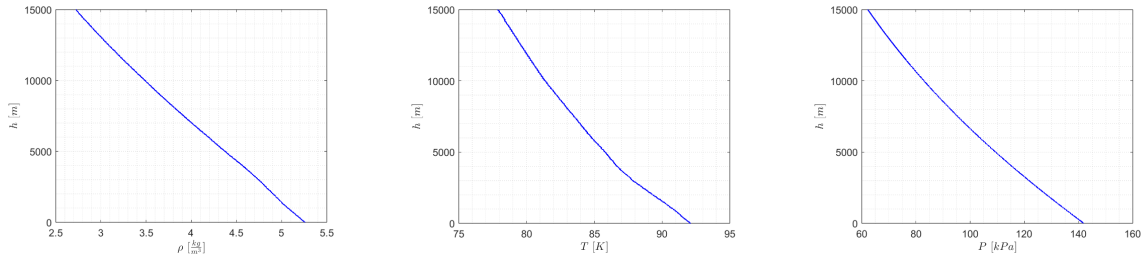

(a) Density (b) Temperature (c) Pressure

Figure 5.4: Titan Atmosphere

The power supply on Titan is a major issue. In fact, according to Pellerito, Olivas, and Hassanalian [33], a solar-powered drone could not be feasible. The main causes are the distance from the sun, and the thick, hazy atmosphere of Titan. As a consequence, a suitable solution might be represented by a nuclear-powered UAV.

Another planetary environment of great actuality is represented by Venus. As explained

by Glaze, Garvin et al. [15], the study of when and why the evolutionary pathways of Venus and Earth diverged is fundamental to understand how terrestrial planets form and how their atmospheres and surfaces evolve. NASA aims to explore Venus with the DAVINCI program, planned to launch by 2029. The objectives are the understanding of atmospheric origin and evolution, the analysis of the surface properties and the investigation of the atmospheric composition and surface interaction. Preliminary studies of fixed-wing atmospheric flight on Venus have been carried out by Landis, Colozza, and LaMarre, in 2002 [23].

Venus is the second Planet from the Sun, on its surface the gravitational acceleration is $g = 8.87\ \frac{\mathrm{m}}{\mathrm{s}^2}$. Venus atmosphere is mainly composed by Carbon dioxide (96.5 %), Nitrogen (Less than 3.5 %) and presents traces of Sulphur dioxide, Argon and Water vapour [35].

A detailed model of the Venusian atmosphere can be found in reference [10]. On Venus surface, the temperature is very high, about $T = 735.3$ K, the density is $\rho = 64.79\ \frac{\mathrm{kg}}{\mathrm{m}^3}$, and the pressure $P = 92.1$ bars. The specific heat ratio is $\gamma = 1.193$, the gas constant is $R = 191.34\ \frac{\mathrm{J}}{\mathrm{kgK}}$, hence the speed of sound at ground level is $c = 410\ \frac{\mathrm{m}}{\mathrm{s}}$. The dynamic viscosity is $\mu = 3.35 \times 10^{-5}$Pas.

The extremely high temperature on the Venus surface apparently makes convenient to fly at higher altitude, where temperature and pressure are lower. Figure 5.5 shows the variation with altitude of the atmospheric density, temperature and pressure.

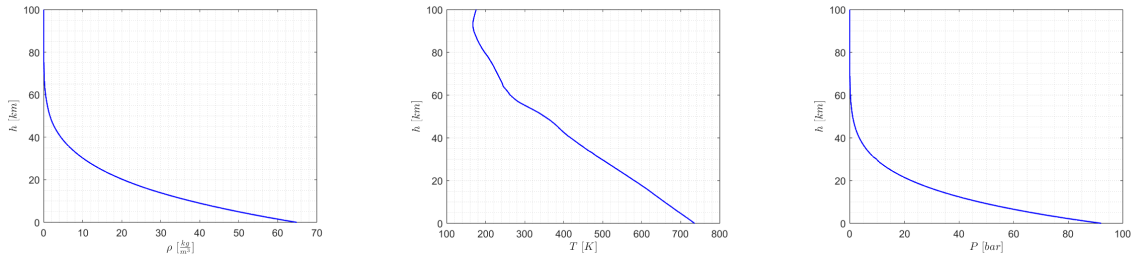

(a) Density (b) Temperature (c) Pressure

Figure 5.5: Venus Atmosphere

At 55 km altitude, the Venusian atmosphere exhibits more benign conditions. T = 302 K, P = 53140 Pa and $\rho = 0.9207\ \frac{kg}{m^3}$. However, Venus presents a cloud layer between 50 to 65 km altitude. Some droplets of sulfuric acid fall from the layer, creating a corrosive environment in the lower atmosphere. The cloud layer acts as a shield for the solar irradiance, hence the solar flux is abundant (about 2600 $\frac{W}{m^2}$), but only above 65 km altitude.

Moreover, extreme winds acts in the Venusian environment. Considering the mean wind profile as function of the altitude, a peak is visible close to the top of the cloud layer, with a mean wind speed reaching $v_{wind} = 95\frac{m}{s}$.

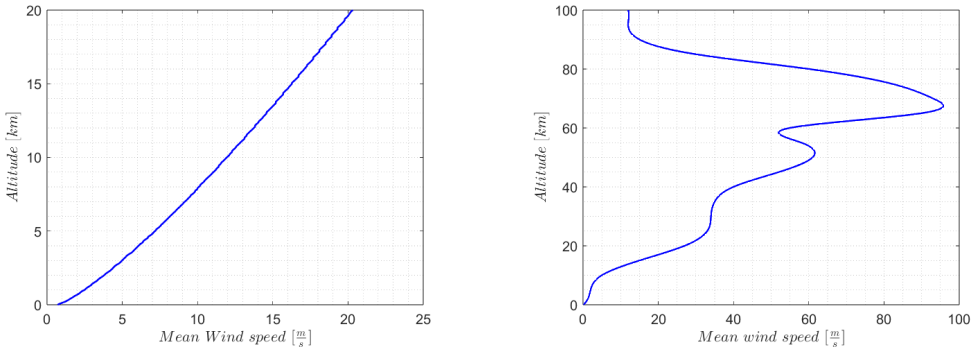

(a) Titan (b) Venus

Figure 5.6: Mean wind velocity profile on Venus and Titan

To highlight the effects of the planetary environmental conditions of Venus and Titan, the same analysis presented in section 2.2 has been repeated, considering terrestrial, Martian, Venusian and Titanic atmospheres. Considering the same test case of section 2.2, results are presented hereafter.

Given its atmospheric characteristics, Titan stands out as an ideal environment for executing long-range missions, leveraging the energy-efficient characteristics of fixed-wing UAVs. This is explained by the fact that the gravitational acceleration on Titan is very low $g_{\text{titan}} = 1.35\frac{\text{m}}{\text{s}^2}$. In addition, the high density environment of the atmosphere of Titan enables the conduction of the cruising phase at high Reynolds numbers, therefore it is reasonable to presume good aerodynamic performance in that scenario.

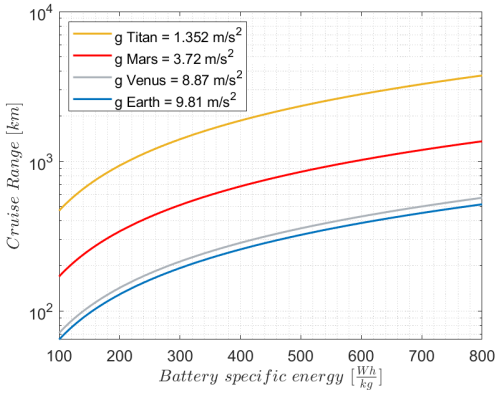

Figure 5.7: Range variation with specific energy and acceleration of gravity

For both Titan and Venus, achieving sufficiently large wing loading while effectively managing the wing surface and structural mass of the aerodynamic surfaces appears plausible, as shown by figure 5.8. In fact, the ratio between the atmospheric density at ground level and gravitational acceleration are extremely higher in the atmospheres of Titan $\frac{\rho_{\text{titan}}}{g_{\text{titan}}} = 3.89\ \frac{\text{kgs}^2}{\text{m}^4}$, and Venus $\frac{\rho_{\text{venus}}}{g_{\text{venus}}} = 7.30\ \frac{\text{kgs}^2}{\text{m}^4}$, when compared to the terrestrial $\frac{\rho_{\text{Earth}}}{g_{\text{Earth}}} = 0.125\ \frac{\text{kgs}^2}{\text{m}^4}$ or even the Martian $\frac{\rho_{\text{Mars}}}{g_{\text{Mars}}} = 0.004\ \frac{\text{kgs}^2}{\text{m}^4}$. Therefore, it is possible to expect that the wing surface of a fixed-wing UAV for the atmospheric flight on Venus or Titan assumes extremely compact dimensions.

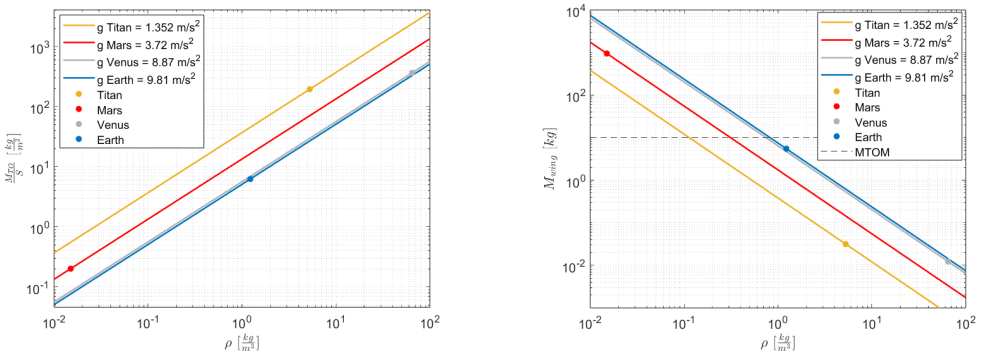

(a) Wing Loading (b) Wing Mass

Figure 5.8: Wing loading and wing mass

The high density atmospheres of Titan and Venus enhance the possibility to easily obtain large wing loading values. On the contrary, there are some implications on the power required to perform the vertical take-off in such environments.

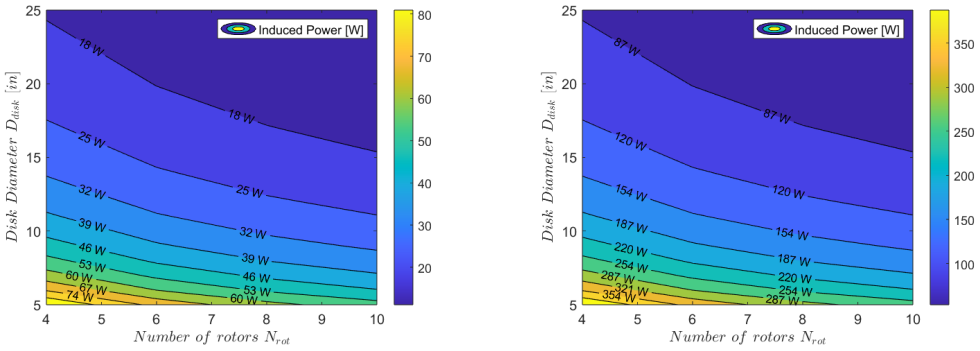

(a) Titan (b) Venus

Figure 5.9: Induced Power

On Titan, the induced power component assumes exiguous values, due to the fact the beneficial effect provided by the low gravitational acceleration is dominant over the adverse effect given by the large atmospheric density.

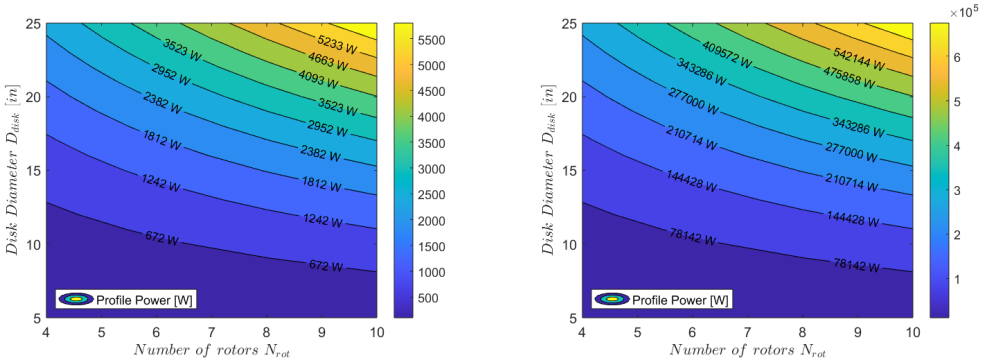

(a) Titan (b) Venus

Figure 5.10: Profile Power

The power profile component assumes moderate values in the atmosphere of Titan, if a proper combination of number of rotors and rotor diameter is selected. Instead, the profile power component assumes extremely high values in the Venusian atmosphere, in any case, due to its extremely high density $\rho_{\text{venus}} = 64.79 \frac{\text{kg}}{\text{m}^3}$ at ground level.

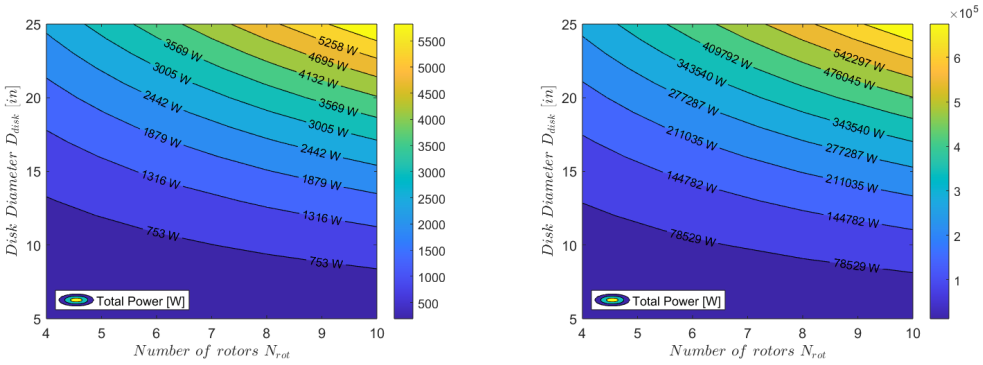

(a) Titan (b) Venus

Figure 5.11: Total Power

For both Titan and Venus, the profile power is the dominant component in the total required power for vertical take-off.

The combination of high density and low gravitational acceleration on the Titan surface, produce high wing loading (hence small wing surface) and moderate power loading (therefore moderate power demand to perform vertical take-off). The environment of Titan is also characterised by a moderate mean wind velocity profile.

On the contrary, the extreme conditions typical of the Venusian atmosphere suggest the impossibility to make use of eVTOL UAVs in such environment. In fact, the amount of power required to perform vertical take-off is huge (in the order of hundreds of kilowatts), just for an hypothetical small UAV with a maximum take-off mass of 10 kilograms.

5.3. Conclusions

In this thesis, it has been investigated the potential application of fixed-wing UAVs for the large scale aerial exploration of the Red Planet. An examination of Martian atmospheric conditions and a comparison with the terrestrial ones have been conducted to evaluate the influence of planetary environmental conditions on the design of fixed-wing Unmanned Aerial Vehicles. To conduct long-range missions in the extreme environment of Mars, it is required to exploit the benefits given by an extensive use of ultra-light materials and innovative battery technology. In addition, in the Martian environment, a drone must be able to guarantee self-charging capabilities. Insights have been presented about ultra-light materials, battery technology and solar panels.

Subsequently, the preliminary design of an electric vertical take-off and landing UAV has been presented, conceived to execute long-range missions on the Red Planet. The draft of the scientific mission in that scenario has been proposed. Afterwards, it has been presented a different eVTOL UAV conceived to accomplish a similar mission in the terrestrial environment. The objective was to evaluate the effects of the diverse planetary conditions on various design aspects, with a particular focus on aerodynamics. This thesis concludes with a comparison of the Martian and terrestrial drones, and a brief assessment of the possible applicability of fixed-wing UAVs in the extra-terrestrial atmosphere of Venus and Titan.

There is significant room for improvement in several aspects of this project. Structural and aeroelastic analyses are recommended to validate and enhance the hypotheses formulated regarding the structural design of the two UAVs. In addition, the design of propellers, conceived specifically for the Martian environmental conditions, will certainly provide better results in terms of accuracy, with respect to what proposed in this thesis, and potentially result in improved outcomes for the Mars scenario.

Furthermore, considering that this thesis evaluates the conceptual and preliminary design phases of the Martian and terrestrial UAVs, low-fidelity methods have been employed, when referring to aerodynamics. It is recommended to employ high-fidelity methods to more effectively assess the impact of planetary environmental conditions on the design and aerodynamic performance of the two drones. Considering the Mars UAV, optimising the wing airfoil, for example, using CFD analyses with SU2, through the adjoint method, could be a viable approach to attain more precise results and, theoretically, enhanced aerodynamic performance Indeed, extensively applying optimization methods to the aerodynamics of the UAV has the potential to yield significant benefits in enhancing the overall performance of the UAV, considering its operations at low Reynolds regime.

Furthermore, it is recommended to conduct high-fidelity studies using URANS or LES simulations, particularly for high-angle-of-attack configurations, in order to validate the maximum lift coefficients used during this work.

Further investigations on the future applicability of fixed-wing UAVs in other extra-terrestrial atmospheres is suggested, in particular referring to potential operations in the atmosphere of Titan.

Bibliography

[1] M. Acuna, J. Connerney, Ness, R. Lin, D. Mitchell, C. Carlson, J. McFadden, K. Anderson, H. Reme, C. Mazelle, et al. Global distribution of crustal magnetization discovered by the Mars Global Surveyor MAG/ER experiment. *Science*, 284(5415): 790–793, 1999. doi: https://www.science.org/doi/10.1126/science.284.5415.790.

[2] K. Antcliff, N. Borer, S. Sartorius, P. Saleh, R. Rose, M. Gariel, J. Oldham, C. Courtin, M. Bradley, S. Roy, et al. Regional Air Mobility: Leveraging our national investments to energize the American travel experience, 2021.

[3] M. Anyoji and D. Hamada. High-performance airfoil with low Reynolds-number dependence on aerodynamic characteristics. *Fluid Mechanics Research International Journal*, 3(2):76–80, 2019.

[4] M. Anyoji, T. Nonomura, H. Aono, A. Oyama, K. Fujii, H. Nagai, and K. Asai. Computational and experimental analysis of a high-performance airfoil under low-Reynolds-number flow condition. *Journal of Aircraft*, 51(6):1864–1872, 2014. doi: 10.2514/1.C032553.

[5] M. Anyoji, D. Numata, H. Nagai, and K. Asai. Effects of Mach number and specific heat ratio on low-Reynolds-number airfoil flows. *AIAA journal*, 53(6):1640–1654, 2015. doi: 10.2514/1.J053468.

[6] J. Appelbaum and D. Flood. Solar radiation on mars, 1989.

[7] R. Bardera, S. Sor, and A. García-Magariño. Aerodynamics of Mars 2020 rover wind sensors. In *Mars Exploration-a Step Forward*. IntechOpen, 2020. doi: 10.5772/intechopen.90912.

[8] N. Barlow. *MARS: An introduction to its interior, surface and atmosphere*. USA, 2008.

[9] H. E. Bass, C. H. Hetzer, and R. Raspet. On the speed of sound in the atmosphere as a function of altitude and frequency. *Journal of Geophysical Research: Atmospheres*, 112(D15), 2007.

[10] A. Beck and R. Schiffer. Models of Venus atmosphere, 1968. Technical report, NASA, 1968.

[11] K. Bugga, J.-P. Jones, S. Jones, C. Krause, and et al. Performance assessment of prototype lithium-sulfur cells from Oxis Energy. Technical report, NASA JPL and Oxis Energy, 2018.

[12] D. Dawson. Solar Impulse 2: Pulse on the future. *Composites World*, 71:36–53, 2016.

[13] De Vries Reynard; Hoogreef Maurice F.M.; Vos Roelof. Range equation for hybrid-electric aircraft with constant power split. *Journal of Aircraft*, pages 552–557, 2020. doi: https://arc.aiaa.org/doi/10.2514/1.C035734.

[14] N. Divine. Titan Atmosphere Models. Technical report, NASA, 1973.

[15] L. S. Glaze, J. B. Garvin, B. Robertson, N. M. Johnson, M. J. Amato, J. Thompson, C. Goodloe, and D. Everett. DAVINCI: Deep atmosphere Venus investigation of noble gases, chemistry, and imaging. In *2017 IEEE Aerospace Conference*, pages 1–5. IEEE, 2017.

[16] Glenn Research Center. Mars atmospheric model, Metric Units, 2023. URL `https://www.grc.nasa.gov/www/k-12/airplane/atmosmrm.html`.

[17] A. Guardone. Thermodynamics of Motion, 2015. Notes from Compressible Fluid Dynamics Course.

[18] G. Hautaluoma and A. Johnson. NASA's Dragonfly will fly around Titan looking for origins, signs of life, 2019. URL `https://www.nasa.gov/news-release/nasas-dragonfly-will-fly-around-titan-looking-for-origins-signs-of-life/`.

[19] S. Hoerner. Fluid dynamic drag: Practical information on aerodynamic drag and hydrodynamic resistance, 1965.

[20] W. Johnson. *Rotorcraft aeromechanics*, volume 36. Cambridge University Press, 2013.

[21] W. Johnson, S. Withrow-Maser, L. Young, C. Malpica, W. J. Koning, W. Kuang, M. Fehler, A. Tuano, A. Chan, A. Datta, et al. Mars science helicopter conceptual design, 2020.

[22] B. W. Kemmerer. *A Compositional Analysis of Artificial and Terrestrial Analog Martian Regolith Simulants*. PhD thesis, Florida Institute of Technology, 2019.

[23] G. Landis, A. Colozza, and C. LaMarre. Atmospheric flight on Venus. In *40th AIAA*

aerospace sciences meeting and exhibit, page 819, 2002. doi: http://dx.doi.org/10.2514/6.2002-819.

[24] P. R. Mahaffy, C. R. Webster, M. Cabane, P. G. Conrad, P. Coll, S. K. Atreya, R. Arvey, M. Barciniak, M. Benna, L. Bleacher, et al. The sample analysis at Mars investigation and instrument suite. *Space Science Reviews*, 170:401–478, 2012. doi: https://doi.org/10.1007/s11214-012-9879-z.

[25] C. Malespin. SAM, 2023. URL `https://mars.nasa.gov/msl/spacecraft/instruments/sam/`.

[26] P. Masson. The history of Mars exploration. Technical report, ESA, 2005. 1st Mars Express Science Conference.

[27] S. Maurice, B. Chide, N. Murdoch, R. D. Lorenz, D. Mimoun, R. C. Wiens, A. Stott, X. Jacob, T. Bertrand, F. Montmessin, et al. In situ recording of Mars soundscape. *Nature*, 605(7911):653–658, 2022. doi: https://doi.org/10.1038/s41586-022-04679-0.

[28] R. A. McDonald. Advanced modeling in OpenVSP. In *16th AIAA Aviation Technology, Integration, and Operations Conference*, page 3282, 2016.

[29] Y. Mikhaylik, I. Kovalev, C. Scordilis-Kelley, L. Liao, M. Laramie, U. Schoop, and T. Kelley. 650 wh/kg, 1400 wh/l rechargeable batteries for new era of electrified mobility. In *Proceedings of the 2018 NASA Aerospace Battery Workshop, Huntsville, AL, USA*, pages 27–29, 2018.

[30] Y. Mikhaylik, I. Kovalev, C. Scordilis-Kelley, L. Liao, M. Laramie, U. Schoop, and T. Kelley. Sion power batteries for ev and aerospace applications. Technical report, Sion Power Corporation, 2020.

[31] P. Nathen, A. Strohmayer, R. Miller, S. Grimshaw, and J. Taylor. Architectural performance assessment of an electric vertical take-off and landing (e-VTOL) aircraft based on a ducted vectored thrust concept. *Lilium GmbH, Claude-Dornier StraeSSe, Weßling, Germany, Tech. Rep*, 2021.

[32] B. N. Pamadi. Performance, Stability, Dynamics and Control of Airplanes, 1965.

[33] V. Pellerito, M. Olivas, and M. Hassanalian. Design a fixed-wing unmanned aerial vehicle with dynamic soaring capability for titan exploration. In *AIAA Scitech 2020 Forum*, page 2018, 2020.

[34] J. Roskam. Aircraft design, 1997. University of Kansas.

[35] Royal Belgian Institute for Space Aeronomy. Venus atmo-

sphere, mainly composed of carbon dioxide and nitrogen, 2023. URL https://www.aeronomie.be/index.php/en/encyclopedia/venus-atmosphere-mainly-composed-carbon-dioxide-and-nitrogen.

[36] M. H. Sadraey. *Aircraft Design: A System Engineering Approach*, chapter 10, page 560. John Wiley and Sons, Ltd., Daniel Webster College, New Hampshire, USA, 2013.

[37] R. Schmunk. ModelE AR5 simulations: Past climate change and future climate predictions, 2023. URL https://data.giss.nasa.gov/modelE/ar5plots/srlocat.html.

[38] D. Shaffer, M. Turner, and R. Nelson. Aerodynamic prediction for low Reynolds numbers. *Department of Aerospace and Mechanical Engineering, University of Notre Dame*, 2010.

[39] W. Steigerwald. NASA instrument bound for titan could reveal chemistry leading to life, 2023. URL https://www.nasa.gov/missions/nasa-instrument-bound-for-titan-could-reveal-chemistry-leading-to-life/.

[40] C. Szopa, D. Coscia, M. Cabane, and A. Buch. Miniaturized gas chromatography for space exploration: A 50 years history. In *2017 Symposium on Design, Test, Integration and Packaging of MEMS/MOEMS (DTIP)*, pages 1–4. IEEE, 2017.

[41] M. G. Trainer, M. H. Wong, T. H. McConnochie, H. B. Franz, S. K. Atreya, P. G. Conrad, F. Lefèvre, P. R. Mahaffy, C. A. Malespin, H. L. Manning, et al. Seasonal variations in atmospheric composition as measured in Gale Crater, Mars. *Journal of Geophysical Research: Planets*, 124(11):3000–3024, 2019. doi: 10.1029/2019JE006175.

[42] Unknown. Mars Express Science highlights: 4. probing the polar regions, 2019. URL https://sci.esa.int/web/mars-express/-/51824-4-probing-the-polar-regions.

[43] Unknown. Thin triple-junction solar cell for space applications (ctj30 – thin). Technical report, CESI S.p.A., 2020.

[44] Unknown. Technology blog, 2021. URL https://lilium.com/newsroom-detail/technology-behind-the-lilium-jet?gl=1*ejtjo*_up*MQ..*_ga*Mzg1MjcwNzgyLjE2OTQ2ODYzNzY.*_ga_9YC7ETNZ98*MTY5NDY4NjM3Ni4xLjEuMTY5NDY4NjM4Ni4wLjAuMA..

[45] Unknown. Mars facts, 2023. URL https://science.nasa.gov/mars/facts/.

[46] Unknown. Historical log, 2023. URL https://mars.nasa.gov/mars-exploration/missions/historical-log/.

[47] Unknown. The Atmosphere: Introduction to the Atmosphere, 2023. URL https://www.noaa.gov/jetstream/atmosphere.

[48] Unknown. Flight log, 2023. URL https://mars.nasa.gov/technology/helicopter/#Helicopter-Highlights.

[49] Unknown. Planetary fact sheet - metric, 2023. URL https://nssdc.gsfc.nasa.gov/planetary/factsheet/.

[50] Unknown. Titan: Facts, 2023. URL https://science.nasa.gov/saturn/moons/titan/facts/.

[51] L. Wald. Basics in solar radiation at Earth surface - revised version 3. *HAL*, 2019. doi: https://minesparis-psl.hal.science/hal-02181163.

[52] T. Zhao. Propulsive battery packs sizing for aviation applications, 2018.

List of Figures

List of Tables

List of Symbols

Variable	Description	SI unit
$\boldsymbol{\rho}$	Atmospheric density	$\frac{\mathrm{kg}}{\mathrm{m}^3}$
$\boldsymbol{T}$	Temperature	K
$\boldsymbol{P}$	Pressure	Pa
$\boldsymbol{C_v} = \left(\frac{\partial e}{\partial T}\right)_v$	Isochoric specific heat	$\frac{\mathrm{J}}{\mathrm{molK}}$
$\boldsymbol{C_p} = \left(\frac{\partial h}{\partial T}\right)_P$	Isobaric specific heat	$\frac{\mathrm{J}}{\mathrm{molK}}$
$\boldsymbol{\gamma} = \frac{\boldsymbol{C_p}}{\boldsymbol{C_v}}$	Specific heat ratio	–
R	Universal gas constant	$\frac{J}{\mathrm{molK}}$
$\boldsymbol{R}_{\mathrm{gas}}$	Gas constant	$\frac{\mathrm{J}}{\mathrm{kgK}}$
$\boldsymbol{c}$	Speed of sound	$\frac{\mathrm{m}}{\mathrm{s}}$
$\boldsymbol{M}$	Mach number	–
$\boldsymbol{\mu}$	Dynamic viscosity	$\mathrm{Pa} \cdot \mathrm{s}$
$\boldsymbol{Re}$	Reynolds number	–
MAC	Wing mean aerodynamic chord	m
$\boldsymbol{\lambda}$ or AR	Aspect ratio	–
$\boldsymbol{e}$	Oswald factor	–
$\boldsymbol{C_l}$	Airfoil lift coefficient	–
$\boldsymbol{C_d}$	Airfoil drag coefficient	–
$\boldsymbol{C_L}$	Aircraft drag coefficient	–
$\boldsymbol{C_D}$	Aircraft drag coefficient	–
$\boldsymbol{E}$	Aircraft lift-to-drag ratio	–
$\boldsymbol{F}$	Aircraft power index	–
MTOM	Maximum take-off mass	kg

Acknowledgements

Vorrei riservare questo spazio per ringraziare tutte le persone che mi hanno accompagnato durante questo percorso. Per prima cosa vorrei ringraziare il Professor Alberto Guardone per avermi dato la possibilità di svolgere questo lavoro in un ambiente stimolante e ricco di entusiasmo, e per avermi assistito durante l'intero percorso. Ringrazio Niccolò per la sua collaborazione durante questo progetto. Ringrazio i miei amici Lazza, Edo, Richi, Cenni, Anto, Muso, Redo, Mor, Marghe e Giudi per tutti i momenti condivisi insieme. Dedico un ringraziamento agli amici della triennale, specialmente a Pietro e ad Apo, in parte è merito (o colpa) loro, se alla fine del primo anno di Ingegneria ho scelto di cambiare facoltà e di iscrivermi ad Ingegneria Aerospaziale. Grazie agli amici di Fly-Mi, per avermi accompagnato in questa avventura straordinaria, ricca di ostacoli ma che ci ha regalato grandi gioie e soddisfazioni. Grazie agli amici di Meccanica del Volo per le sfide affrontate e superate insieme, in particolare a Chri e a Sofi. Il ringraziamento più grande va naturalmente alla mia famiglia, ai miei genitori Giulia e Silvio e a mio fratello Luca. A loro sarò per sempre grato. Ringrazio i miei genitori per avermi reso quello che sono oggi, per essermi stati di esempio ogni singolo giorno, per avermi dato la possibilità di studiare, per avermi insegnato a dare sempre il meglio di me e per aver creduto in me fin dal primo giorno. Senza di loro questo traguardo non sarebbe possibile. Grazie a mio fratello Luca, per il suo continuo sostegno lungo questo cammino, per aver sempre creduto in me, per tutti i momenti che abbiamo condiviso crescendo insieme, e per tutti gli insegnamenti che mi ha dato. Un ringraziamento è rivolto a Fede, da molto tempo compagna di viaggio di Luca, per il suo supporto e per aver sempre creduto in me. Grazie ai miei zii, Maura e Stefano, e ai miei cugini, Simo e Lori, per tutti i momenti trascorsi insieme. Un ringraziamento speciale è rivolto alle mie nonne Ersy e Mina, e ai miei nonni Mario e Gianni, per il loro immenso affetto e per tutti gli insegnamenti che mi hanno trasmesso.

Marco